NTNU – Trondheim
Norwegian University of
Science and Technology

Fatigue of Welded AA6082 Alloys - Effects of PWHT and Shot Peening

Sophie Caroline Utne

Chemical Engineering and Biotechnology
Submission date: June 2013
Supervisor: Trond Furu, IMTE
Co-supervisor: Hans Jørgen Roven, IMT
Ole Runar Myhr, KT

Norwegian University of Science and Technology
Department of Materials Science and Engineering

”A reader lives a thousand lives before he dies. The man that never reads lives only ones.”

– George R.R. Martin - *A Dance With Dragons (2011)*

Preface

This master's thesis is the result of work done at the Department of Materials Science and Engineering at the Norwegian University of Science and Technology (NTNU) during spring 2013. This thesis is a continuation of my specialization project fall 2012, and is a collaboration between Hydro, Qatar Petroleum, Qatalum, NTNU and Qatar University. The goal of this thesis is to characterize the microstructure, mechanical and fatigue properties of welded aluminum profiles.

First I would like to thank my supervisors Professor II Trond Furu, Professor Hans Jørgen Roven and Professor II Ole Runar Myhr for guidance and support during this work. I would especially thank Professor Hans Jørgen Roven for all the enlightening and inspiring discussions on the topics. Furthermore, I would like to thank Pål Christian Skaret for assisting me with my experimental work in the MTS laboratory and thanks to Yingda Yu for guidance concerning SEM-work.

A special thanks to Hydro Aluminium and Materials Strategic Area at NTNU for sponsoring this thesis. Thanks to Hydro for taking us to Doha, Qatar January 2013.

Last but not least, thanks to all my fellow students for support, motivation and lots of fun throughout the last five years. *Hvala!*

Declaration

I hereby declare that this work has been performed independently and in accordance with the rules and regulations at the Norwegian University of Science and Technology (NTNU).

Trondheim, June 2013

Sophie Caroline Utne

Abstract

Aluminum is a metal widely used in areas such as a construction material in buildings, transportation, oil and gas industry, in packaging for preserving food and drink, electric cables, heat exchangers and many other areas. The wide area of use is due to aluminum being a relatively light metal (1/3 of the weight of steel), has relatively high strength, good formability, high corrosion resistance, is a good conductor of heat and electricity, has good reflectivity, and can be recycled over and over again. The latter lowers the CO_2 footprint and the energy consumption substantially. This master's thesis is very relevant to the oil and gas industry, transportation industry (car, ship, train, etc.) and to other industries involving the use of metal inert gas (MIG) welded aluminum. Welded aluminum profiles of an Al-Mg-Si alloy, AA6082, is to be characterized in terms of fatigue. Fatigue is the dominant cause of collapse of components in structures that experience applied cyclic loads over a certain limit. Fatigue behavior of a structure relies on mechanical design, the actual surrounding environment and the materials microstructure, mechanical strength, intrinsic properties and surface quality. The fatigue behavior will be discussed on the basis of variations in the microstructure (morphology and grain structure) of the weld metal, the HAZ and the base material. Also, the influence of surface quality and the external environment (humidity and temperature) will be investigated. As welding reduces the strength of aluminum, two post weld treatments, PWHT and shot peening, will therefore be investigated to see how they affect the strengths of welded aluminum. Various techniques and equipment will be used such as fatigue and tensile machines, roughness and surface measuring instruments, hardness tester, optical light microscopy and scanning electron microscopy (SEM).

This master's thesis is part of an international collaboration project between Norway and Qatar where the participating industrial partners are Hydro, Qatar Petroleum (QP) and Qatalum (primary aluminum plant in Qatar where QP and Hydro owns 50 % each).

The microstructures were investigated of both the base materials and across the weld. The microstructure of the base material showed the typical fibrous grain structure of the AA6082 alloy along with a recrystallized layer along the surfaces from the extrusion. The welded profiles presented typical characteristics as recrystallization and nucleation in the weld, grain growth in the heat affected zone (HAZ) and a fusion line.

The AA6082.52-T6, welded fall 2012, revealed a very poor welding. The HAZ went throughout the welded profiles. This affected all of the properties of this profile, reducing the yield strength with 71 % and the ultimate tensile strength by 50 % compared to the base material. The fatigue resistance was also reduced, by 35 %. The fatigue fractography also revealed large pores due to entrapped air during welding. Therefore, these results are not representative for welded AA6082.52-T6.

The AA6082.50 base material had lower strengths than AA6082.52 due to some differences in the chemical composition. The AA6082.50-T6 was welded spring 2013 and showed an improved welding. The resulting decrease of yield strength compared to the base material was 40 % and

the ultimate tensile strength by 20 %. The fatigue resistance was decreased by 40 % compared to the base material. By introducing PWHT, the fatigue resistance increased with 26 % compared to the as welded. The yield strength increased with 40 % and the ultimate tensile strength with 6 %.

Shot peening of the as welded specimens did not increase the strength of the material as much as the PWHT. The yield strength increased with 10 % and the ultimate tensile strength with 4 %. The fatigue resistance however, increased with 38 % and showed a better fatigue limit than the base material.

The fatigue fractography of AA6082.50-T6 showed all of the usual characteristics of a fatigue failure. Some irregularities were found in the shot peened specimens suggesting some hydrogen diffusion had occurred. Some hydrogen diffusion is also suspected in the PWHT specimens.

All of the results in this thesis was somewhat consistent with literature values.

Sammendrag

Aluminium er et metall mye brukt i områder som konstruksjonsmateriale, transport, olje-og gassindustrien, i emballasje for å oppbevare mat og drikke, elektriske kabler, varmevekslere og mange andre områder. Det brede bruksområdet til aluminium er grunnet den forholdsvis lave vekten (1/3 av vekten av stål), i tillegg har aluminium relativt høy styrke, god formbarhet og høy korrosjonsmotstand, er en god leder for varme og elektrisitet, har god refleksjon, og kan resirkuleres igjen og igjen. Sistnevnte reduserer CO_2 fotavtrykket og energiforbruket betydelig. Denne masteroppgaven er svært relevant for olje-og gassindustrien, transportbransjen (bil, båt, tog, osv.) og for annen industri som involverer bruk av sveiset aluminium. Sveiste aluminium profiler av en Al-Mg-Si legering, AA6082, skal karakteriseres i henhold til utmatting. Utmatting er den dominerende årsaken til kollaps av komponenter i strukturer som opplever påførte fluktuerende belastninger over en viss grense. Utmattingsoppførselen av en struktur er avhengig av mekanisk design, selve omkringliggende miljø og materialets mikrostruktur, mekanisk styrke, intrinsikke egenskaper og overflatekvalitet. Utmatting vil bli drøftet på grunnlag av variasjoner i mikrostrukturen (morfologi og kornstruktur) av sveisemetallet, HAZ og grunnmaterialet. Dessuten vil påvirkning av overflatekvaliteten og det ytre miljøet (fuktighet og temperatur) undersøkes. Ettersom sveising svekker styrken til aluminium vil to typer etterbehandlinger, varmebehandling og overflatebehandling, bli undersøkt for å se hvor mye disse påvirker styrkene til sveiset aluminium. Ulike teknikker og utstyr vil bli brukt som utmattings- og strekkmaskiner, ruhet og overflate måleinstrumenter, hardhetstester, optisk lysmikroskopi og skanning elektronmikroskopi (SEM).

Masteroppgaven er en del av et internasjonalt samarbeidsprosjekt mellom Norge og Qatar hvor de deltakende industrielle partnerne er Hydro, Qatar Petroleum (QP) og Qatalum (aluminiumverket i Qatar der QP og Hydro eier 50 % hver).

Mikrostrukturene av både grunnmaterialet og på tvers av sveisen ble undersøkt. Mikrostrukturen av grunnmaterialet viste den typiske fiberstrukturen av AA6082 legeringen sammen med et rekrystallisert sjikt langs overflatene fra ekstruderingen. De sveiste profilene presenterte typiske kjennetegn som rekrystallisasjon og korndannelse i sveisen, kornvekst i den varmepåvirkede sonen (HAZ) og en fusjonslinje.

AA6082.52-T6, sveiset høsten 2012, avdekket en svært dårlig sveising. HAZ strakk seg helt ut til endene i den sveiste profilen. Dette påvirket alle egenskapene til denne profilen, reduserte flytegrensen med 71 % og strekkfastheten med 50 % i forhold til grunnmaterialet. Utmattingsmotstanden ble også redusert, med 35 %. Utmattingsfraktografien avdekket store porer på grunn av luftlommer dannet under sveising. Derfor er disse resultatene ikke er representative for sveiset AA6082.52-T6.

AA6082.50 grunnmaterialet hadde lavere styrke enn AA6082.52 grunnet noen forskjeller i den kjemiske sammensetningen. AA6082.50-T6 ble sveiset våren 2013 og viste en forbedret sveising. Resultatene viste en nedgang i flytegrensen sammenlignet med grunnmaterialet med 40 % og

strekkfastheten med 20 %. Utmattingsmotstanden viste lignende resultater, og var redusert med 40 % i forhold til grunnmaterialet. Ved å introdusere PWHT økte utmattingsmotstanden med 26 % i forhold til den sveiste. Flytegrensen økte med 40 % og strekkfastheten med 6 %.

Overflatebehandling med glasskuler av de sveiste prøvene økte ikke styrken av materialet i like stor grad som PWHT. Flytegrensen økte med 10 % og strekkfastheten med 4 %. Utmattingsmotstanden økte imidlertidig med 38 % og viste en bedre utmattingsgrense enn grunnmaterialet.

Utmattingsfraktografien av AA6082.50-T6 viste alle de vanlige egenskapene ved en utmattingsfeil. Noen uregelmessigheter ble funnet i de overflatebehandlede prøvene som tydet på at noe hydrogendiffusjon hadde inntruffet. Resultatene for PWHT tyder også på at noe hydrogendiffusjon har skjedd under varmebehandlingen.

Alle resultatene i denne avhandlingen var i samsvar med litteraturverdier.

Table of Contents

List of Figures

List of Tables

Abbreviations

A	=	Area [mm^2]
A_r	=	Amplitude ratio
α_l	=	Coefficient of thermal expansion [K^{-1}]
BM	=	Base material
d	=	Diameter [mm]
DC	=	Direct-chill (casting process)
E	=	Modulus of elasticity [GPa]
ϵ	=	Strain [mm/mm]
GP	=	Guinier-Preston zone
H	=	Hardness [MPa]
HAZ	=	Heat affected zone
HK	=	Knoop Hardness
HV	=	Vickers hardness
k	=	Thermal conductivity [$Wm^{-1}K^{-1}$]
MIG	=	Metal inert gas (welding)
N	=	Number of cycles
N_f	=	Number of cycles to failure
N_i	=	Crack initiation fatigue life
N_p	=	Crack propagation fatigue life
P	=	Load [N]
PWHT	=	Post weld heat treatment
qw	=	Minimum rate of energy release per unit area [Wm^{-2}]
R	=	Stress ratio
r	=	Radius [m]
RO	=	Run-outs
SEM	=	Scanning electron microscope
SCF	=	Stress concentration factor
SD	=	Standard deviation
S-N curve	=	Stress - Number of cycles to failure curve
SP	=	Shot peening/Shot peened
σ	=	Stress [MPa]
T	=	Temperature [K]
T_m	=	Melting temperature [K]
T4	=	Naturally aged temper condition
T6	=	Artificially aged temper condition
TIG	=	Tungsten inert gas (welding)
σ_{ys}	=	Yield strength [MPa]
W	=	Weld/Welded

1 Introduction

This thesis is a part of an international collaboration between students at the Norwegian University of Science and Technology (NTNU) and Qatar University, Hydro in Norway, Qatar Petroleum and Qatalum in Qatar. It is a part of a strategy to increase the use of aluminum in the gas and oil sector in Qatar. To be able to exploit the use of aluminum even further, more knowledge is required about its microstructure and its mechanical and fatigue properties. This thesis aims to give more data about welded aluminum profiles, where the microstructure analysis relates to the mechanical and fatigue behavior. The thesis is divided into three groups, one working with mechanical properties in general, one with corrosion and one with fatigue. The alloy that is to be investigated at NTNU is AA6082, and the alloys investigated at Qatar University are AA6005, AA6061.47, AA6063.60 and AA6082. The alloys are cooled from elevated temperature shaping process and naturally aged (T1) or solution heat treated followed by artificially aged (T6). All of the extruded profiles have been welded by MIG (metal inert gas) at SINTEF, Trondheim, Norway.

Presented results for alloy AA6082.52 were all done during the specialization project fall 2012, except the fatigue and tensile results in the T6 temper conditions. The AA6082.52 results are included to give a better overview of the mechanical and fatigue properties of this alloy.

Objective

In this thesis the fatigue life of welded aluminum profile, AA6082, will be investigated. The fatigue testing will be in the high cycle fatigue region. Microstructure, hardness, surface roughness, mechanical strengths and fracture mechanisms will also be studied. The object of this thesis is to correlate the fatigue life with these properties of welded AA6082. In addition it will focus on post weld treatments to increase the strength of the heat affected zone, hence increasing the fatigue life. Post weld heat treatment and shot peening are the methods chosen and they will be investigated to see how they affect the microstructure, mechanical properties and fatigue life.

2 Basic Theory

2.1 Background

Aluminum is, due to several reasons, considered a so-called green metal. Firstly, aluminum is 100 percent recyclable and about 75 percent of all aluminum produced since 1888 has been recycled and is still used today. Today, approximately 90 percent of all aluminum in use is recycled. Secondly, the energy input needed to recycle aluminum is only 5 percent of the energy originally used to produce aluminum from bauxite. Thirdly, bauxite is the third most abundant mineral in the earths crust, resulting in minimal land use (Hydro, 2012).

In addition, as aluminum and its alloys are much lighter than comparable materials, the use of aluminum in transport will reduce greenhouse gas emissions, making aluminum an environmental winner (Hydro, 2012).

2.2 Materials

2.2.1 Microstructure and alloys

The chemical composition of the two AA6082 aluminum alloys in this thesis are given in weight percent in Table 2.1, provided by Hydro (Furu, 2012).

Table 2.1: Chemical compositions of the two AA6082 alloys given in weight percent.

Alloy	Fe	Si	Mg	Mn	Cr	Cu	Zn	Ti	Ga	Al
AA6082.52	0.22	1.00	0.81	0.53	0.14	0.10	0.00	0.01	0.01	bal.
AA6082.50	0.20	1.02	0.67	0.53	0.00	0.003	0.006	0.01	0.01	bal.

Microstructure and strengthening methods have almost all to do with the resulting strength of a material. For a given alloy composition, the resulting properties are affected by the particular processing method chosen. The alloys presented here are of the aluminum 6xxx series and have been solution heat treatment to create a solid solution of the alloying elements. The two temper conditions, T1 and T6, are naturally aging and artificial aging respectively. The entire processing of the profiles is shown in Figure 2.1. During aging, the precipitation hardening occurs. Not all aluminum alloy series respond to this type of hardening, neither does all the series respond to heat treatment. The 2xxx, 6xxx and 7xxx series are heat treatable and are therefore capable of higher strengths than the other series (Dowling, 2012).

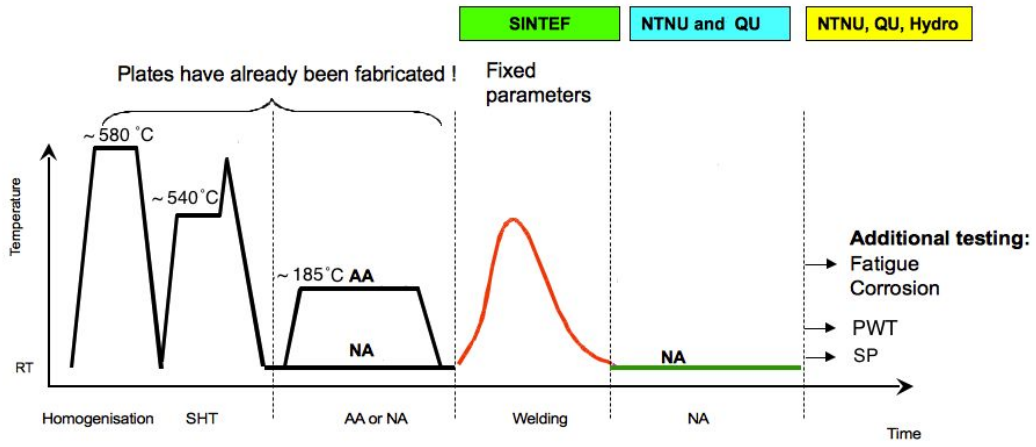

Figure 2.1: Processing of the aluminum profiles (Furu, 2012).

Figure 2.1 describes the processing of the aluminum profiles from homogenization to age hardening. The solution heat treatment of the alloys was carried out in a lab furnace at $540°C$ for 30 minutes and water quenched after solutionized. The age hardening process involved heating the samples to $185°C$ at a heating rate of $200°C$/h, keeping the materials at desired temperature for 5 hours, followed by cooling in air to room temperature (Furu, 2012).

2.2.2 Casting and extrusion

The use of casting techniques are favorable when either the finished shape is to large or complicated that no other technique would suffice. Casting is also preferred if the desired alloy has such a low ductility that forming by either cold or hot working is difficult, or if casting is just more economical compared to other techniques (Callister, 2007).

Casting is a fabrication process where a molten metal is poured into a mold cavity having the desired shape. The metal assumes the shape of the mold when the solidification of the molten metal takes place. During solidification, the shape may undergo some shrinkage (Callister, 2007).

Direct-chill (DC) casting is a semi-continuos casting process. The molten metal is solidified by casting into large ingot molds followed by a primary hot-rolled operation, giving a flat sheet or a slab. The solidification occurs in a water-cooled die with a desired cross-sectional geometry (Callister, 2007).

The alloys used in this thesis were DC cast at the reference center at Hydro Research and Technology Development (RTD) centre in Sunndal, 203 mm in diameter and a length of 3.25 m. The homogenization treatments are listed in Table 2.2 (Furu, 2012).

Table 2.2: Homogenization parameters of the two AA6082 alloys.

Alloy	Homogenization temperature and time	Cooling rate
AA6082.52	100°C/h holding at 580°C for 3 hours	350 − 300°C/h
AA6082.50	200°C/h holding at 580°C for 2 hours	350 − 300°C/h

The extrusion of the alloys was done at Hydro Aluminum Profiles a.s. at Raufoss. The extruded materials were 210 mm wide and 3 mm thick. Two different dies were applied, and all samples used in this thesis are taken from the middle part of the extruded section. Details of the extrusions are given in Table 2.3 (Furu, 2012).

Table 2.3: Detalis of the extrusion process.

Alloy	Charge	Press	Billet temp. [°C]	Ram speed [m/min]
AA6082.52	7728	5	510	6 (1 press), 5 (4 press)
AA6082.50	7609	3	515	0.9

The whole production cycle of aluminum, from melting till aging and recycling, is shown in Figure 2.2 (Furu, 2012).

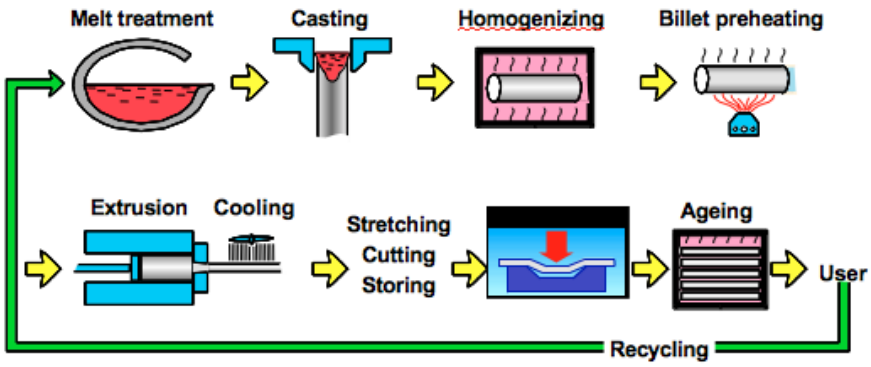

Figure 2.2: The production cycle of the aluminum profiles.

2.2.3 Precipitation hardening Al-Mg-Si alloys

A general description of precipitation hardening of an Al-Mg-Si alloy follows the sequence given below (Solberg, 2011):

$$\text{Saturated } \alpha \rightarrow \text{GP1} \rightarrow \beta\text{''} \rightarrow \beta\text{'} \rightarrow \beta(\text{Mg}_2\text{Si})$$

The different particles have the following structures and features (Solberg, 2011):

GP1: These particles are usually spheres of Mg and Si. Often monoclinic and partially coherent needles along the $< 100 >$ direction.

β'': These monoclinic particles are partially coherent needles along the $< 100 >$ direction in the aluminum matrix. The phase is usually described as Mg_5Si_6, but recent research show that some aluminum would also be a part of this phase.

β': These particles have hexagonal structures and are partially coherent rods. When maximum is achieved, the structure is a mix of β'' and β'. There have been found four different β' particles.

β: These are Mg_2Si particles with a cubic structure. The particles are squared and incoherent plates, providing strength to the material by increasing the energy needed by dislocations to break the Mg-Si bondings.

The addition of alloying elements contribute to the resulting strengthening. In this 6xxx series by adding Magnesium, the solid-solution strengthening properties increase. Strength and ductility are further enhanced by the addition of Iron and Cu. Cu and Ir also influence the surface finish together with Zn. Corrosion resistance is enhanced by adding Ir, Mn, Cu and Zn. The high Mn content in the AA6082 alloy give a very distinct fibrous microstructure, as shown in Figure 2.3. This fibrous microstructure provides higher strength in the extrusion direction. Mn also works as a grain refiner (Furu, 2012).

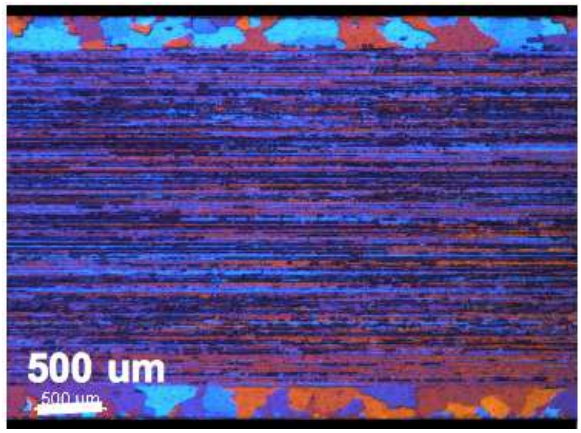

Figure 2.3: Microstructure of AA6082.52.

The importance of fine grains to introduce increased strength of a metal is given by the Hall-Petch equation (2.1) (Callister, 2007).

$$\sigma_y = \sigma_0 + k_y d^{-1/2} \tag{2.1}$$

σ_y is the yield stress, σ_0 is the materials resistance to dislocation movement, k_y is the materials strengthening coefficient and *d* is the grain size in mm (Callister, 2007).

2.3 Hardness

Hardness is the measurement of a materials plastic deformation resistance due to indentation. Hardness given by, *H*, is the ratio between the applied load, *P*, and the representative area, *A*, given in Equation (2.2) (Ambriz et al., 2011).

$$H = \frac{P}{A} \tag{2.2}$$

The indentation used in this paper is the Vickers hardness number *HV*. *HV* is given by a pyramidal square-based indenter that is calculated with the true contact area. The relation of *HV*, where *d* is the indent diagonal in mm, is given by Equation (2.3).

$$HV = 1.8544\frac{P}{d^2} \tag{2.3}$$

Hardness testing is a frequently used mechanical test. They are simple, inexpensive and the tests are nondestructive. Data given by hardness tests can give estimations of other mechanical properties of the material (Callister, 2007).

2.4 Surface roughness

The surface of fatigue specimens are one of the most important variables affecting the fatigue resistance. To sharp or to large notches reduces the fatigue life drastically, given in more detail in Section 2.7.4, (Callister, 2007). The parameters given from the measurements are used to characterize the surface roughness, and in particular the average roughness, R_a, the maximum height of the profile, R_t, and the average distance between the highest peak and lowest valley, R_z, calculated in accordance to ISO 4287.

2.5 Welding of aluminum

Aluminum and its alloys are highly suitable for many manufacturing applications, and the breakthrough came in the 1940s with the introduction of the metal inert gas welding method. This

made it possible to make high strength welds without corrosive fluxes at high speed in all positions. Aluminum alloys have prevailed in the aerospace industry since its beginning, and is used in applications from rocket casings to space station modules. Today, the automotive industry has started to integrate aluminum alloys into vehicles to provide desired light-weighting without compromising performance or safety (Sapa, 2012).

Aluminum has also been integrated into a growing number of corrosion-resistant applications, especially in the oil, gas, water and chemical industry. In addition welded aluminum can also be found in electronics, packing and architecture (Sapa, 2012).

When welding aluminum, it is important to remember that aluminum have unique characteristics that needs to be taken into account when welded. Aluminum alloys are susceptible to hydrogen porosity when welded, which leads to hydrogen dissolving unto the molten weld pool and produce gas pores upon solidification. By using inert gas as a shield during welding, keeping the aluminum clean and dry and avoiding condensation, can prevent this. Thermal conductivity is about six times that of steel. This means that the heat input while welding must be more intense to keep the welding efficient. As the thermal expansion is twice that of steel, it must be taken into account that solidification shrinkage is six percent by volume. This creates larger distortions and weld crater size. If all of these characteristics are taken into consideration, the welding of aluminum is not difficult (Sapa, 2012).

Various methods of welding influences the weld geometry, residual stresses and defects. The combination of these three welding factors determines the quality of the weld and the resulting fatigue life. In addition, temperature and environment would affect the fatigue life of any specimen (Haagensen, 2008).

2.5.1 Metal Inert Gas welding - MIG

The most commonly welding method for structural components and constructions are metal inert gas welding – MIG (Haagensen, 2008). MIG welding is a fusion welding method where two pieces of metal are joined together by melting and fusion, illustrated in Figure 2.4.

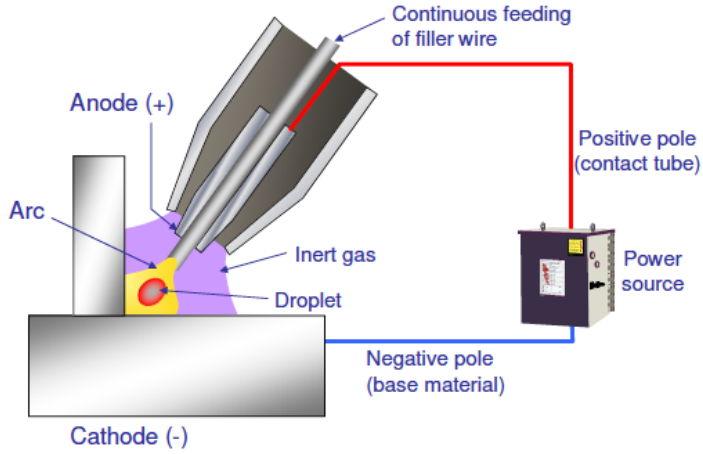

Figure 2.4: Metal inert gas welding method (Myhr, 2013).

The fusion requires an intense local heating source. The minimum rate of energy release per unit area, *qw*, required to maintain a molten state of radius, *r*, is given by Equation (2.4) (Lancaster, 2002).

$$qw = \frac{AkT_m}{r} \tag{2.4}$$

Here k is the thermal conductivity, T_m is the melting temperature and A is a factor that depends on the welding speed, weld size and thermal diffusivity. The weld pool size is limited to be large enough to fuse the edges of the weld and to be manageable (Lancaster, 2002).

MIG welding uses a consumable metal wire electrode protected by an inert gas shield. An axial flow in the welding arc column is desirable as the gas flow protects the molten metal from contamination by atmospheric Ni and O. In MIG welding the electromagnetically induced flow gives the arc a stiffness that is resistant to deflection by external forces. This flow then converts to a stagnation pressure where it impinges on the weld pool. This pressure generates an arc force that ensures good penetration of the molten weld into the workpiece. The arc force must not be to high as that would create an instability and can in extreme cases blow the molten metal out of its proper location (Lancaster, 2002).

Welding with a consumable wire, makes the wire work both as an electrode and as a conductor for the arc current. This provides a heat source and a source of liquid filler metal at the location that are to be welded. The transfer operates in a free flight mode (Lancaster, 2002).

2.5.2 Welding metallurgy

Features and defects contributing to the loss of properties after welding includes the following (Lancaster, 2002):

- Gas porosity.
- Oxide inclusions and oxide filming.
- Solidification (hot) cracking or hot tearing.
- Reduced strength in the weld and HAZ.
- Lack of fusion.
- Reduced corrosion resistance.
- Reduced electrical resistance.

The heat affected zone (HAZ), illustrated in Figure 2.5, is the area with the highest loss of strength due to grain growth during welding. Mg, Ti, Zr and Sc are added to promote fine grain size as these elements forms finely dispersed solid particles in the weld metal. These particles act as nuclei on which the grains form as the solidification after the welding proceeds (Lancaster, 2002).

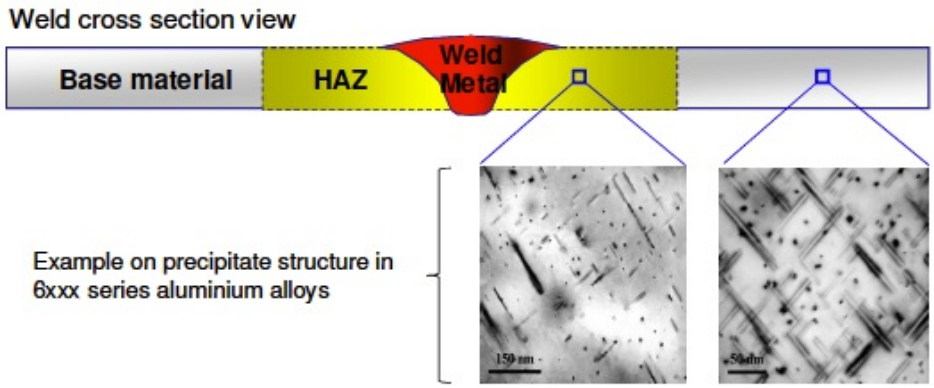

Figure 2.5: General characteristics of single sided butt welding (Myhr, 2013).

Welding of aluminum can cause some problems. This is mostly due to the heat input during welding. Closest to the weld, the temperature will reach high values that leads to homogenization of an aged alloy. In the following cooling period, the big precipitates would gather at the grain boundaries. This leads to a significant reduction in strength in the HAZ. Further out in the alloy where the temperature is lower, the alloy will lose strength due to overaging, as the β" transforms into β' (Solberg, 2011).

Al-Mg-Si alloys are suitable for welding as 80 percent of the strength recovers in a couple of months due to cold hardening (Solberg, 2011).

Filler alloy selection is also important when welding aluminum. The factors for choosing the right filler metal includes freedom from hot cracking, weld metal strength and ductility, corrosion

resistance, weld performance at elevated temperatures, weld metal fluidity, MIG electrode wire feedability and weld metal color match with base metal after anodizing (Sapa, 2012).

Unless the base material that is to be welded are either annealed or as-cast, the fusion welding decreases the strength of both heat treatable and non-heat treatable alloys. The properties of the weld bead, the mix of filler metal and base metal, are influenced by quality, rate of solidification and composition. A high solidification rate gives finer microstructure and better mechanical properties (Sapa, 2012).

2.6 Tensile properties

The magnitude of an imposed stress affects the way a structure deforms. For most metals, when stressed in tension, stress and strain are proportional to each other where the metal is deformed elastically. Hooke's law, Equation (2.5), describes this relationship (Callister, 2007).

$$\sigma = E\epsilon \tag{2.5}$$

σ is the applied stress, ϵ is the strain and the constant E is the modulus of elasticity or Young's modulus. Beyond the elastic limit, the material is deformed plastically with permanent deformation. Ductile materials experience so-called "necking" when deformed plastically followed by rupture of the specimen. Figure 2.6 show a sketch of a typical stress-strain curve of aluminum (Callister, 2007).

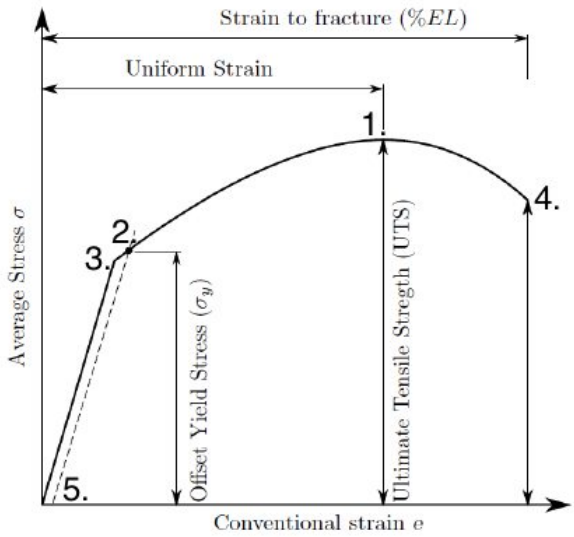

Figure 2.6: A typical stress-strain curve (Skorpen, 2011).

1. The ultimate tensile strength.
2. The proportional limit where the initial departure from linearity occurs.
3. The elastic limit, also defined as yield strength, σ_y, given in MPa (or psi).
4. The point of rupture.
5. The 0.002 strain offset, giving the yield strength at 0.2 % offset, $\sigma_{y0.2}$.

The fracture happens where the shear stress is largest, the 45° angle between the fracture plane and the applied stress. Ductile fractures results from crack growth where small microvoids nucleates in the centre of the specimen. These microvoids grow as the applied stress increases until the microvoids merges and and creates a crack. When this crack reaches a certain length, the specimen fractures (Callister, 2007).

2.7 Fatigue

Since 1850, fatigue has been recognized as the cause of failure by fracture of metals subjected to a repetitive fluctuating stress over a period of time. The stress applied is usually lower than the required stress to cause fracture by a single application of load. Todays industry requires a great amount of equipment for automobiles, aircrafts, turbines, pumps, etc, subjected to a number of vibrational and repeated loadings. Research states that fatigue is the cause of at least 90 percent of all in service failures due to cyclic mechanical stress. A fatigue failure often occurs without obvious warning, in contrast to ductile fracture, as it does not undergo a plastic deformation that indicates that a fracture may happen before it actually happens (Dieter, 1984).

There are three basic factors necessary to cause fatigue failure. These are as follows:

1. Maximum tensile stress of sufficiently value.
2. A large enough variation of fluctuation in applied stress.
3. A sufficiently large number of cycles of the applied stress.

In addition to these three factors other variables as stress concentrations, temperature, corrosion, overload, metallurgical structure and different stresses will alter the fatigue conditions. As the nature of a fatigue failure depends on many different variables, fatigue data is essentially from an empirical point of view (Dieter, 1984).

2.7.1 Stress cycles

There exists many types of fluctuating stresses, which can be divided into three basic categories. The most common is the completely fully reversed cycle of stress of sinusoidal form. This is an idealized situation produced by the R.R. Moore rotating-beam fatigue machine that simulates what a shaft may encounter during service. Figure 2.7 represents this reversed stress cycle (Campbell, 2008).

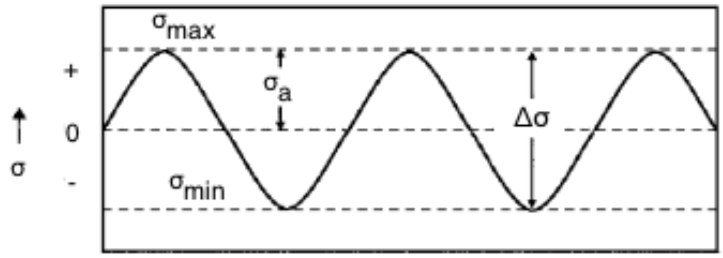

Figure 2.7: Fully reversed cycle.

In this case the maximum and minimum stresses are equal, giving the stress ratio R = -1 from Equation (2.6).

$$R = \frac{\sigma_{min}}{\sigma_{max}} \tag{2.6}$$

In a repeated stress cycle scenario the maximum stress, σ_{max}, and the minimum stress, σ_{min}, are not equal. The stresses can both be in tension, both in compression or of opposite signs. Tensile stress is here considered positive, while compression is negative. Figure 2.8 shows a typically tension-tension stress cycle (Campbell, 2008).

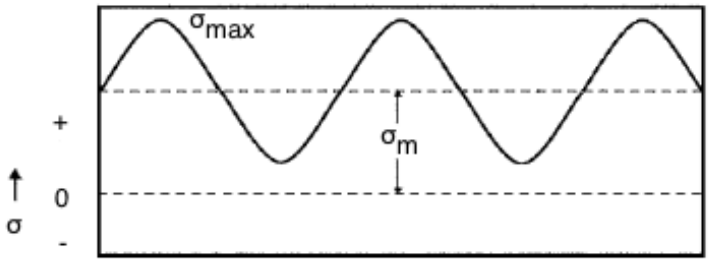

Figure 2.8: Tension - tension cycle.

The most complicated stress cycle is the random or spectrum loading, given in Figure 2.9. This illustrates a more realistic cycle, for example in the case of an aircraft wing that is subjected to periodic unpredictable overloads due to gusts (Campbell, 2008).

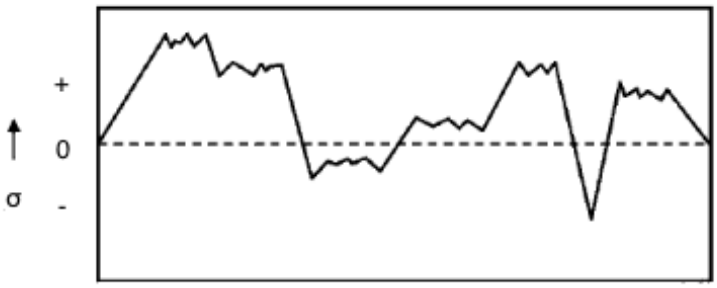

Figure 2.9: Random cycle.

A fluctuating stress cycle can be considered to be made up of two components, a mean stress σ_m, and an alternating stress, σ_a. Where the stress range σ_r, is the difference between the maximum and the minimum stress. These are given in equations (2.7) - (2.9), respectively (Campbell, 2008).

$$\sigma_m = \frac{(\sigma_{min} + \sigma_{max})}{2} \tag{2.7}$$

$$\sigma_a = \frac{\sigma_r}{2} = \frac{(\sigma_{max} - \sigma_{min})}{2} \tag{2.8}$$

$$\sigma_r = \sigma_{max} - \sigma_{min} \tag{2.9}$$

In addition there are two quantities used in presenting fatigue data in terms of stress ratios. Either the stress ratio, Equation 2.6 or the amplitude ratio, Equation 2.10 (Campbell, 2008).

$$A_r = \frac{\sigma_a}{\sigma_m} = \frac{1 - R}{1 + R} \tag{2.10}$$

2.7.2 S-N curve

The fatigue life of metals are usually presented in a S-N curve, a plot of applied stress against the number of cycles to failure, using a logarithmic x-axis. S-N curves of a typical ferrous and nonferrous metal are given in Figure 2.10 (Campbell, 2008).

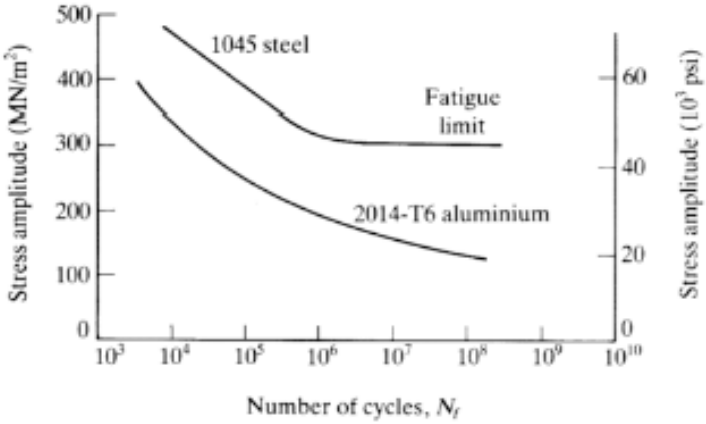

Figure 2.10: A typical fatigue curve with mild steel as the ferrous metal and aluminum as the nonferrous metal.

This type of presenting fatigue data is mainly used for high cycle fatigue, where the number of cycles to failure is higher than 10^5. A low-cycle fatigue is in the region where $N < 10^4$. In the low-cycle fatigue region, tests are performed with controlled cycles of plastic and elastic strain instead of controlled load or stress cycles. Fatigue life under high cycle fatigue are generally controlled by crack initiation. This is thought to be influenced by surface condition, including roughness, residual stress and microstructural inhomogeneities that can cause stress concentrations.

The fatigue limit (or endurance limit) of a material indicates at what stress it presumably can endure an infinite number of cycles without failure. For nonferrous metals without this fatigue limit, the fatigue strength at an arbitrary number of cycles is used to characterize the fatigue properties, usually set to $N = 10^8$ (Campbell, 2008).

2.7.3 Crack initiation and propagation

The fatigue failure is characterized by three distinct steps:

1. Crack initiation
2. Crack propagation
3. Final failure

The initiation point for a fatigue crack is usually a point of high stress concentration such as a notch, a sharp corner, or a metallurgical discontinuity like an inclusion. In addition the cyclic loading produces microscopic surface discontinuities that results in dislocation slip steps that contributes as a stress concentrator and may become a crack initiation site. The fatigue fracture surface looks like a brittle fracture with no gross deformations visible on the surface. A fatigue

failure can be recognized by having two regions, where the smooth region has its features from the rubbing action of the crack propagation, and the rough region is where the member has failed in a ductile matter. Striations and beach marks are typical features of fatigue failures and indicate the point of initiation as a series of rings progressing inward from the initiation point. The fracture surface is usually perpendiclar to the direction of the principle applied tensile stress (Dieter, 1984).

Beach marks often represent an interruption of the load, and therefore represents a period of time over which the crack has grown. Striations on the other hand represents each load cycle the material has been through during the crack propagation. The width of the striations depends on the stress range, where the width increases with increased stress range. These marks are usually found at the region of slow crack propagation, and not in the region of rapid failure (Callister, 2007).

The difference between a welded and a non-welded structure is that the fatigue life of a welded structure is dominated by the crack propagation life, Equation (2.11), and the life of the non-welded structure is more or less purely crack initiation life, given in Equation (2.12) (Dowling, 2012).

$$N = N_p \tag{2.11}$$

$$N = N_i \tag{2.12}$$

2.7.4 Fatigue life

Fatigue behavior is highly sensitive to a number of variables, as mentioned above. These variables includes mean stress levels, geometrical design, size effects, the environment and metallurgical variables (Callister, 2007).

The mean stress affect fatigue life by decreasing the fatigue life when it is increased, as shown in the S-N curve in Figure 2.10 (Callister, 2007).

The design and geometry of a component have a significant influence on the fatigue behavior. Any geometrical discontinuities or notches act as stress raisers that may decrease the fatigue life. The smaller the radius of a notch, or sharper the discontinuity is, the stress concentration becomes higher. Therefore a poor design would be a component with sharp edges, while a good design would exhibit large radii of curvatures at the point where there is a change in design (Callister, 2007).

To improve the surface and thereby the fatigue life, different surface treatments can be utilized. The most effective method is to introduce residual compressive stresses within a thin layer of the outer surface. One process to do this is by shot peening, a process that uses small, hard particles with the diameter within 0.1 to 1.0 mm that are projected at high velocities onto the surface, described in more detail in Section 2.8.2. This leads to deformation and residual stresses, more details are given in Section 2.7.7 (Callister, 2007).

Two environmental factors that may also affect the fatigue life are temperature and corrosion. Thermal fatigue is usually induced at elevated temperatures, and can happen without any mechanical stresses, but fluctuating thermal stresses. The thermal stress, σ, depends on the coefficient of thermal expansion, α_l, modulus of elasticity, E, and temperature change, ΔT, the relationship is shown in Equation (2.13) (Callister, 2007).

$$\sigma = \alpha_l E \Delta T \tag{2.13}$$

Corrosion fatigue is the failure that occurs when both a cyclic stress and a corrosive environment are present. Chemical reactions happens on the surface of the material, creating small pits that may act as stress raisers and become crack initiation sites. The crack propagation rate is enhanced by the corrosive environment (Callister, 2007).

2.7.5 Goodman diagram

The fatigue life of a material can be estimated by using the Goodman relation, Equation (2.14) and the Goodman diagram (also called Haigh diagram), Figure 2.11 (Dowling, 2012).

$$\frac{\sigma_a}{\sigma_{ar}} + \frac{\sigma_m}{\sigma_{uts}} = 1 \tag{2.14}$$

The Goodman diagram below represents fatigue data by plotting the endurance limit of the material on the y-axis, σ_{ar}, and drawing a straight line to the ultimate tensile strength, σ_{uts}, on the x-axis. Below this line is the safe operating region, where a chosen mean stress, σ_m, applied relates to the maximum applied stress amplitude, σ_a, allowed in the safe region. The limiting mean stress is found by drawing a straight line from the yield strength on the x-axis to the yield strength on the y-axis. In the area above the Goodman line, the material may fail during operation. The Goodman relation is generally conservative, hence the error is such that it causes extra safety in the fatigue life estimations (Dowling, 2012).

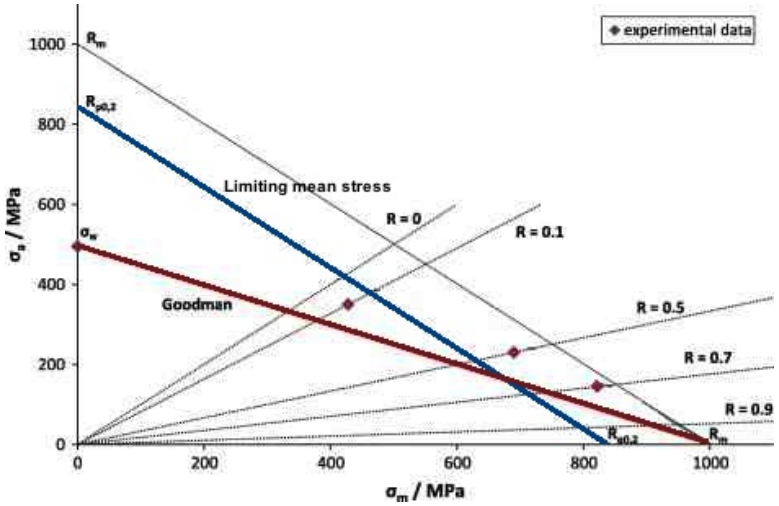

Figure 2.11: Goodman diagram showing the region of safe operating below the Goodman line and the limiting mean stress, and the region where the material may fail if operated at stresses above these lines (Kovacs et al., 2013).

2.7.6 Cyclic deformation

When a metal and its alloys are subjected to cyclic loading, the microstructure changes and leads to alterations in their mechanical, magnetical, electrical and other properties. These changes occur mostly during the earliest cycles, leading to a somewhat saturated state which remains more or less constant for the rest of the materials' fatigue life. A result of this can also be either cyclic softening or cyclic hardening. The microscopic changes are numerous extrusions and intrusions associated with persistent slip bands. For aluminum, with a high stacking fault energy, at high cyclic loads, slip occurs on multiple slip systems. The strengthening phases that forms are Guinier-Preston (GP) zones and β particles that during deformation is cut by dislocations, and are piled up at the grain boundaries. This creates microstructural stress concentrations. When the stress concentration exceed the crack nucleation stress at the grain boundaries, an intergranular fracture starts (Klesnil and Lukás, 1992). As the microstructure of materials often vary with direction, due to for example extrusion and rolling, the fatigue resistance may be decreased when the stress is normal to the longest direction of the grains (Dowling, 2012).

2.7.7 Residual stresses

A material can exhibit internal stresses, called residual stresses. Compressive residual stresses are beneficial when it comes to fatigue life, unlike tensile residual stresses. A compressive residual stress can be introduced to the material by stretching the thin surface layer, by yielding it in tension. As the underlying material then tries to recover its original size by elastic deformation, the surface layer will be forced into compression. Different methods are used to introduce

compressive residual stresses, like presetting (bending), cold rolling or shot peening. A smooth surface resulting from careful machining will in general improve fatigue strength, but it can also introduce harmful tensile residual stresses in the near surface layers. Welding often results in geometries that act as stress raisers and the uneven cooling of the molten metal often result in residual stresses. The microstructure of the weld may also include porosity and other small flaws that reduces fatigue life (Dowling, 2012).

Figure 2.12 shows the situation for $R = 0$ where no residual stresses are introduced (a), and the ideal case when compressive residual stresses are formed (b) and the effect on fatigue life (Cheng et al., 2003).

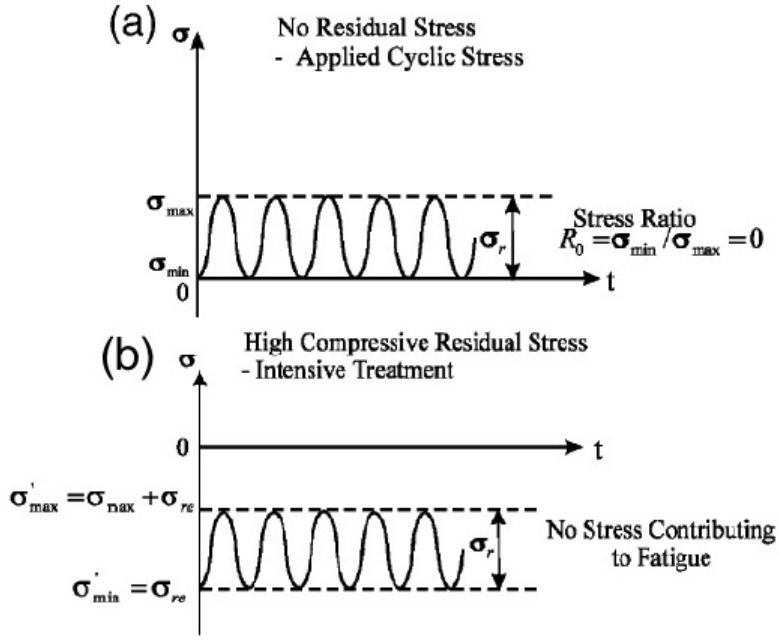

Figure 2.12: For the stress ratio, R = 0, (a) shows the case of no residual stresses. (b) shows the ideal case when compressive residual stresses are introduced.

2.7.8 Effect of welding on fatigue strength

The different methods of welding influences the weld shape, residual stresses and defect sizes and shapes. The combination of these three factors determines the quality of the weld and hence the resulting fatigue life. In addition, both temperature and environment would also affect the fatigue life of any specimen (Haagensen, 2008).

A weld can reduce the fatigue strength of a component drastically, primarily caused by weld defects, welding stresses and reduced static strength of the material near the weld, in the HAZ. The stress concentration factor (SCF) of a butt weld is only marginally higher than the non-welded

plate. A high local stress at the weld can be caused by the overall shape of the component and/or by the micro geometry at the weld toe. Weld defects at the critical region of the high stresses at the weld toe also contribute to the reduced fatigue strength. In addition, a high tensile residual stress due to metal shrinkage upon solidification may cause a further reduction in fatigue strength (Haagensen, 2008).

All of these factors contribute to an early crack initiation, and thereby implicates that the fatigue life of welded structures are spent in crack propagation as mentioned earlier, Equation (2.11).

Geometry of the weld contributes to the reduction of fatigue strength, where the weld toe radius, weld angle, attachment length and plate thickness all have a crucial role. The greatest influence comes from the weld toe radius. A decrease in the weld radius from 3 mm to 0.5 mm, decreases the fatigue life by a factor of 1.3, almost reducing the fatigue life by half (Haagensen, 2008).

Angular misalignment, Figure 2.13, created by the weld also creates an extra stress concentration factor by introducing a bending moment, and thereby reducing the fatigue life (Haagensen, 2008).

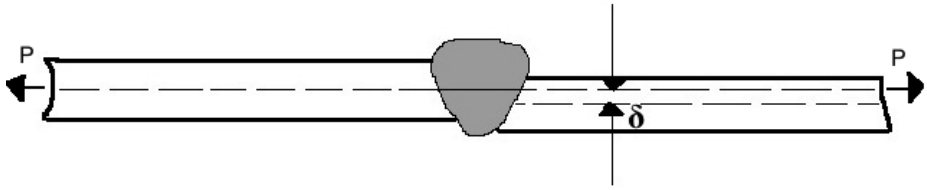

Figure 2.13: Misalignment between two welded plates. The centre alignments differ with a factor δ.

Cold lap defects are one of the most common defects found in welded aluminum. These cold laps are often caused by an oxide layer on the surface that has a higher temperature of fusion than the aluminum, where the break down of this layer is not accomplished. This leads to the welding becoming incomplete and introduces an additional weakness in the component (Haagensen, 2008).

2.8 Post weld treatment

Age-hardened aluminum alloys' mechanical properties at room temperature are directly linked to the number of density and size distribution of the hardening precipitates that forms during artificial aging (Myhr et al., 2004).

After welding the strength of the material is decreased due to the heat input during welding, as the thermal stability of the hardening precipitates is low, and these dissolve during welding. To increase the strength i.e. promote the formation of β" precipitates or introduce residual compressive stresses (Myhr et al., 2004), two methods will be discussed in the following sections; post weld heat treatment and shot peening.

2.8.1 Post weld heat treatment

Post weld heat treatment (PWHT) involves either both solution heat treatment and aging or just aging. This depends on the temper condition of the base material prior to welding. A PWHT involving solution heat treating and aging have shown better results than just aging (Bertini et al., 1998), but post weld aging has its advantages as it is easily performed and does not require high temperatures and water quenching which can introduce distortion and residual stresses (Sapa, 2012).

The heat-treatable aluminum alloys will have an increase in strength of the HAZ by PWHT. The weld metal will usually not be affected as much as the base material. The amount of filler metal will therefore affect the final strength (Sapa, 2012).

During artificial aging (AA) of these alloys, a high density of fine needle-shaped β" particles are formed uniformly in the aluminum matrix, as shown in Figure 2.14 (a). This is the dominating hardening phase in T6 heat treated Al-Mg-Si alloys. Since these particles are thermodynamically unstable during welding, the smallest particles will start to dissolve in parts of the HAZ where the temperature is higher than $250°\mathrm{C}$, while the larger particles starts to grow. A full achievement of reversion of the β" particles are found close to the fusion line. At the location where the temperature reaches $250 - 480°\mathrm{C}$, coarse rod-shaped β' precipitates may be formed, seen in Figure 2.14 (b) (Myhr et al., 2004).

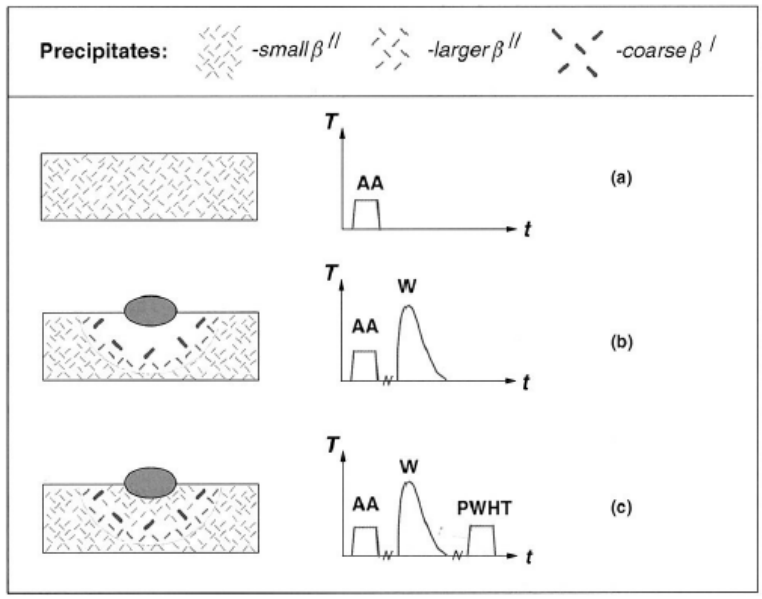

Figure 2.14: The effect of PWHT on the microstructure of Al-Mg-Si alloys. AA: artificial aging, W: Welding, PWHT: PWHT (Myhr et al., 2004).

When the welding is succeeded by a PWHT, Figure 2.14 (c), a reprecipitation of hardening β"

particles will take place where the temperature reached its peak temperature. This reprecipitation depends on the matrix vacancy concentration and the level of Si and Mg in solid solution. The most extensive reprecipitation will take place in the fully reverted region close to the weld fusion line, as the combined effect of a high solute content and high concentration of quenched-in vacancies are found in this region. At the same time, the renewed β" formation will be suppressed in parts of the HAZ where the temperature was lower during welding. The aluminum matrix in these regions are depleted with respect to solute and vacancies. This results to the development of a permanent soft region within the HAZ, still after PWHT (Myhr et al., 2004).

2.8.2 Shot peening

Shot peening is used to induce compressive residual stresses in the surface and near-surface layers to limit the reduction in fatigue properties. It is a cold working process where the surface is bombarded with small spherical shots, made of either cast steel, conditioned cut wire or a ceramic media. Every shot acts as a tiny peening hammer, creating small indentations or dimples to the surface. When the shots strike the surface the material is yielded in tension, making the fibers in the surface below to try to restore the surface in its original shape, hence creating a hemisphere below the dimple where the material is highly stressed in compression (Locke et al., 2005), shown in Figure 2.15 (Kopeliovich, 2012).

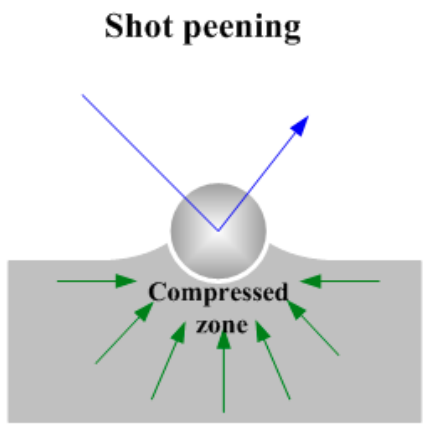

Figure 2.15: A dimple created by shot peening and the resulting compressive zone.

As the shot peening produces plastic deformation changes in the internal structures of the deformed grains. The effect of the shot peening depends on various variables including shot size, nozzle pressure, impignant angle, coverage, shot flow rate and distance of the nozzle from the surface. These variables are integrated in the form of Almen intensity (Mehmood and Hammouda, 2007).

A post-fracture analysis is required to quantify the effect of the shot peening. As well, a measurement of how much compressive stresses are induced must be quantified (Locke et al., 2005).

3 Literature Review

A literature research was conducted on the different topics of this thesis. As there have not been done to much research on these topics, especially for the AA6082 alloy, similar aluminum alloys have been included to give an indication of what to be expected.

3.1 Mechanical properties of welded AA6082

Moreira et al. (Moreira et al., 2007) tested the influence of metal inert gas welding on Al6082-T6. The welding parameters used were 128 A, 17.1 V, 700 mm/min and the Argon had a flow of 20 L/min. The filler metal used were AWS ER5356. The yield strength of the base material was found to be 276.2 MPa, while for the welded specimens the yield strength was 176.8 MPa. The ultimate tensile strength of the base material was found to be 322.9 MPa, and for the welded specimens it was 210.0 MPa. All of the base material specimens failed in the 45° shear plane. The welded specimens ruptured outside the welding seam in the heat affected zone.

The microhardness profile of the MIG welded Al6082-T6 specimens showed that the softest areas were at the weld centre line, and in the heat affected zone, both giving a Vickers hardness of 50 HV. The base material had values over 90 HV reached 16 mm from the centre of the weld (Moreira et al., 2007).

Morgenstern et al. (Morgenstern et al., 2006) found the 0.2% offset yield strength of as welded AW6082 T6 to be 287 MPa and the ultimate tensile strength to be 318 MPa. The hardness profile using Vickers hardness (HV-5) showed the softest area of the fully penetrated butt weld was found in the heat affected zone with a value of 57 HV. Another soft zone was measured in the centre of the weld at 64 HV and reaches its maximum value of 105 HV, 13 mm from the centre of the weld.

Richter-Trummer et al. (Richter-Trummer et al., 2008) did a residual stress measurement on a 6082-T6 MIG butt welded thin plate, with the same welding parameters as Moreira (Moreira et al., 2007). By using the contour method and the sectionoing method, both non-destructive, the

maximum longitudinal residual stresses was found near the welding line and had a value of 180 MPa.

3.2 Fatigue of AA6082

Calvin White et al. (White et al., 2005) conducted tension-tension fatigue tests on AA6082.50 in the T6 temper condition, on both square and round cross sectioned specimens. Both specimen types had hourglass profiles with no uniform gage section. The yield strength of the specimens was found to be 309.6 MPa and the ultimate tensile strength was 334.6 MPa. The fatigue testing was conducted on a Zwick-Roell resonance fatigue tester with the stress ratio, *R*, was equal to 0.1. The round specimens grounded circumferentially with an abrasive size of 1 μm showed the lowest fatigue strengths than the other specimens. It was also found that the round specimen, as machined, had better fatigue resistance than the ones grounded and polished longitudinal. The square specimens showed a higher fatigue strength than the round circumferential grounded specimens, but lower strength than the other round specimens. The baseline fatigue strength of the AA6082.50 at $N = 10^6$ was 255 MPa. It was also found that the corners of the square cross sectioned specimens did not diminish the fatigue life of AA6082.50. There was not found any correlation between the location of the crack initiation and the fatigue strength of the specimens.

3.2.1 Fatigue of welded AA6082

The fatigue data given by Moreira et al. (Moreira et al., 2007) for the MIG welded Al6082-T6 show a decrease in fatigue life compared to the base material. The fatigue tests were conducted in tension-tension with the stress ratio, *R* = 0.1 and a frequency interval of 7-26 Hz. The tests had a high scatter of the results, giving a fatigue life of 46,645 cycles at 106.1 MPa. The specimens still had the excess material after welding.

Morgenstern et al. (Morgenstern et al., 2006) investigated MIG welded joints of AW-6082 T6 under both fully reversed and pulsating axial loading, R = -1 and R = 0 respectively. The tests were under load control with a frequency of 25-30 Hz. The fatigue life at $N = 2x10^6$ cycles and R = -1 was 98 MPa for the fully penetrated butt welded specimens. For R = 0, the fatigue life at $N = 2x10^6$ was 72 MPa.

3.3 Post weld heat treatment on fatigue behavior

A modeling of the microstructure and strength in Al-Mg-Si alloy during aging, welding and post weld heat treatment (PWHT) was done by O. R. Myhr et al. (Myhr et al., 2004). The alloy used was AA6005 in the T6 temper condition. The welding was simulated by Gleeble simulations. The weld simulated specimens was post weld heat treated either 0.5 h or 5.5 h at $185^{\circ}\mathrm{C}$. Hardness profiles was made before and after PWHT, revealing that the soft zones of the HAZ decreased after PWHT especially for the ones heated for 5.5h. Conversely the PWHT had no effect on the minimum hardness level in the HAZ. This is explained by the low concentration of quenched-in

vacancies and low solute content where the reprecipitation of hardening β " particles could take place. This may suggest that the fatigue behavior would be more or less the same as for as welded specimens.

Bertini et al. (Bertini et al., 1998) investigated the influence on post weld aging (PWA) on the fatigue behavior of MIG welded 6063-T6 aluminum alloy. The filler metal during welding was 4043. A microhardness (Vickers HV-0.05) profile found the extension of the HAZ to be about 6 mm, with the minimum value about 4 mm form the centre of the weld, 66 HV as welded. The solution treatment was set to 55 min at $520°\mathrm{C}$ and aging for 4 h at $175°\mathrm{C}$. After solution and aging treatment the material was almost completely homogenized, giving the minimum hardness of 86 HV 3 mm from the centre of the weld. The yield strength of the as welded specimen was 100 MPa, while after PWA it was measured to be 200 MPa.

The fatigue tests were performed on a electrohydraulic Instron machine with R = 0.05 at a frequency of 30 Hz. The effect of PWA on the fatigue life at $N = 2x10^6$ did not show any significant difference. At $N = 2x10^6$ the as welded had a stress of 71.4 MPa and the PWA specimens had 70.2 MPa (Bertini et al., 1998).

Another study on the AA7075 done by Balasubramanian et al. (Balasubramanian et al., 2008) reports the influence of pulsed current welding and post weld aging on fatigue behavior. Continuos and pulsed MIG welding, single butt, with Argon (16 L/min) as shielding gas was investigated. The filler rod AA5356 was 1.6 mm in diameter. Welding voltage, speed and current was 30 V, 150 mm/min and 200 A respectively. The post weld aging was performed at $125°\mathrm{C}$ for 24 h. Yield strength of the base material was found to be 417 MPa and of the MIG welded specimen 303 MPa. The ultimate tensile strength was found to be 520 MPa and 380 MPa for the base material and the welded specimens respectively. PWA showed an increase of yield and ultimate tensile strength of about 8-10 %. The PWA also had a positive affect on the hardness, with a increase of 15-20 % compared to the as welded specimens. The pulsating MIG welding showed better results than the continuos MIG welding.

The fatigue tests were done using a servo hydraulic controlled, 100 kN capacity fatigue testing machine with a frequency of 10 Hz and R = 0. Post weld aging also showed a decrease in fatigue crack growth, nearly 20-25 % increment in fatigue life irrespective of welding technique (Balasubramanian et al., 2008).

3.4 Shot peening on fatigue behavior

To investigate crack growth in a shot peened material, Locke et al. (Locke et al., 2005) have quantifyed the effectiveness of the shot peening process, the different coverage levels and intensities on the fatigue crack growth rates of 7050-T7451 an 7075-T7351 aluminum alloys. The depth of the compressive stresses introduced was less than 0.010 inches and the maximum values was in the depth range of 0.0020-0.0030 inches. Constant amplitude testing with R = 0.5 was conducted for both the hourglass and single edge specimens at a frequency of 20 Hz. The intensity of the peening was 0.077-0.078A on the Almen strip. The shots used were steel shots with a diameter of 230R. The peening coverage was 100 and 200 %. For the 100 % coverage, the maximum introduction of residual stresses was -50 ksi (-344 MPa) and for the 200 % coverage maximum

was -55 ksi (-379 MPa). The results in this investigation indicates improved fatigue life of these shot peened specimens.

Mehmood and Hammouda (Mehmood and Hammouda, 2007) did an experimental study of the effect of shot peening parameters on a 2024 aluminum alloy. The parameters optimized included shot size, nozzle pressure, nozzle distance, impingement angle and exposure time. The Almen strip was used to measure the different parameters. The formation of compressive residual stresses was quantified by the hole drilling method. For testing the resulting fatigue life, a four point rotating bending fatigue testing machine of 20 kgm maximum bending moment and 2860 rpm was used. Stress ratio, *R*, was set to -1. The 0.2 % proof yield stress of the alloy was found to be 324 MPa and the ultimate tensile strength was 393 MPa. Three "A" type Almen strips were used; S110, S170 and S230 according to SAE J442, .

The results showed that the Almen intensity of 12A introduced the maximum residual stresses of -242 MPa at the depth of 0.2 mm. The minimum introduced residual stress was 49 MPa at the depth of 1.4 mm. This was obtained with the S230 Almen strip. A considerable improvement in the fatigue life was observed, improving the life with 166 percent at a cyclic stress of 236 MPa (Mehmood and Hammouda, 2007).

Bertini et al. (Bertini et al., 1998) also investigated the influence of shot peeing on the fatigue behavior of MIG welded 6063 aluminum alloy. Shot peening was used to introduce residual compressive stresses with an Almen intensity of 7A on a specimen in the T4 temper condition. To measure the formed residual stresses, a X-ray diffraction (XRD) technique was used. The residual stresses measured at the fusion line was maximum -125 MPa. At a point about 5 mm from the fusion line, the residual stresses measured was -121 MPa. The fatigue tests were conducted as described above in Section 3.3 from the same article. The stress at $N = 2x10^6$ after the shot peening was 88.7 MPa. An increase of fatigue strength of about 25 %.

4 Experimental

4.1 Microstructural analysis

To analyze the grain structures and grain sizes of the extruded sections, the specimens were grind with a grit size increasing from 320 to 2400, with Struers RotoForce4 shown in Figure 4.1. Then the specimens were polished down to 3 μm and anodized with 5 % HBF_4. The microstructure was then investigated in an optical microscope, Leica MEF4M.

Figure 4.1: Struers RotoForce4 used to grind the specimens for microstructural analysis.

The base material was investigated in the longitudinal transverse section of the surface, while the welded material was investigated across the weld, perpendicular to the extrusion direction.

4.2 Hardness

Vickers hardness testing of the base material was done by testing in the middle of the specimen, measuring 3-5 indentations with 1 mm distance apart. The hardness was tested using 1 kg for about 30 seconds with the use of Duramin A-2500 Hardness tester.

Hardness testing of the welded area and the HAZ were done to produce a hardness profile to characterize the extent of the HAZ. The measurements were done with 1 mm distance between each indentation, as illustrated in Figure 4.2.

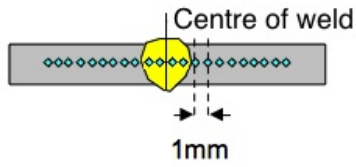

Figure 4.2: Description of how the Vickers hardness testing was conducted.

4.3 Surface Roughness

The surface roughness was measured by using a Mahr Perthometer M2. A diamond head was used to track the peaks and valleys of the specimens, resulting in a surface profile. The perthometer calculated the different parameters, R_a, R_t, R_z over a length L_t. Three measurements were done per specimen. Figure 4.3 shows the perthometer measuring the surface roughness of one of the shot peened specimens of AA6082.50-T6.

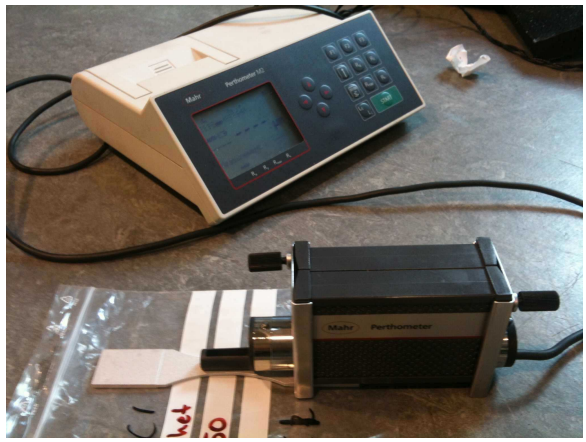

Figure 4.3: Mahr Perthometer M2 measuring the surface roughness of a shot peened specimen of AA6082.50.

4.4 Welding

Metal inert gas welding of the profiles was prepared at SINTEF Materials and Chemistry in Trondheim. Two plates of the same alloy and temper condition were welded together, as shown in Figure 4.4. The filler metal chosen was 5183 ($AlMg_5$). The shield gas used was 4.6 Ar, welding speed was 10 mm/s and there was no gap between the plates when welded. The mean current was 165-170 A, and the potential was 22 V. Before the welding began, both chemically and mechanically removal of oxide layers were done. All of the welding parameters are given in Table A.1 in Appendix A.

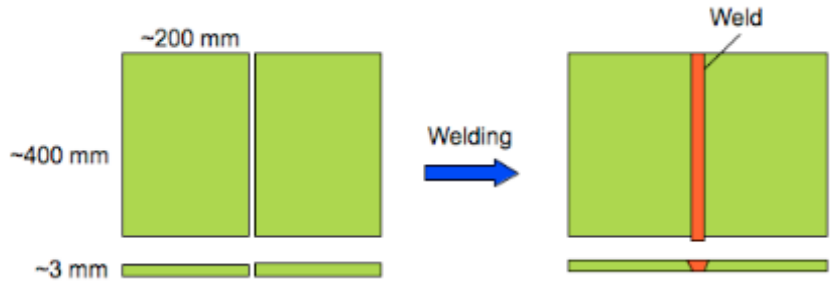

Figure 4.4: Description of the welded aluminum profiles.

Figure 4.5 illustrates the angle between the two welded profiles after welding (Furu, 2012). This misalignment was removed during machining of the fatigue specimens.

Figure 4.5: Illustration of the angle between the aluminum profiles after welding.

4.5 Specimens

The specimen dimensions were chosen according to the American Society for Testing and Materials (ASTM) standard E466, given in Appendix B. The dimensions are given in Table 4.1 and shown in Figure 4.6. The artificial aging of the profiles is given in Figure B.2 also given in Appendix B.

Table 4.1: Dimensions of the specimens for tensile and fatigue testing.

Dimensions [mm]		
Section	Base material	Welded
Radius	60.00	60.00
Width	7.50	7.50
Length	120.00	120.00
Height	20.00	20.00
Thickness	3.00	2.00

Two different specimens were used to test the fatigue strength. Specimens from the base material are similar to the sketch in Figure 4.6. The other specimens are symmetric around the weld, with the center of the weld in the smallest cross section area. The weld is perpendicular to the extrusion

direction. The welded specimens have a smaller thickness due to the removal of excess material from the weld. All specimens were machined at the fine-mechanical workshop at NTNU.

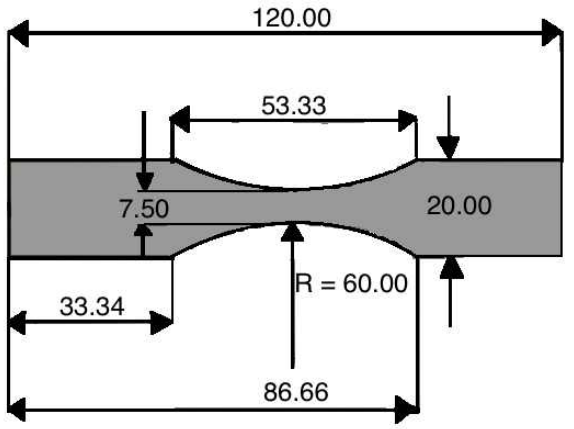

Figure 4.6: Specimen dimensions.

Figure 4.7 and Figure 4.8 show the base material specimen of the AA6082.50-T6 and the as welded specimen of the same alloy, respectively.

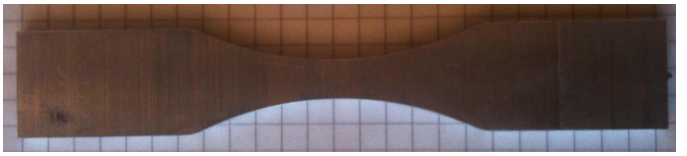

Figure 4.7: Base material specimen AA6082.50-T6.

Figure 4.8: As welded specimen AA6082.50-T6.

Figure 4.9 show the specimen before (top) and after (bottom) being shot peened with glass shots at the fine-mechanical workshop at NTNU, Norway. The as welded specimen show how the specimens were machined and the resulting surface finish due to the shot peening of the surface.

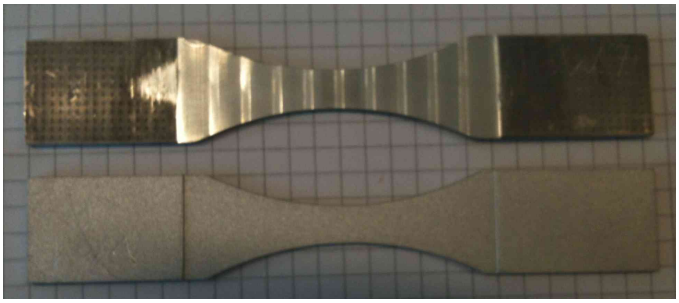

Figure 4.9: The as welded specimen (top) and the shot peened specimen (bottom) of AA6082.50-T6.

4.6 Tensile testing

Tensile tests were carried out in 25 kN, servo-hydraulic MTS testing machine at NTNU, Trondheim, Figure 4.10. The yield strengths and ultimate tensile strengths were derived from the stress-displacement diagrams shown in Section 5.4

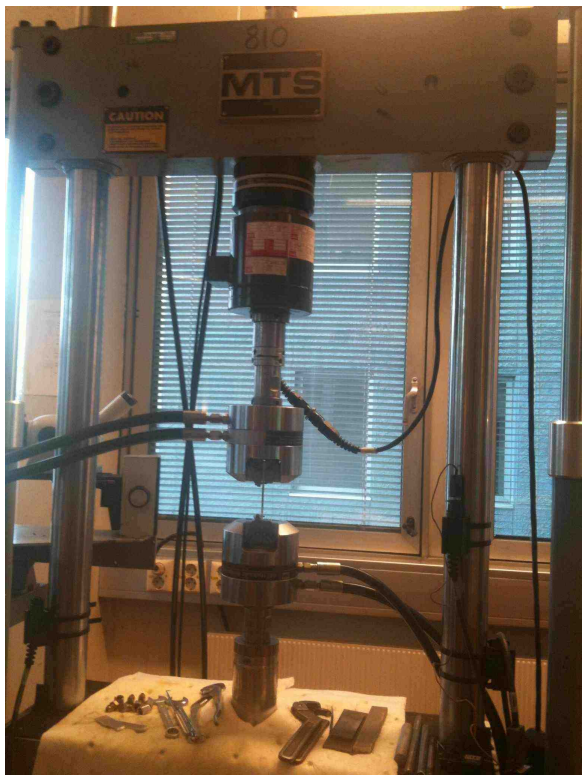

Figure 4.10: 25 kN, servo-hydraulic MTS testing machine used for both tensile and fatigue tests.

To establish the extent of cyclic hardening or softening, a tensile tests were also done on specimens that were deemed run-outs (RO) and for those cycled for about $3.0x10^6$ cycles without fracture for all of the specimen types; base material, as welded, welded + post weld heat treated (PWHT) and welded + shot peening (SP).

4.7 Fatigue testing

Fatigue testings were conducted in a servo-hydraulic MTS testing machine at NTNU, Trondheim, Figure 4.10. A stress ratio of R = 0.1 was chosen so that the fatigue tests were done under tension-tension to avoid any buckling during testing. The frequency used was 25 Hz, a sinusoidal periodic forcing function. The life of the specimens was defined as the number of cycles to failure. The threshold for infinite life was chosen to be 10^7 cycles, deemed run-outs (RO). All tests were done perpendicular to the extrusion direction.

All tests where performed in the high cycle fatigue region, as shown in Figure 4.11 (Klesnil and Lukás, 1992).

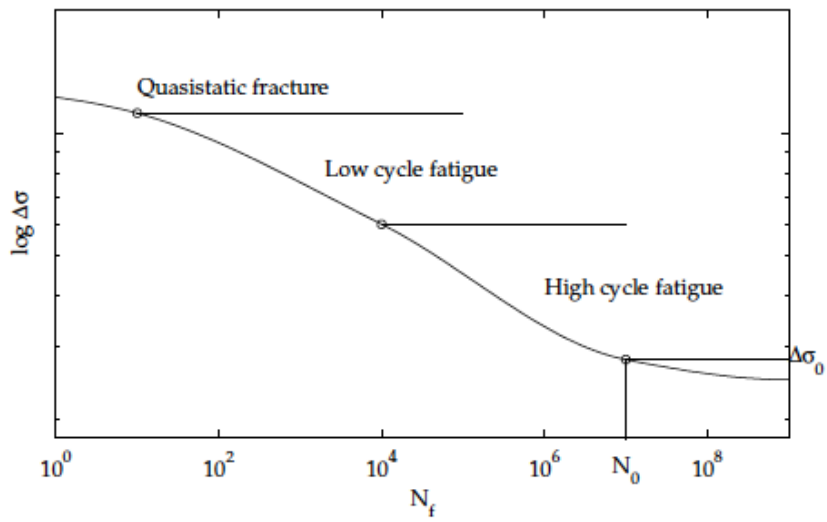

Figure 4.11: Different fatigue testing regions.

4.8 Post weld treatments

4.8.1 Post weld heat treatment

The PWHT was done by using a convection furnace with a rate of 200°C/h until reached 185°C. The temperature was then held for 5 hours. The specimens were cooled by air (Furu, 2012). The PWHT of the specimens took place 6 weeks after being welded. The treatment is similar to the artificial aging of the profiles shown in Figure B.2 in Appendix B.

The Duramin A-2500 Hardness tester was used to measure the hardness of the PWHT specimens.

4.8.2 Shot peening

Shot peening of specimens post welding were conducted at the fine-mechanical workshop with the use of Guyson Formula 1600 machine, 8 weeks after being welded. Shots made of glass were shot at the specimen with high pressure air at 5.5 bar, accelerated through a nozzle directed at the specimens, shown in Figure 4.12.

Figure 4.12: Shot peening of as welded specimens of AA6082.50-T6.

The glass shots used for the shot peening are soda-lime glass, the chemical composition is given in Table 4.2, and other characteristics are given in Table 4.3 (ClemcoNorgeAs, 2009).

Table 4.2: Chemical composition of soda-lime glass used for shot peening given in weight percent.

Compound:	SiO_2	Fe_2O_3	Mg0	CaO	Na_2O	Al_2O_3
Weight percent [%]:	65	0.15	2.5	8.00	14	0.5-2

Table 4.3: Technical data for the soda-lime glass shots used for shot peening.

Size [mm]	Density [g/cm^3]	Shape	Vickers hardness
2.0-0.037	2.2-2.45	Round	669

To estimate the introduced residual stresses, the specimens hardness across the weld post shot peening was determined. The surface roughness of the shot peened specimen was also investigated.

4.9 Fatigue fractography

To investigate the fracture surface of the fatigued specimens, the failed specimens with the shortest and longest fatigue lives were evaluated by using a Zeiss Supra 55 VP scanning electron microscopy (SEM). The acceleration voltage was set to 20 kV and the working distance was 22-16 mm. The crack initiation point were to be localized along with characteristics of stage I and stage II crack propagation.

5 Results

5.1 Microstructure

The extruded profiles of AA6082.52-T6 were investigated by optical microscopy, both the base material and the as welded. Figure 5.1 show the micrographs of the base material to the left, a), taken in the longitudinal transverse section at the surface. In the micrograph a recrystallized layer can be seen along the surface due to homogenization. The micrograph of the as welded plates, b), taken in the extrusion direction, show a quite different microstructure. The recrystallized layer along the surface seems to be larger than for the base material. The grain size in the middle of the plate has also grown large and do no longer exhibit the fibrous structure found in the base material, a). Except for the recrystallized surface layer, the base material has homogenous grain structure, unlike the as welded plates. The depth of both of the recrystallized layers is between 90 - 120 μm.

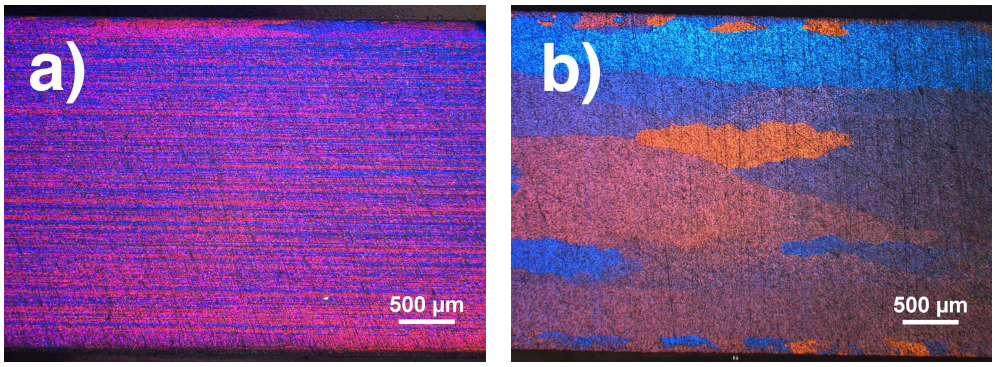

Figure 5.1: Micrographs of the base material, a), and the as welded, b), AA6082.52, T6 temper condition.

Figure 5.2 show all the features of the weld in the micrograph to the left, c). The fusion line can easily be seen as a line separating the weld and HAZ. The micrograph to the right, d) show the different microstructure and composition of the weld bead. The grain size in the HAZ is larger than the ones shown in both the recrystallized surface layer and in the weld. The depth of the recrystallized layer in the HAZ is about 130 μm. The weld, d), has a more uniform grain size, smaller than the ones in the HAZ and larger than the grains in the recrystallized surface layer and in the base material.

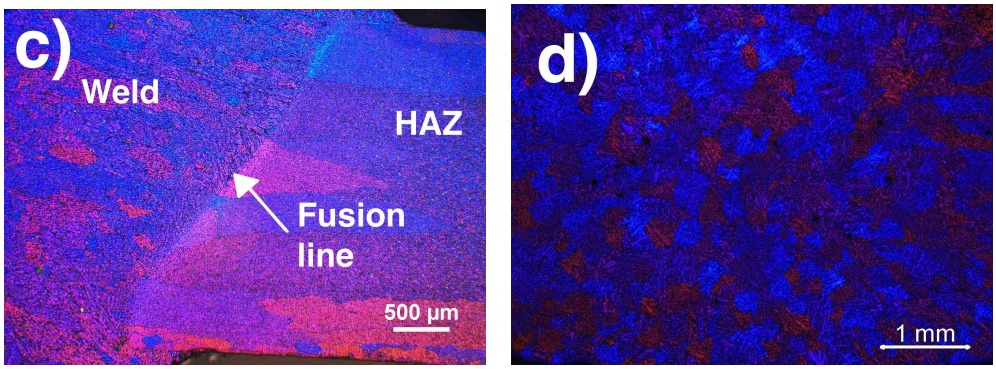

Figure 5.2: Micrographs of the as welded AA6082.52,T6 temper condition. All features of the as welded plate is shown in c), and the weld is shown in d).

The AA6082.50 alloy has another chemical composition than the AA6082.52 alloy, as seen in Table 2.1 in Section 2.2.1. The AA6082.50 has no Cr and less Cu and Mg than AA6082.52. Due to these differences, the recrystallized surface layer of the AA6082.50-T6 base material shown in the micrograph in Figure 5.3, a), is wider than the one of AA6082.52-T6. The depth of the recrystallized layer is about 125 μm. The Mn content is the same in both alloys, giving the same fibrous and uniform microstructure. To the right, b), the HAZ seen in the extrusion direction show a different situation than the corresponding micrograph above. The grain sizes have not grown large and has a more homogenous size distribution. The depth of the recrystallized layer is about 140 μm.

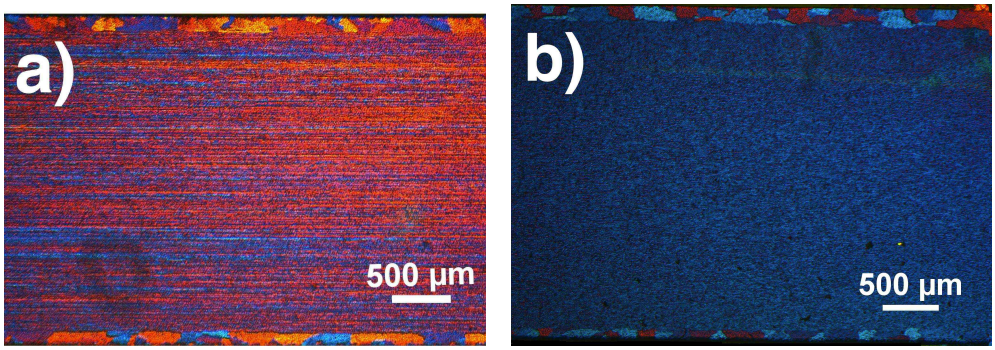

Figure 5.3: Micrographs of the AA6082.50, T6 temper condition. The base material to the left, a), and as welded to the right, b).

The welded AA6082.50-T6 profile, shown in Figure 5.4, differs from the welded AA6082.52-T6 profile by the almost non-existing HAZ. This is also validated by the hardness profiles, Figure 5.7 - 5.9. The fusion line separates the weld bead from the HAZ, pointed out by the arrow, in the micrograph to the left. The grain size near the surface in the HAZ show that some of the grains have grown due to the heat input, but the extent of this growth zone is limited. The depth of the recrystallized layer is about 200 μm. The grain size of the weld, d), is also here more uniform in size than in the HAZ and is the result of recrystallization and nucleation of the filler metal combined with the melted base material.

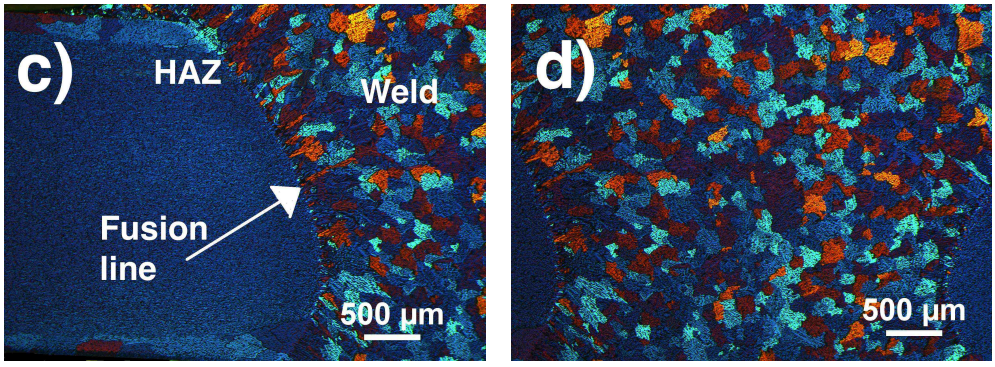

Figure 5.4: Micrographs of the welded AA6082.50,T6 temper condition. The micrograph to the left, c), shows all the features of the weld and the micrograph of the weld is to the right, d).

Some hot cracking can be seen at the weld toe in both Figure 5.2 c) and Figure 5.4 c), but it was not found any cold laps in either of the welded plates.

The microstructure of the PWHT specimen is shown in Figure 5.5. The depth of the recrystallized layer is between 125-140 μm. The microstructure does not differ much from the base material, Figure 5.3, and exhibit the same fibrous microstructure and somewhat the same depth of the

recrystallized layer.

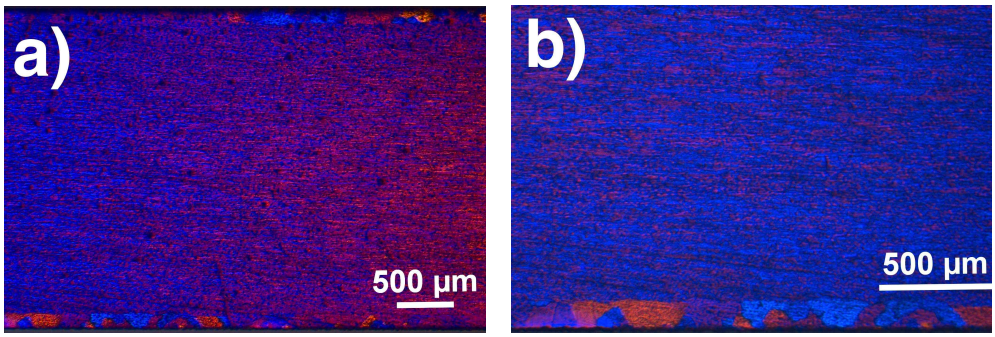

Figure 5.5: Micrographs of the post weld heat treated AA6082.50, T6 temper condition. The micrograph to the left, a), show the longitudinal transverse cross section and the recrystallized layer is shown in the micrograph to the right, b).

Figure 5.6 show the microstructure of the shot peened specimen of AA6082.50-T6. The result of the shot peening can be seen along the surface, in the micrograph to the right (b), hence the increased surface roughness. Part from these differences, the microstructure resembles the base material in Figure 5.3. The depth of the recrystallized layer is about 125 μm.

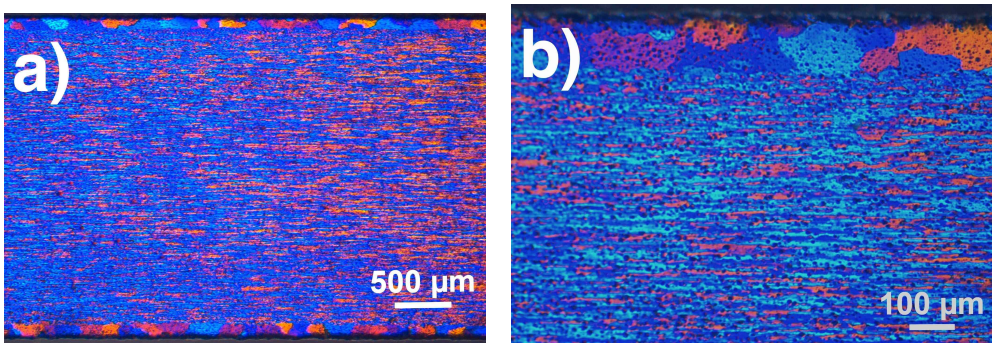

Figure 5.6: Micrographs of the shot peened AA6082.50, T6 temper condition. The micrograph to the left, a), show the longitudinal transverse cross section and the increased surface roughness can be seen in the micrograph to the right, b).

5.2 Hardness

The hardness profile in Figure 5.7 shows the extent of the HAZ in the welded AA6082.52-T6 profile. The grey area represents the weld bead and the dashed line is the average of five measurements of the hardness of the base material, giving the value of 109 HV. To ensure the HAZ

extends throughout the welded plates, three measurements were done at the ends of the plates. The profile to the right has the same scale as the hardness profiles of AA6082.50-T6 below, Figure 5.8 and Figure 5.9. In the weld, the minimum hardness was found to be 46 HV located in the middle of the weld. The hardness reached a maximum at 4 mm from the centre, at 87 HV. The minimum hardness measured in the HAZ was 43 HV and the maximum was 50 HV.

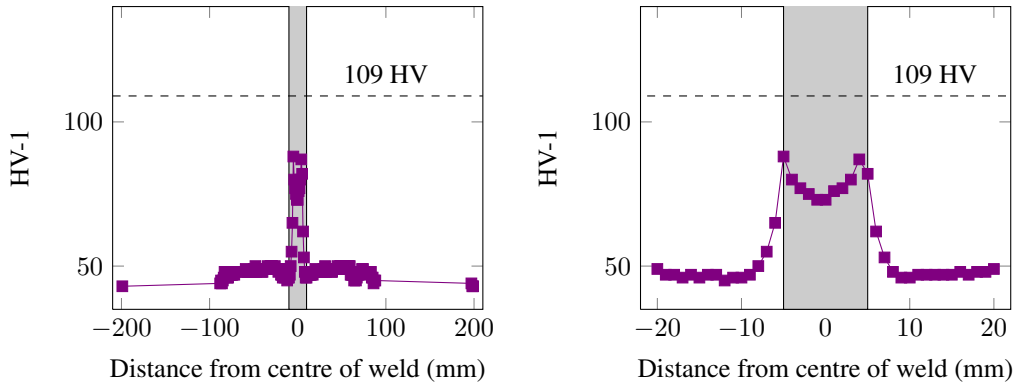

Figure 5.7: Hardness profile of the as welded AA6082.52, T6 temper condition. The gray area represents the weld bead and the dashed line is the measured hardness of the base material. The profile to the right is scaled the same as the following hardness profiles.

The hardness profile of the welded AA6082.50-T6, Figure 5.8, show a completely different profile than the one above. The HAZ is drastically reduced. This can be seen as the base material value (the dashed line) 94 HV, is reached 18 mm from the centre of the weld. This means that the HAZ only extends for 14 mm. The minimum value found in the weld bead was 58 HV and the maximum reached 75 HV. The minimum value found in the HAZ is the same as in the weld bead, 58 HV, measured 12 mm from the centre of the weld.

After the PWHT, the hardness of the profile is increased in the weld and the HAZ. The increase gives a new minimum value in the weld of 81 HV, an increase of 40 %. The maximum value in the weld bead has been increased with 50 %, 113 HV. The softest area in the HAZ is found to be 71 HV, an increase of 23 %. The hardness stabilizes after 15 mm from the centre of the weld, giving a decrease of the HAZ with 3 mm. The hardness reached outside the HAZ has decreased compared to the specimen before the heat treatment, having a maximum hardness of 85 HV.

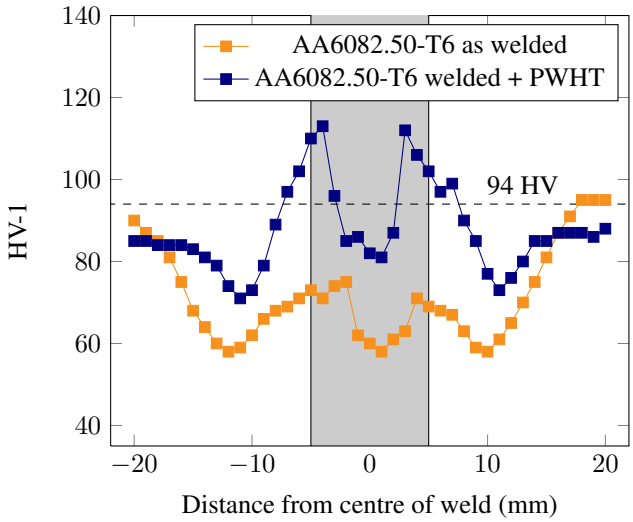

Figure 5.8: Hardness profiles of as welded AA6082.50, temper condition T6 before (orange) and after PWHT (blue). The gray area represents the weld bead and the dashed line is the measured hardness of the base material.

Figure 5.9 show the same reduced HAZ as Figure 5.8 of the as welded and PWHT specimens. The dashed line representing the base material value of 94 HV, was reached 19 mm from the centre of the weld. The minimum hardness measured in the weld bead was found to be 60 HV and the maximum hardness was 80 HV. In the HAZ the minimum value measured was 59 HV, 10 mm from the centre of the weld.

After being shot peened, the hardness of the specimen increased all over the welded profile, represented by the pink curve in Figure 5.9. A new minimum in the weld bead was found to be 89 HV and the maximum was found to be 110 HV. Both show an increase in hardness of about 30 HV. In the heat affected zone, the softest area measured was 73 MPa, 10 mm from the centre of the weld. Maximum hardness measured 18 mm from the centre of the weld was 103 HV. The softest area is still in the same region after the shot peening, but is now increased by at least 14 HV.

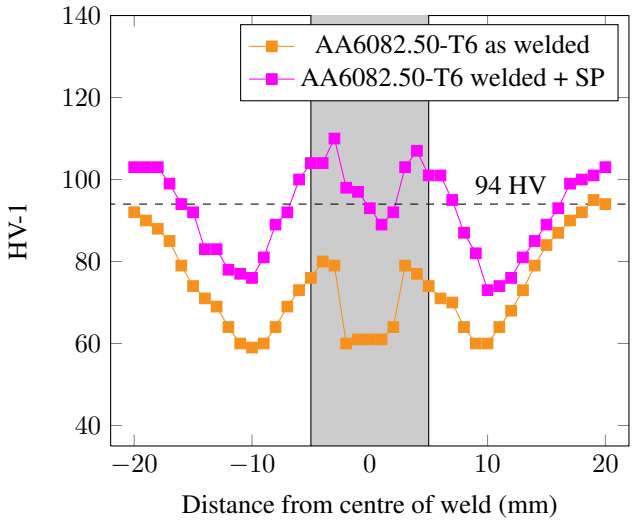

Figure 5.9: Hardness profiles of as welded AA6082.50, temper condition T6 before being shot peened (orange) and after (pink). The gray area represents the weld bead and the dashed line is the hardness measured of the base material.

5.3 Surface roughness

The surface roughness of the different specimens was measured using a Mahr Perthometer M2, using the auto function to measure the average roughness of the surface, R_a, the maximum height of the profile, R_t, and the average distance between the highest peak and lowest valley, R_z. The length measured is given as L_t. All parameters are given as the average of three measurements in Table 5.1.

Table 5.1: Surface roughness of the different specimens of AA6082.52 and AA6082.50, both in T6 temper condition.

Alloy	Specimen	L_t [mm]	R_a [μm]	R_z [μm]	R_t [μm]
AA6082.52	Base material	5.60	0.422	2.82	5.43
	As welded	5.60	0.824	5.00	10.4
AA6082.50	Base material	17.5	2.14	13.8	19.7
	As welded	17.5	3.24	16.8	37.5
	Welded + PWHT	17.5	1.894	5.47	30.1
	Welded before SP	17.5	3.672	15.4	22.8
	Welded + SP	17.5	5.742	37.3	56.0

The surface profiles of the specimens are given in Figures 5.10 - 5.15. The profiles show the peaks and valleys of the specimens as positive and negative, respectively. The different measured

lengths were chosen by the auto function of the perthometer. (The grids shown are not in scale).

The base material of AA6082.52-T6 in Figure 5.10, was measured over 5.60 mm of one of the specimens. The roughness of the surface show a maximum difference between the highest peak and the lowest valley to be 2.82 μm and the highest peak to be 5.43 μm. The highest peak and lowest valley are shown with arrows. The profile show a somewhat even surface given the R_a value of 0.422 μm.

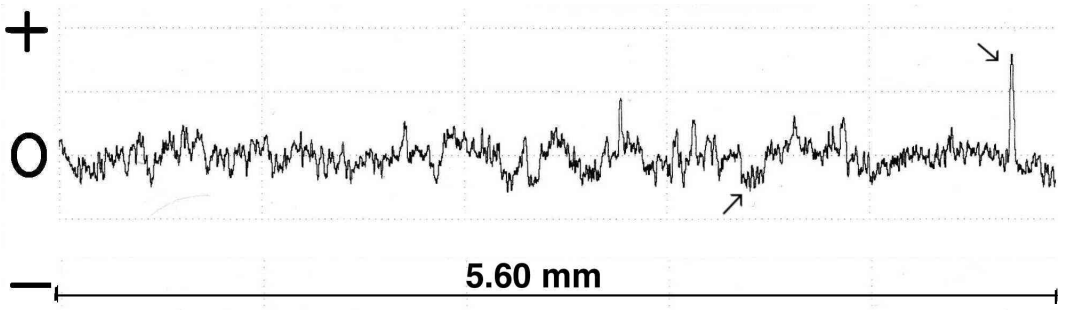

Figure 5.10: Surface profile of AA6082.52-T6 base material.

The as welded specimen of AA6082.52-T6 in Figure 5.11, was measured over a length of 5.60 mm. The roughness of the surface show a maximum difference between the highest peak and the lowest valley to be 5.00 μm. The highest peak was found to be 10.4 μm. The highest peak and lowest valley are shown with arrows. The profile show a more rough surface than the base material given a R_a value of 0.824 μm. The surface profile show that the as welded specimens have a different surface finish than the extruded base material.

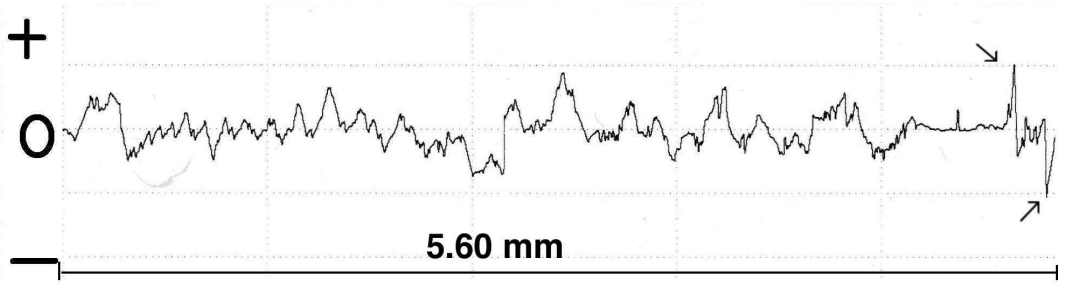

Figure 5.11: Surface profile of AA6082.52-T6 as welded.

The base material specimen of AA6082.50-T6 in Figure 5.12, was measured over a length of 17.5 mm. The surface is similar to the AA6082.52-T6 base material. As the measured length is longer, it gives a more compact profile. The maximum difference between the highest peak and the lowest valley was found to be 13.8 μm. The highest peak and lowest valley are shown with arrows, where the highest peak is 19.7 μm. The R_a value of 2.14 μm, gives a more rough surface than the previous profiles.

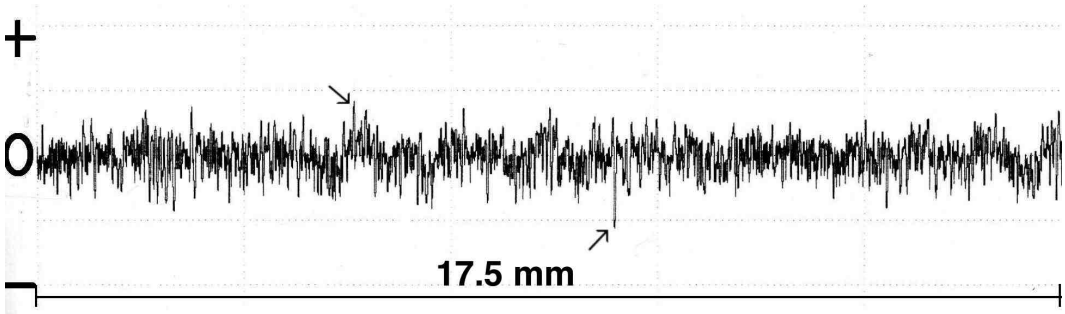

Figure 5.12: Surface profile of AA6082.50-T6 base material.

The as welded specimen of AA6082.50-T6 in Figure 5.13, was measured over a length of 17.5 mm. The roughness of the surface show a maximum difference between the highest peak and the lowest valley to be 16.8 μm, a higher difference than the base material. The highest peak is also higher than for the base material with a value of 37.5 μm. The highest peak and lowest valley are shown with arrows. The profile show a more rough surface than the base material given a R_a value of 3.24 μm. Surface profile show that the welded specimens have a different surface finish than the extruded base material.

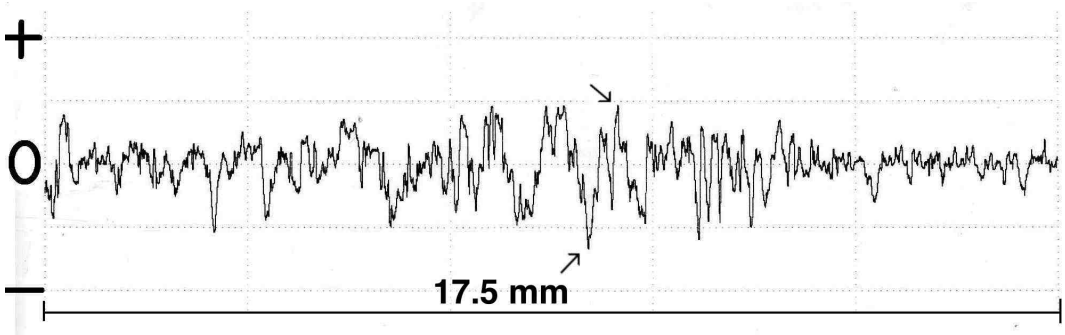

Figure 5.13: Surface profile of AA6082.50-T6 as welded.

The post weld heat treated specimen of AA6082.50-T6 in Figure 5.14, was measured over a length of 17.5 mm. The roughness of the surface show a maximum difference between the highest peak and the lowest valley to be 5.47 μm. The highest peak in this surface profile was found to be 30.1 μm. The highest peak and lowest valley are shown with arrows. The profile show a less rough surface than the base material and the as welded specimen, given a R_a value of 1.894 μm. This specimen have another surface finish than the two previous specimens, and contain larger notches.

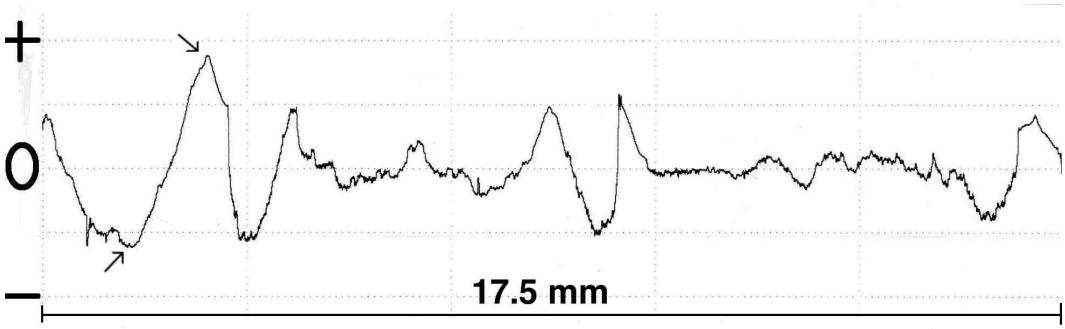

Figure 5.14: Surface profile of AA6082.50-T6 welded + PWHT.

The as welded specimen to be shot peened of AA6082.52-T6 in Figure 5.15, was also measured over a length of 17.5 mm. The roughness of the surface show a maximum difference between the highest peak and the lowest valley to be 15.4 μm and the highest peak 22.8 μm. The highest peak and lowest valley are shown with arrows. The R_a value of 3.672 μm, show that this specimen has the largest roughness difference. The surface differs from the base material by being smoother at some areas and having larger notches.

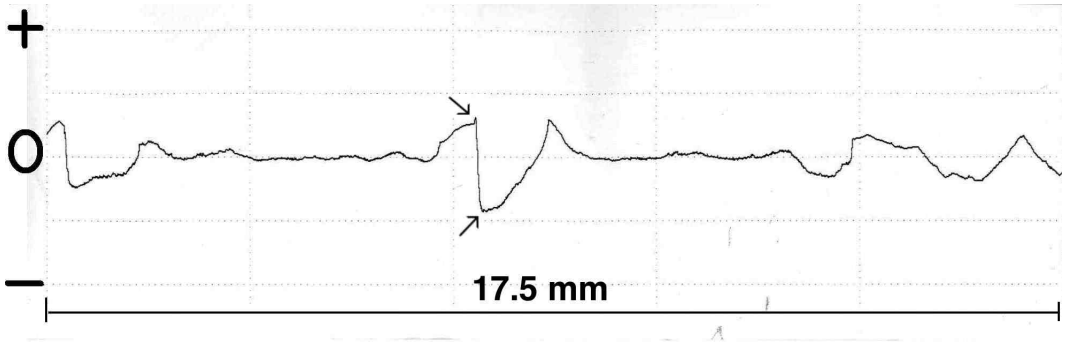

Figure 5.15: Surface profile of AA6082.50-T6 welded before SP.

After being shot peened, the as welded AA6082.50-T6 specimen surface resulted in the surface profile shown in Figure 5.16. The length measured over the welded area was 17.5 mm and the average roughness, R_a, has increased to 5.742 μm. The maximum difference between the highest peak and the lowest valley, R_z, is now 37.3 μm with the highest peak at 56.0 μm on average. The roughness seen from the surface profile differs from the before surface treatment by being more rough throughout the surface and not having one large notch that is easily distinguished from the rest as in Figure 5.15. Micrographs of the surface of a shot peened specimen are shown in Figure B.3 in Appendix B.

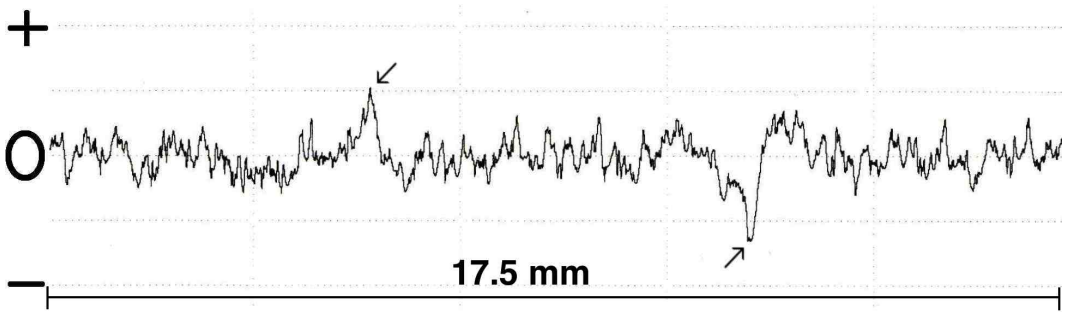

Figure 5.16: Surface profile of AA6082.50-T6 welded + SP.

5.4 Tensile tests

Tensile tests were done to find the yield strength and the ultimate tensile strengths of the different specimens. Two additional tests were done on the AA6082.50-T6 alloy to document any cyclic hardening or softening after about $3.0x10^6$ cycles without fracture and for the specimens deemed run-out (10^7 cycles without fracture). The tensile tests all had fracture in the same manner, through the 45° shear plane. The fractures happened in the smallest cross section area, except for the as welded AA6082.52-T6 that fractured in the HAZ.

Tensile tests of the base material and the as welded AA6082.52 in the T6 temper condition, Figure 5.17, show a drastic reduction of strength in the as welded specimen. With a yield strength of 325 MPa of the base material, a reduction of about 71 % is observed after welded, 95 MPa. The ultimate tensile strength is reduced with almost 50 %. The ductility however is increased after welding. The yield strength and ultimate tensile strengths are given in Table 5.2.

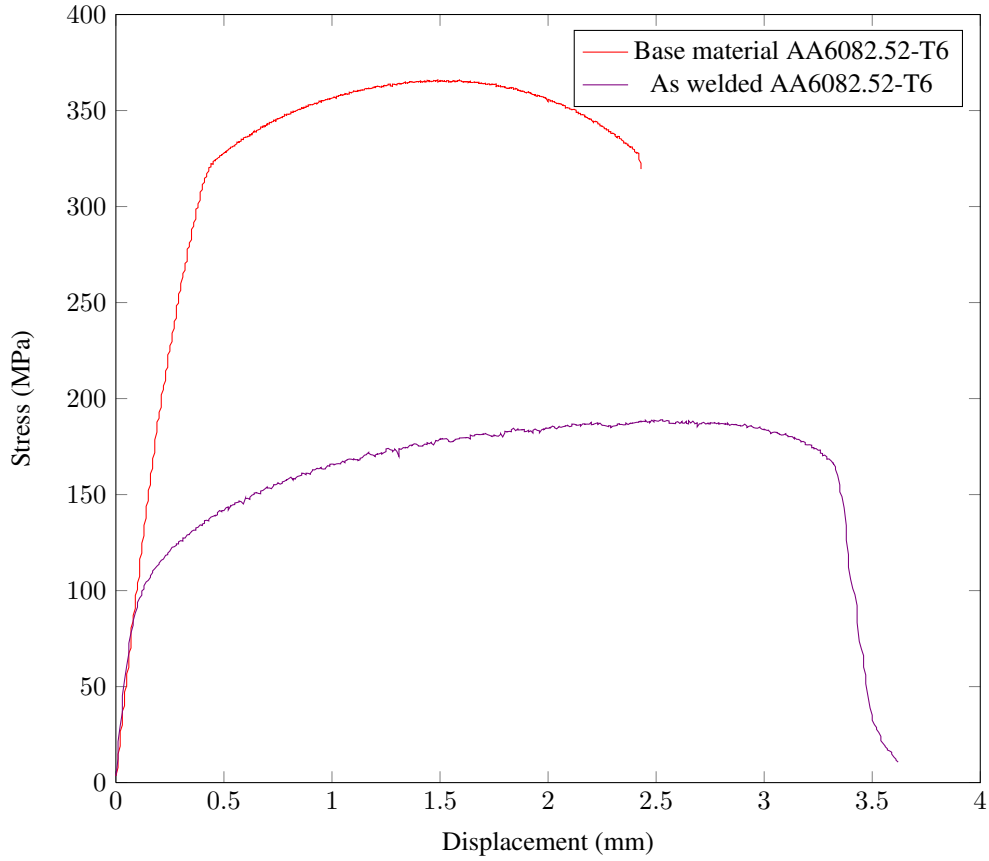

Figure 5.17: Tensile tests for base material and as welded AA6082.52-T6.

The tensile test of the base material of AA6082.50-T6, Figure 5.18, give a yield strength of 245 MPa and an ultimate tensile strength of 306 MPa. Compared to the AA6082.52-T6 the strengths of the material are lower, due to the differences in the chemical compositions. The ductility is almost the same. Compared to the specimen being cycled for $3.0x10^6$ cycles at maximum stress of 120 MPa without fracture, the yield strength increased to 260 MPa and the ultimate tensile strength to 311 MPa. The deemed run-out (RO) at maximum applied stress at 120 MPa does not show any significant increase in strength. The yield strength and ultimate tensile strength are found to be 245 MPa and 309 MPa, respectively.

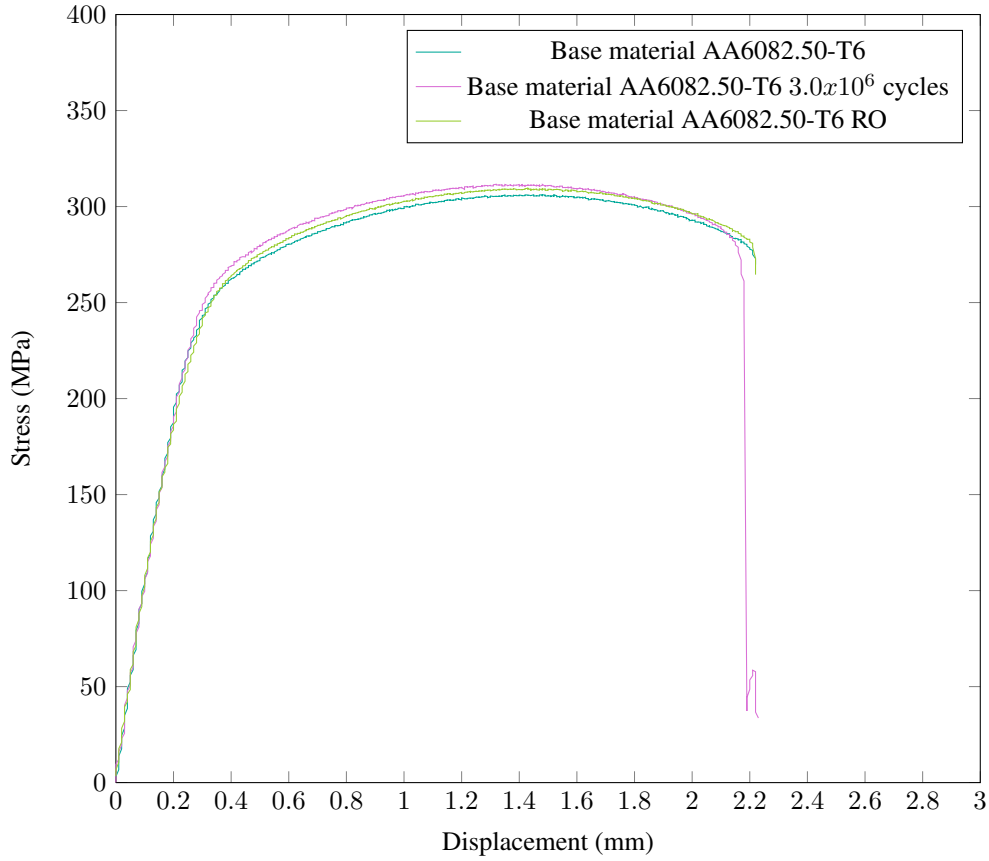

Figure 5.18: Tensile tests of the base material AA6082.50-T6. The dark green curve is the un-cycled specimen, the pink curve has been cycled for $3.0x10^6$ cycles and the light green is the specimen deemed run-out.

The as welded specimen of AA6082.50-T6 is shown in orange in Figure 5.19. A reduction in strength compared to the base material is observed. The yield strength is reduced by 41 %, from 245 MPa to 145 MPa. The ultimate tensile strength is reduced with only 23 % to 236 MPa. A much less reduction than for the AA6082.52-T6.

Comparing a specimen of the as welded that were deemed run-out (RO) with one that has not been cycled, a cyclic hardening is observed. The cycled specimen, tested at maximum stress of 90 MPa, has increased strength by 3 % in yield strength and 5 % in ultimate tensile strength, from 145 MPa to 150 MPa and from 236 MPa to 247 MPa respectively. The cycled specimen also has reduced ductility due to the hardening.

The pink curve represents a specimen aborted after $3.0x10^6$ cycles at maximum stress of 130 MPa. The specimen also shows cyclic hardening compared to the specimen that has not undergone any cycles. The yield strength increased from 145 MPa to 160 MPa, an increase of 9 %.

The ultimate tensile strength has increased with 3 %, from 236 MPa to 243 MPa. The ductility however has had a large decrease. Compared to the RO specimen, the yield strength is 6 % higher and the ultimate tensile strength is 1.5 % lower.

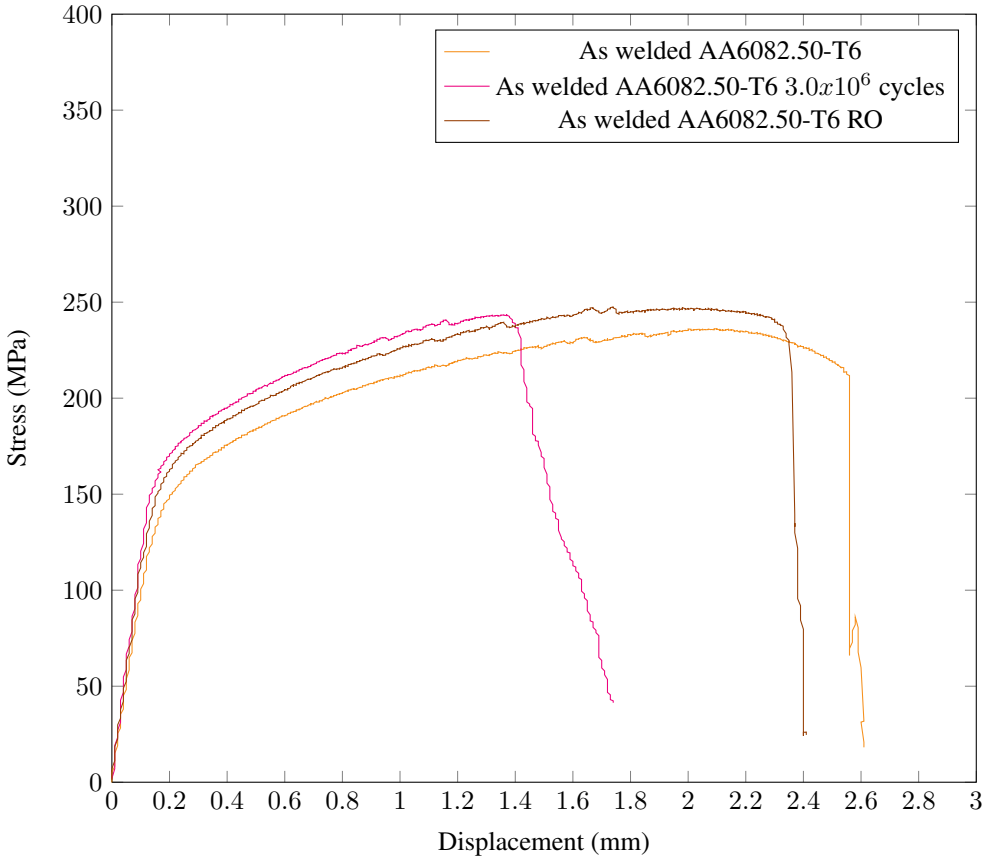

Figure 5.19: Tensile tests of as welded AA6082.50-T6. Orange curve represents the specimens that had not undergone any cycles, the brown curve represents the specimen undergone 10^7 cycles and the pink curve represents a specimen that was aborted after $3x10^6$ cycles.

The PWHT specimen of AA6082.50-T6 is shown in blue in Figure 5.20. The curve gives a yield strength of 200 MPa and an ultimate tensile strength of 251 MPa. The ductility in the specimen is drastically reduced compared to the base material and the as welded specimens. A 18 % reduction in yield strength and ultimate tensile strength compared to the base material is observed. The reduction of yield strength and ultimate tensile strength from the un-cycled to the specimen undergone $3.6x10^6$ cycles at maximum applied stress of 125 MPa, are 18 % and 12 %, respectively. Showing an opposite behavior compared to the other tensile curves. The deemed run-out specimen cycled at maximum 100 MPa however, show almost no difference in yield strength and ultimate tensile strength compared to the un-cycled specimen.

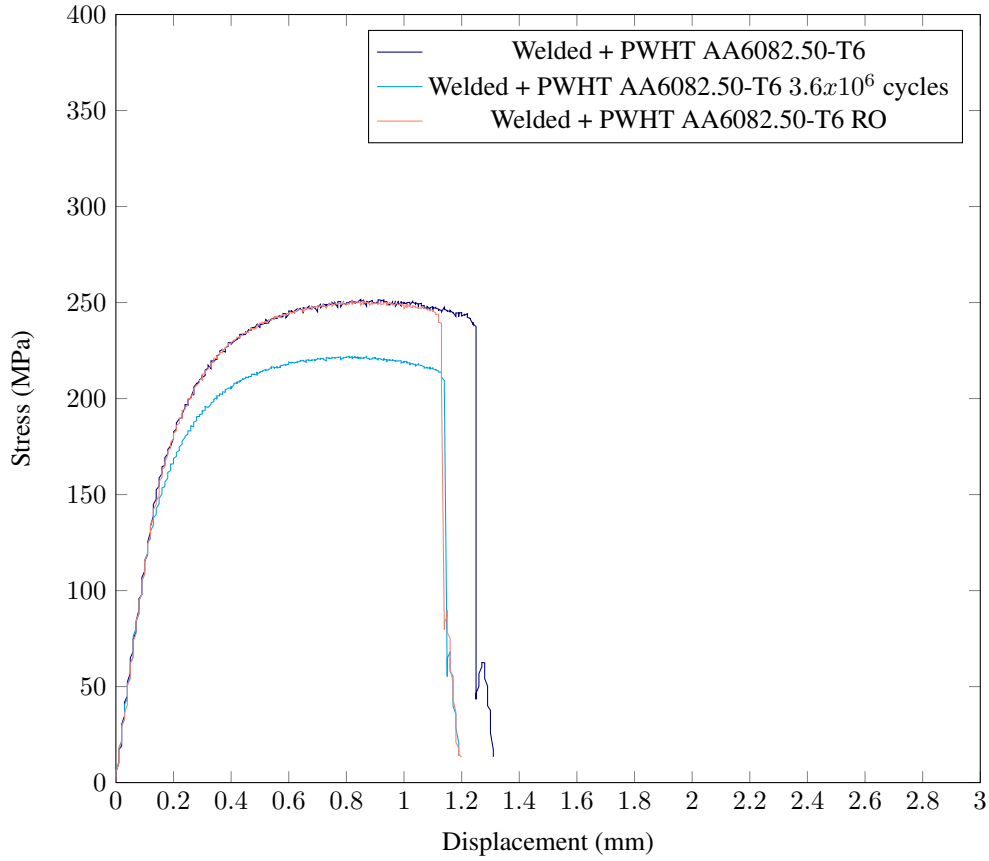

Figure 5.20: Tensile tests of the post weld heat treated specimens of AA6082.50-T6. The purple curve is the un-cycled specimen, the light blue curve is of a specimen undergone $3.6x10^6$ cycles and the orange curve is the specimen deemed run-out.

The shot peened specimen in figure 5.21 show a yield strength of 160 MPa and an ultimate tensile strength of 245 MPa. After 10^7 cycles at 130 MPa, there is not observed any cyclic hardening or softening. The yield strength has decreased with 6 % to 150 MPa and the ultimate tensile strength is found to be 238 MPa, a decrease of 3 %. The ductility seems intact. After $2.8x10^6$ cycles at maximum 130 MPa, the specimen has the same yield strength and ultimate tensile strength as the un-cycled specimen, 160 MPa and 245 MPa respectively. The ductility has only been a bit reduced.

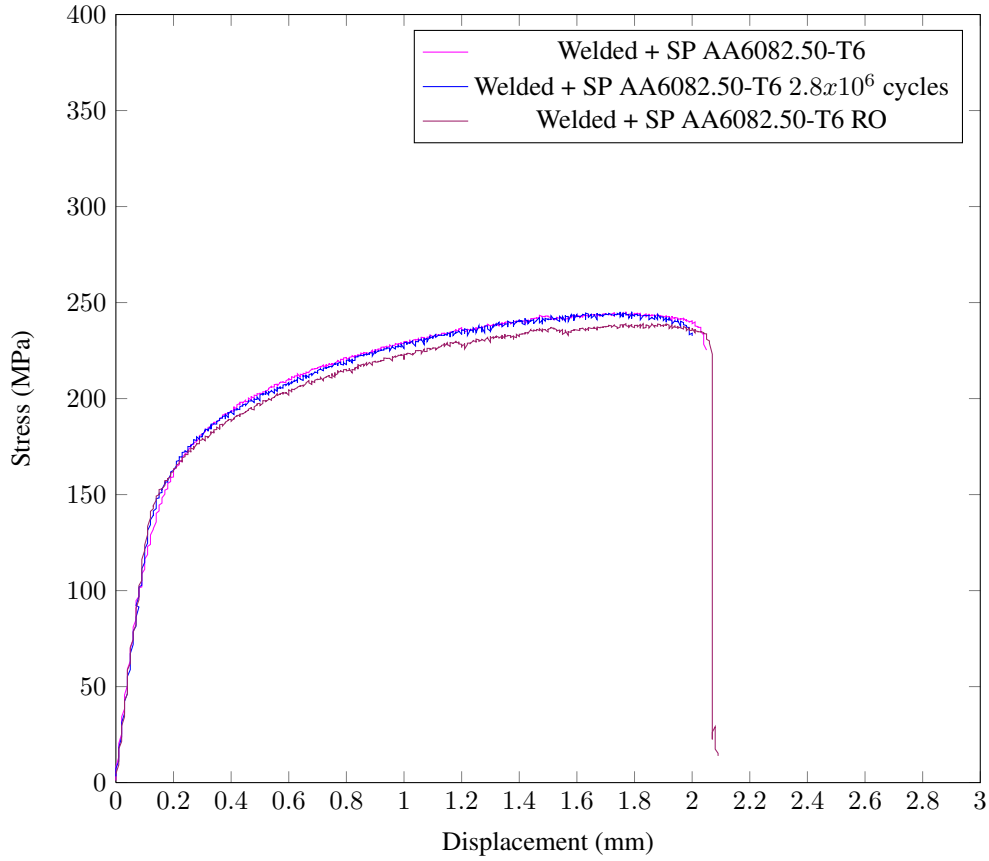

Figure 5.21: Tensile tests of the shot peened specimens of AA6082.50-T6. The pink curve represents the specimen not undergone any cycles, the blue curve is of the specimen undergone $2.8x10^6$ cycles and the brown curve is the specimen deemed run-out.

The yield strength and ultimate tensile strength given in Table 5.2, are derived from the tensile curves above, Figure 5.17 - Figure 5.21.

Table 5.2: Yield strength and ultimate tensile strength of the different specimens of AA6082.52 and AA6082.50. Both in the T6 temper condition.

Alloy	Specimen	Yield strength [MPa]	Ultimate tensile strength [MPa]
AA6082.52	Base material	325	365
	As welded	95	188
AA6082.50	Base material	245	306
	Base material $3.0x10^6$ cycles	260	311
	Base material RO	245	309
	As welded	145	236
	As welded RO	150	247
	As welded $3.0x10^6$ cycles	160	243
	Welded + PWHT	200	251
	Welded + PWHT $3.6x10^6$ cycles	165	221
	Welded + PWHT RO	200	250
	Welded + Shot Peening	160	245
	Welded + Shot Peening $2.8x10^6$ cycles	160	245
	Welded + Shot Peening RO	150	238

All of the tensile tests of the four different specimens are given in Figure 5.22. None of the specimens have been cycled. Comparing the tensile curves of the different specimens show that the base material has the highest yield strength and ultimate tensile strength. The as welded specimen is the most ductile specimen. The as welded specimen has a reduction of yield strength and ultimate tensile strength of 40 % and 20 % respectively. When post weld heat treating the as welded specimen, the ductility is drastically reduced, almost by 50 %. The yield strength and ultimate tensile strength however is increased with about 40 % and 6 %, respectively. By shot peening the as welded specimen an increase in yield strength by 10 % is observed. The ultimate tensile strength is increased by only 4 %. The ductility of the specimen is not as reduced as the PWHT specimen.

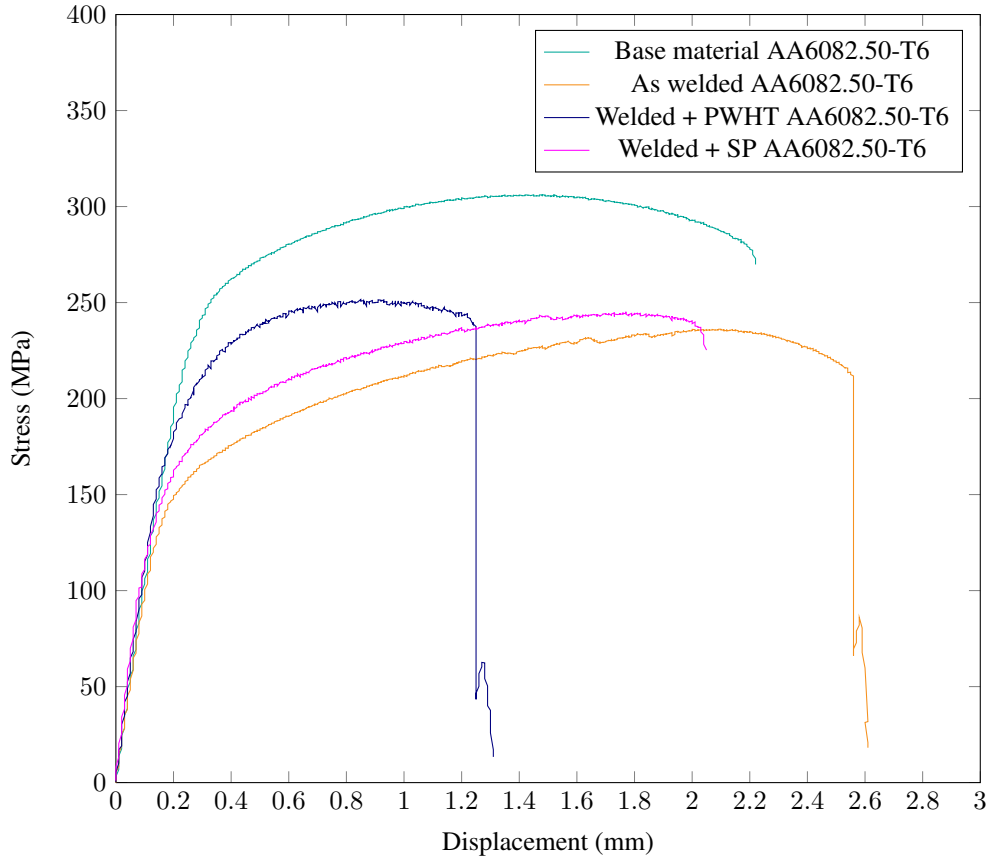

Figure 5.22: All the tensile tests of the different specimens of AA6082.50-T6. The green is the base material, the orange is the as welded, the PWHT is blue and the shot peened specimen is represented by the pink curve.

5.5 Fatigue testing

The S-N curves shown in Figure 5.23 are a continuation of the specialization project done fall of 2012. During this project fatigue testings of the base material, the weld and the HAZ of the T1 tempered profile were done. The addition of T6 tempered specimens were done to complete the S-N curves of AA6082.52. The T6 tempered base material show a more steeper curve with no run-outs. The as welded curve show a correspondent curve to the T1 tempered specimens, exhibiting a higher fatigue resistance. The fatigue lives at $N = 10^6$ is shown in table 5.3. The as welded T6 specimens, regardless of the loss of strength due to welding, display a better fatigue resistance than all of the welded T1 tempered specimens.

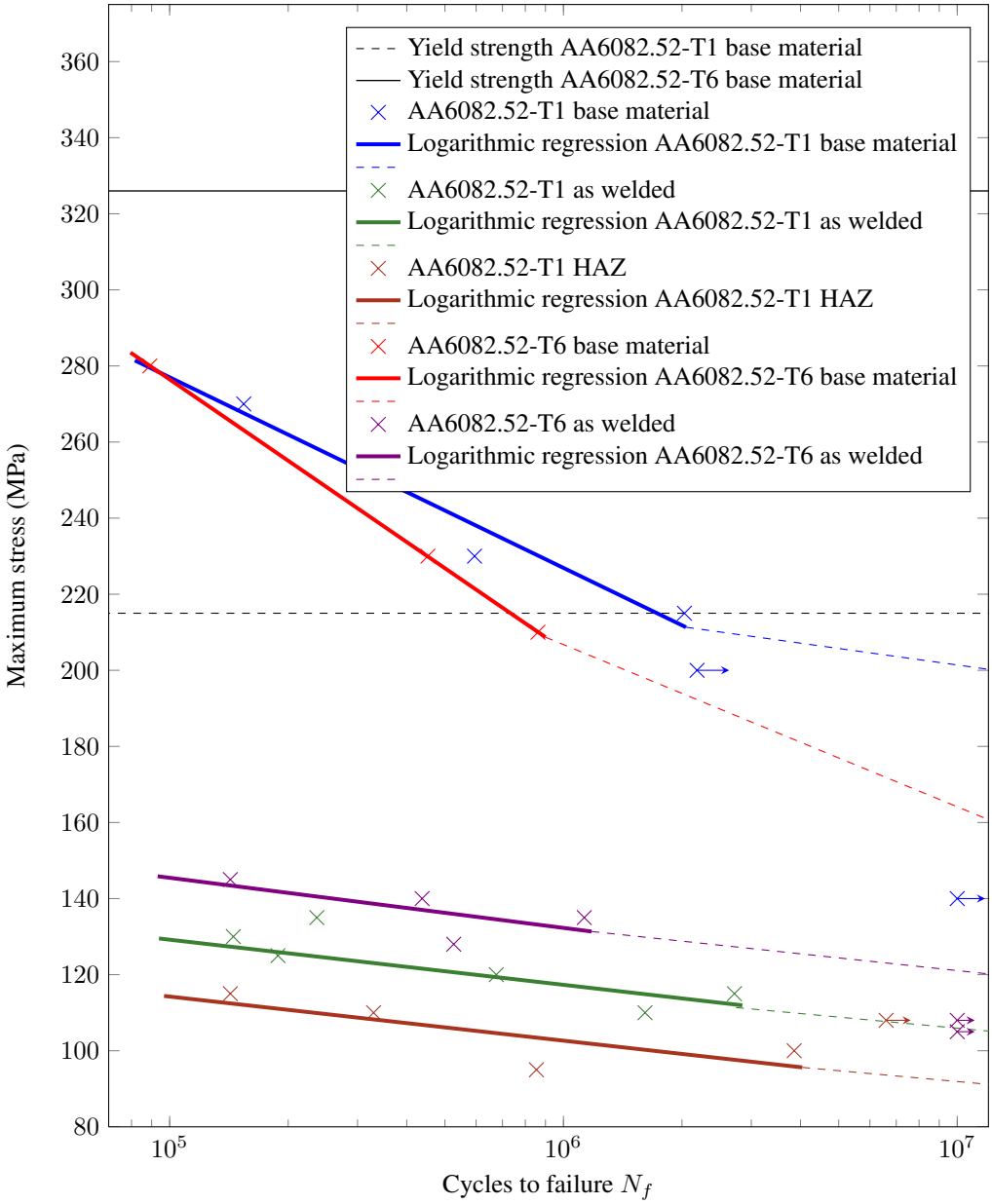

Figure 5.23: S-N curve of base material and as welded AA6082.52, temper condition T1 and T6. Arrows indicates specimens that were deemed run-outs (RO). The black line is the yield strength of the base material and the dashed line of the as welded specimens of AA6082.52-T6.

Table 5.3 show that the fatigue life of a welded specimen in the T1 temper condition is reduced by almost 50 % at $N = 10^6$ cycles. For the HAZ specimens the fatigue life is even further reduced,

over 50 %. In the T6 temper condition, the as welded specimens had a 35 % reduction after $N = 10^6$ cycles.

Table 5.3: Fatigue life at $N = 10^6$ of AA6082.52.

Temper condition	Specimen	Fatigue life [MPa]
T1	Base material	230
	As welded	120
	HAZ	108
T6	Base material	210
	As welded	135

The S-N curves in Figure 5.24 are of the various specimens of AA6082.50 in the T6 temper condition. The reduction of fatigue resistance of the as welded specimen is reduced by about 40 %. There is not found any large scatter between the data in this curve. By PWHT the as welded specimens, an increase in fatigue resistance is observed. The fatigue life is increased by 26 %. Compared to the base material the fatigue resistance is reduced by 30 %. There are more scatter in the data for this curve and the curve is less steep than for the as welded curve. The shot peened curve has an even more increased fatigue resistance than the PWHT, by 38 % compared to the as welded. The shot peened specimen show a decrease in fatigue life at N = 10^6 by 21 % compared to the base material. However, the endurance limit, 130 MPa, of the specimens are higher than for the base material, 120 MPa.

The yield strengths are shown as the black lines. The base material at 245 MPa, the PWHT at 200 MPa, the shot peened specimen at 160 MPa and the as welded at 145 MPa.

The tests were all done between 22 - 28 °C and the humidity varied between 10 - 40 %.

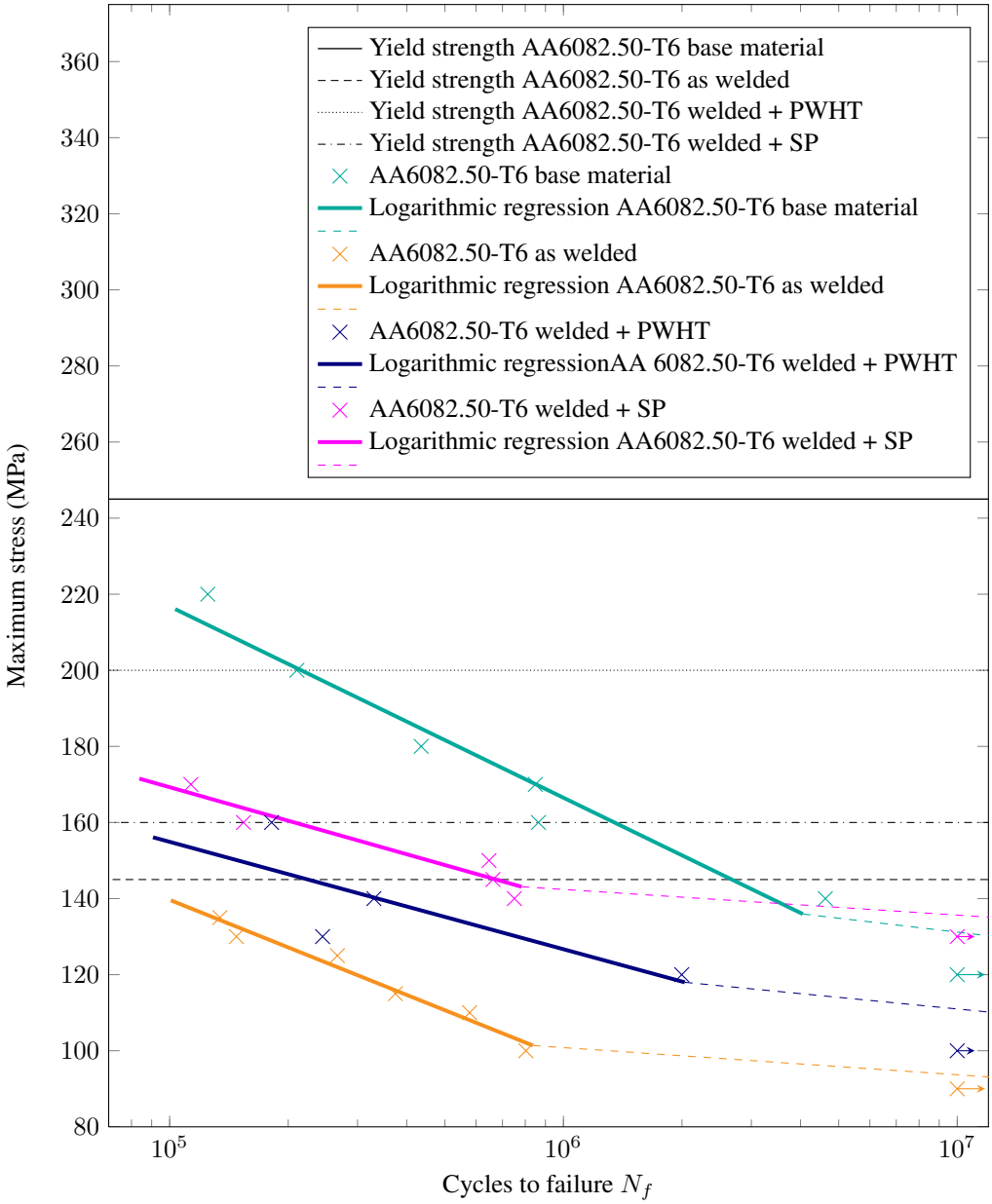

Figure 5.24: S-N curve of base material, as welded and post weld treated AA6082.50, temper conditionT6. Arrows indicates specimens that were deemed run-outs (RO). The different yield strengths are given by the black lines.

In Table 5.4 the fatigue lives of all of the AA6082.50-T6 specimens after $N = 10^6$ are listed.

Table 5.4: Fatigue life at $N = 10^6$ of AA6082.50-T6.

Specimen	Fatigue life [MPa]
Base material	175
As welded	100
Welded + PWHT	126
Welded + SP	138

All the fatigue data are given in Table C.1 in Appendix C.

5.6 Goodman diagrams

The Goodman diagrams are based on the fatigue and tensile data given above for each type of specimen. For the AA6082.52-T6 base material specimens, Figure 5.25, the Goodman line (red) is drawn from the endurance limit, 160 MPa, taken from the S-N curve, Figure 5.24. The line is drawn to the ultimate tensile strength, 365 MPa, from the tensile test, on the x-axis. The brown line is the yield strength, 325 MPa, found from the same tensile test, giving the limiting mean stress line. The area below these two lines represents the estimation of safe operational region for fatigue, based on applied stress amplitude (y-axis) and mean stress (x-axis). The stress ratios, R = 0, 0.1 and 0.5 are also given in all of the diagrams.

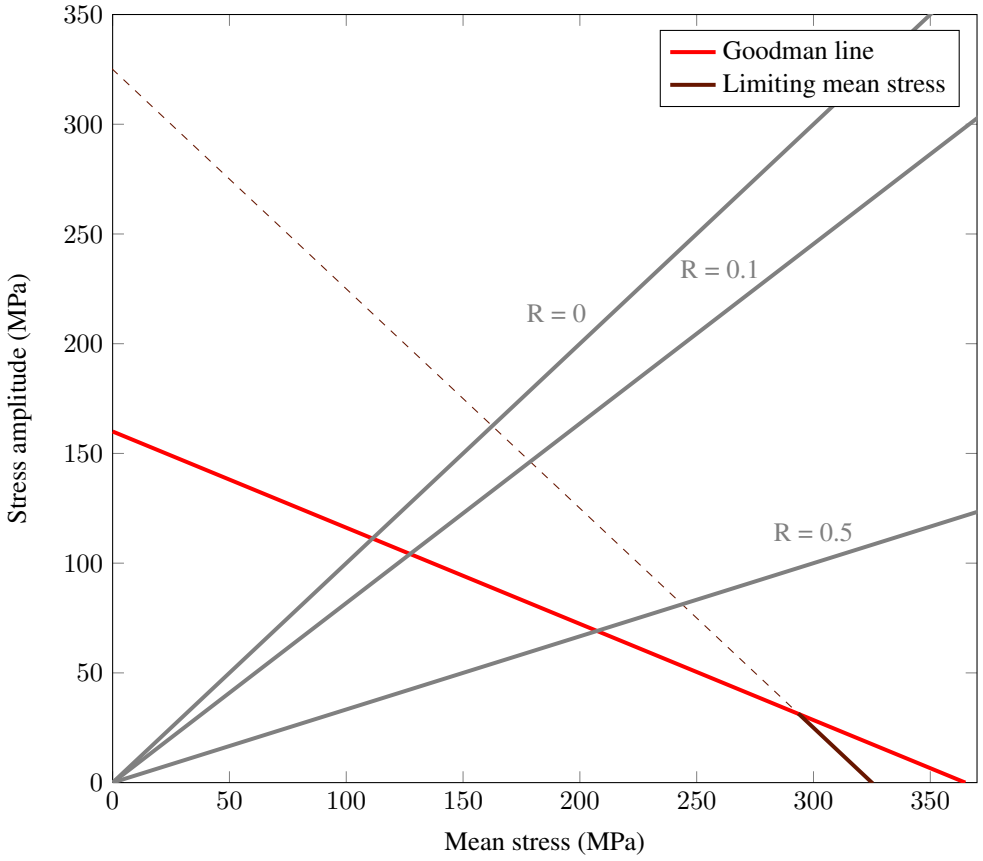

Figure 5.25: Goodman diagram for the base material of AA6082.52-T6.

The as welded specimen of AA6082.52-T6, Figure 5.26, show the limiting mean stress line (beige) being below the Goodman line (purple). The yield strength of 95 MPa is the limiting value by this estimation, while the endurance limit exceeds this value by 13 MPa up to 108 MPa. The ultimate tensile strength here is 188 MPa. The area between these two curves represents the yielding area during fatigue, suggesting yielding at all applied mean stresses and stress amplitudes above yield strength.

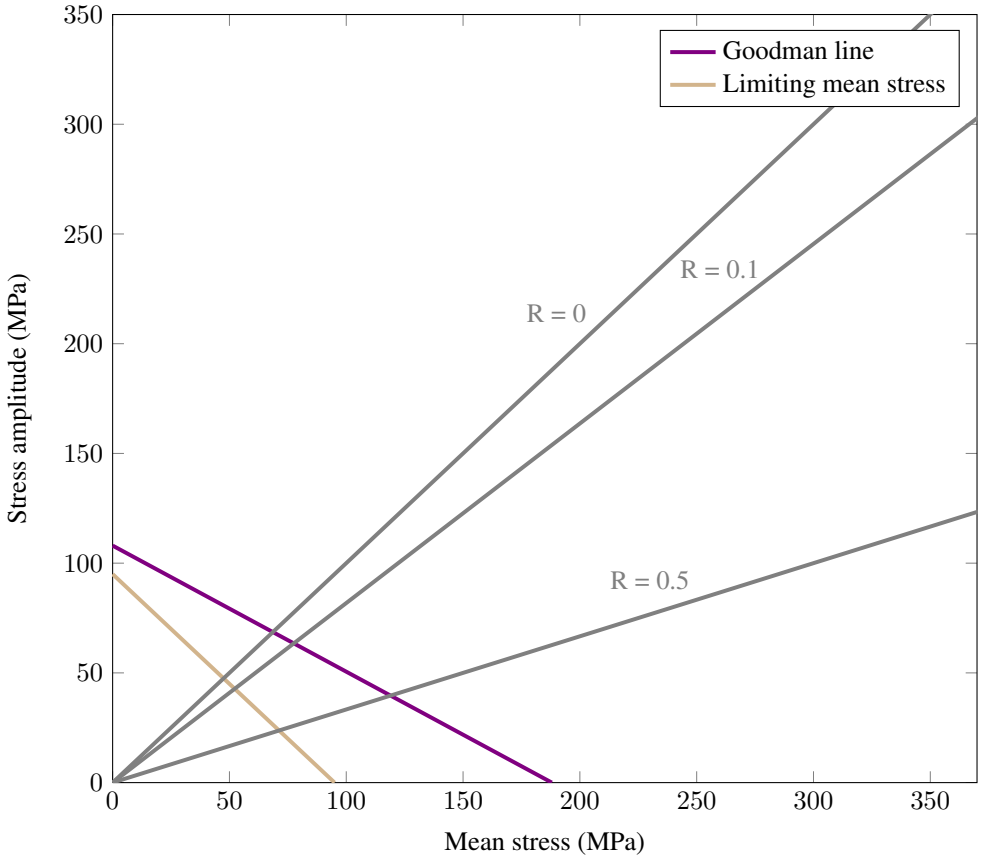

Figure 5.26: Goodman diagram for as welded AA6082.52-T6.

The base material for AA6082.50-T6 is shown in Figure 5.27. The dark green line is the Goodman line drawn from the endurance limit, 120 MPa, taken from the specimen being deemed run-out during fatigue testing, to the ultimate tensile strength, 306 MPa, on the x-axis. The light green line is the limiting mean stress line, with a yield strength of 245 MPa.

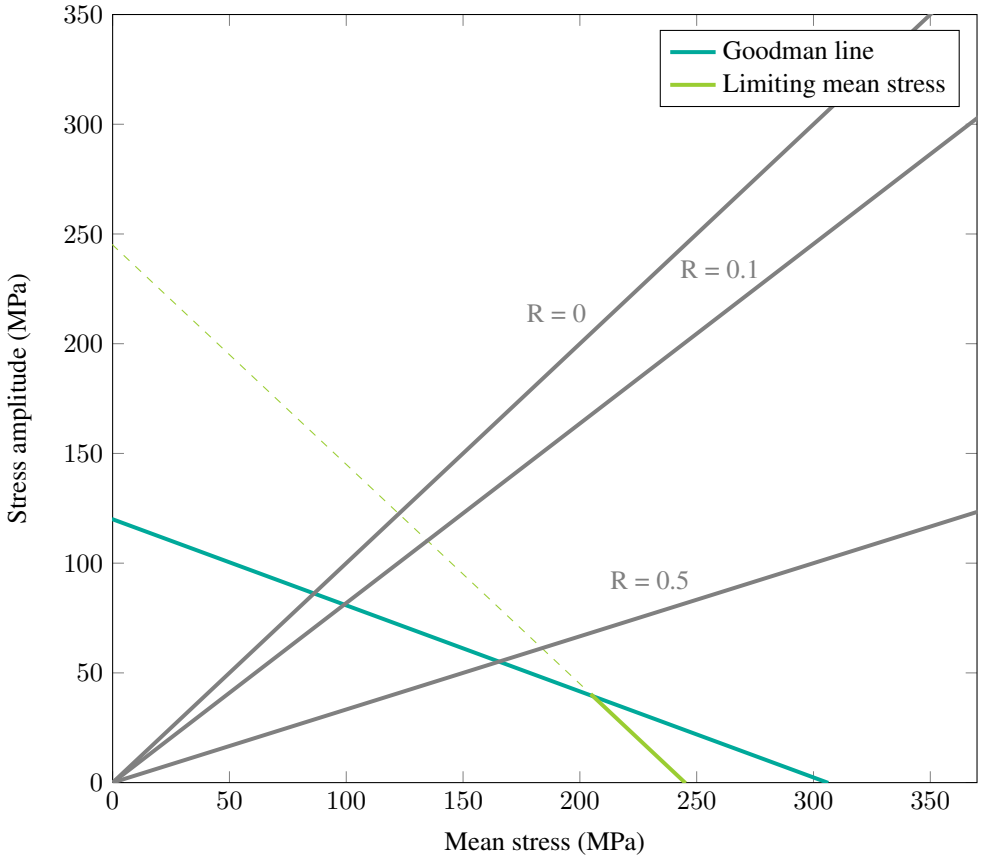

Figure 5.27: Goodman diagram for the base material of AA6082.50-T6.

Figure 5.28 shows the Goodman diagram for the as welded specimens of AA6082-T6. This estimation show a smaller area of safe operation, as the S-N curve also indicates. The endurance limit is here put to 90 MPa, the ultimate tensile strength used is 236 MPa and the yield strength is 145 MPa.

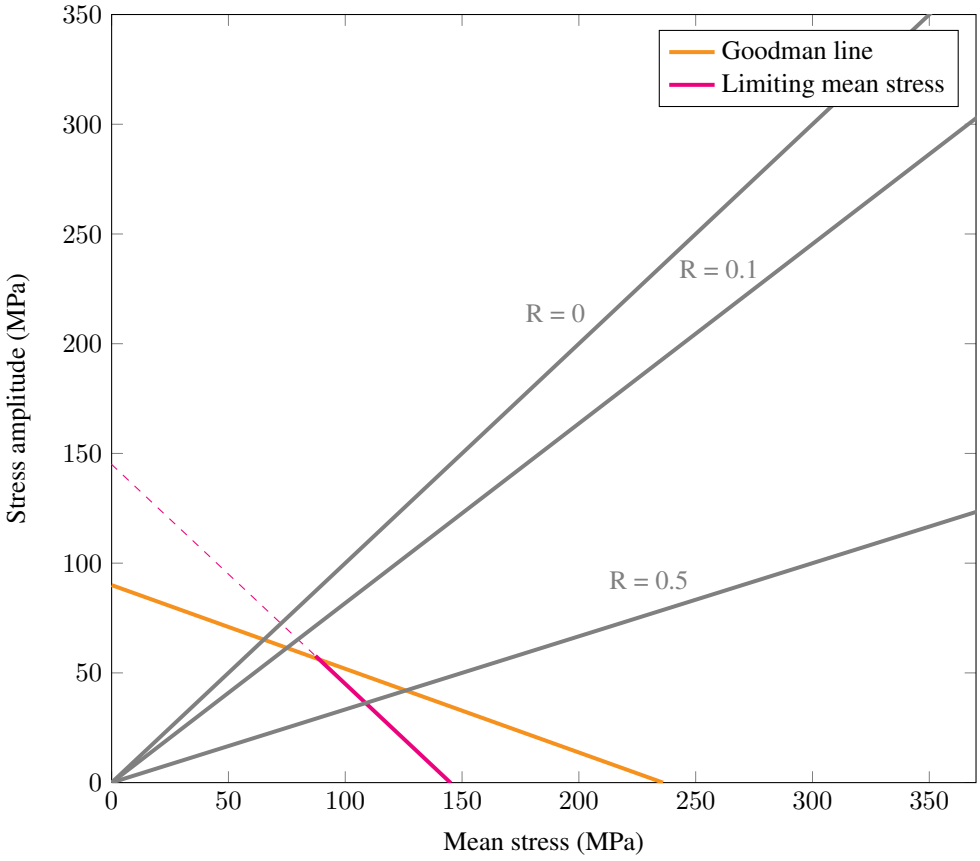

Figure 5.28: Goodman diagram for as welded AA6082.50-T6.

The Goodman diagram for the PWHT specimens, Figure 5.29, illustrates the same results as the S-N curve, Figure 5.24. The PWHT specimens have a better fatigue resistance than the as welded specimens. The area under the two curves is larger, hence having a larger safe operational region. The endurance limit is set to 110 MPa and together with the ultimate tensile strength, 243 MPa, the Goodman line is drawn. The limiting mean stress is drawn from the yield strength of 175 MPa from the x-axis to the y-axis.

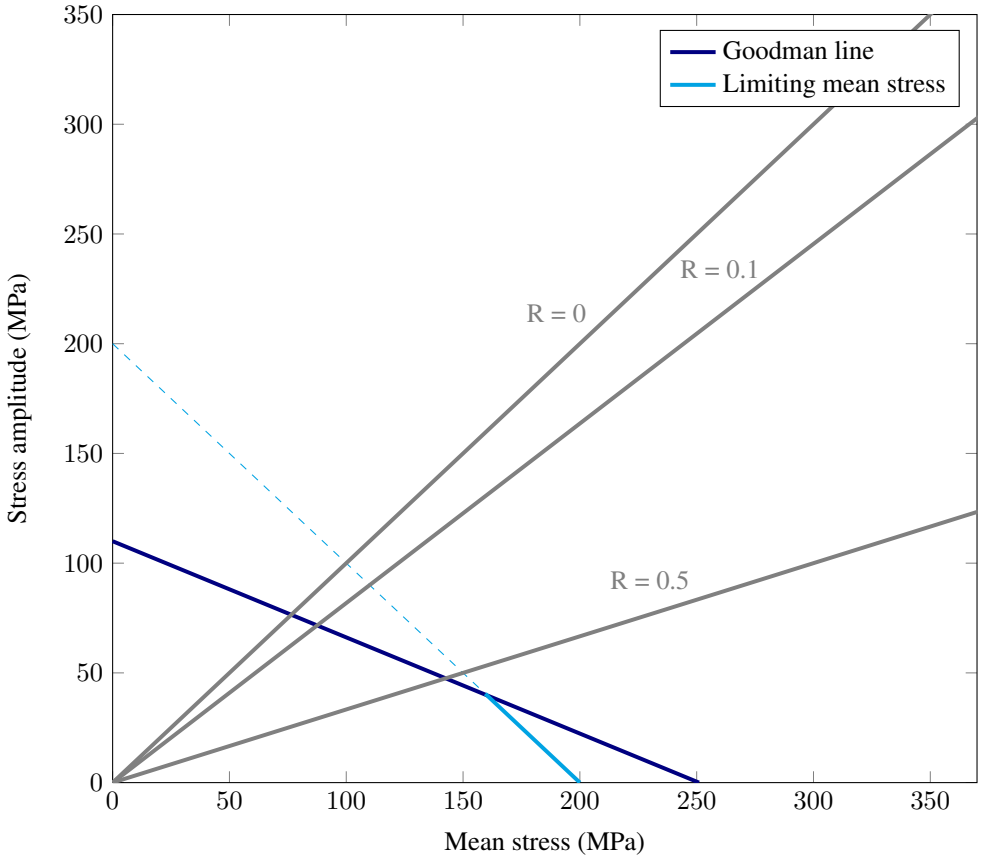

Figure 5.29: Goodman diagram for the post weld heat treated AA6082.50-T6.

Figure 5.30 shows the Goodman diagram for the shot peened specimens of AA6082-T6. The endurance limit is put to 130 MPa, the ultimate tensile strength used is 245 MPa and the yield strength is 160 MPa. This estimation show that a higher stress amplitude is possible for the shot peened specimens compared to the other specimens, and that the yield strength limits most of the safe operational area.

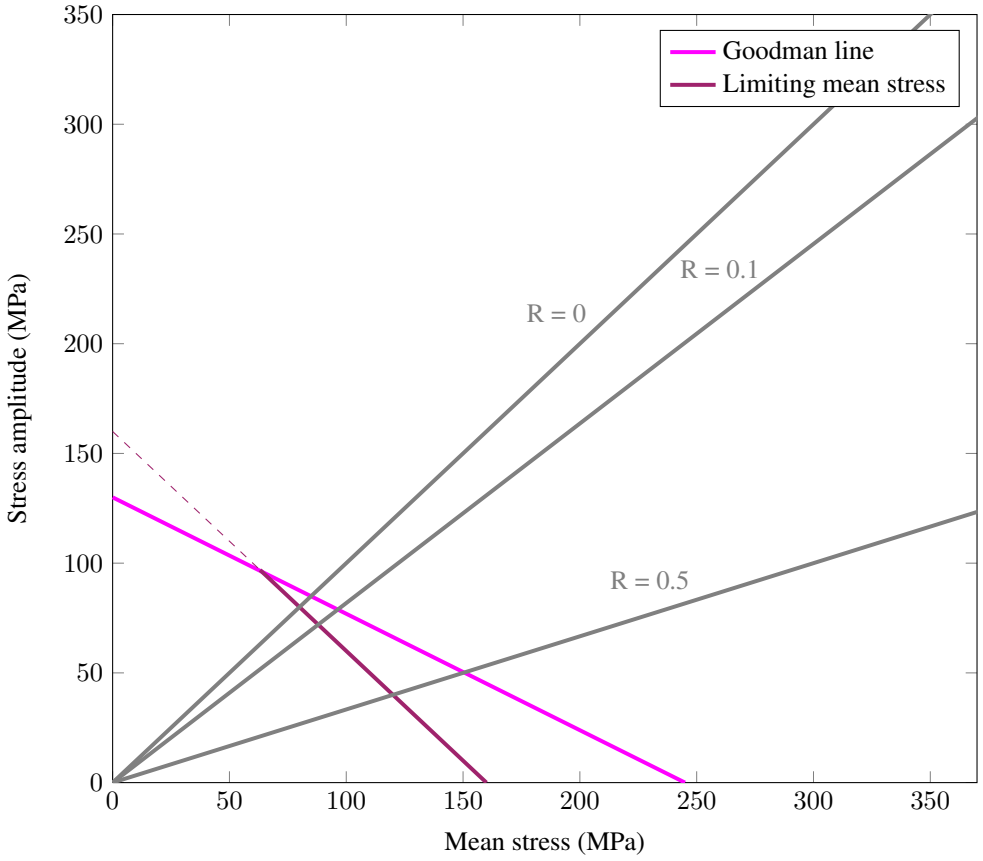

Figure 5.30: Goodman diagram for the shot peened AA6082.50-T6.

5.7 Fatigue fractography

Fractography was done to investigate the fracture surfaces and to locate the initiation points for the fatigue cracks. Two specimens were chosen from each S-N curve, the specimen with the fewest cycles to failure and the specimen with the most cycles to failure. The specimens were investigated both macroscopically and microscopically to document different stages of a fatigue crack; crack initiation (stage I), crack propagation (stage II) and the final fracture. Most of the specimens failed in the smallest cross section area.

5.7.1 Fractography of AA6082.52-T6 base material

The specimen with the fewest cycles to fracture, see Figure 5.31, is investigated in the images below, Figures 5.32 - 5.36.

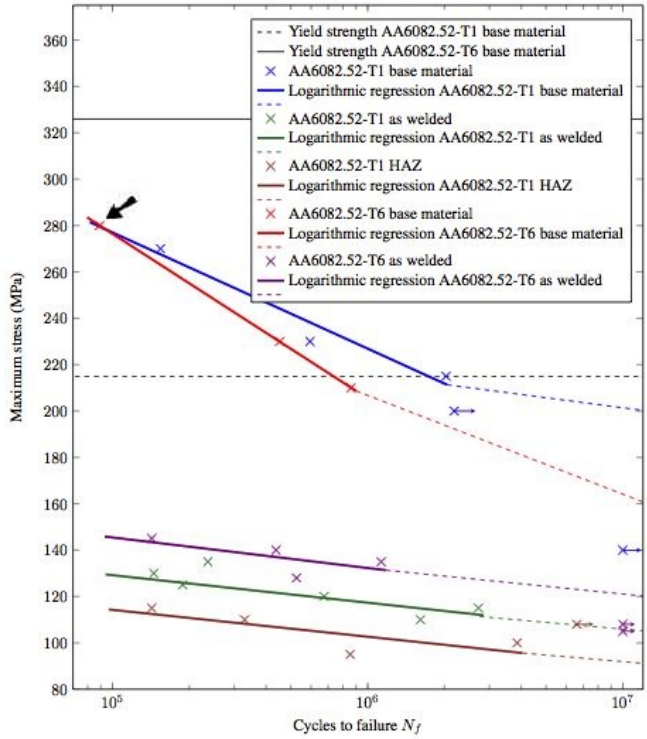

Figure 5.31: The arrow indicates the specimen with the fewest cycles to failure of the base material of AA6082.52-T6 investigated further below.

The specimen fractured after $9x10^5$ at a maximum applied stress of 280 MPa and the overview in Figure 5.32 show the initiation point along the surface on the top to the left (1). Ductile fracture surface resulting from the rapid fracture is visible to the right.

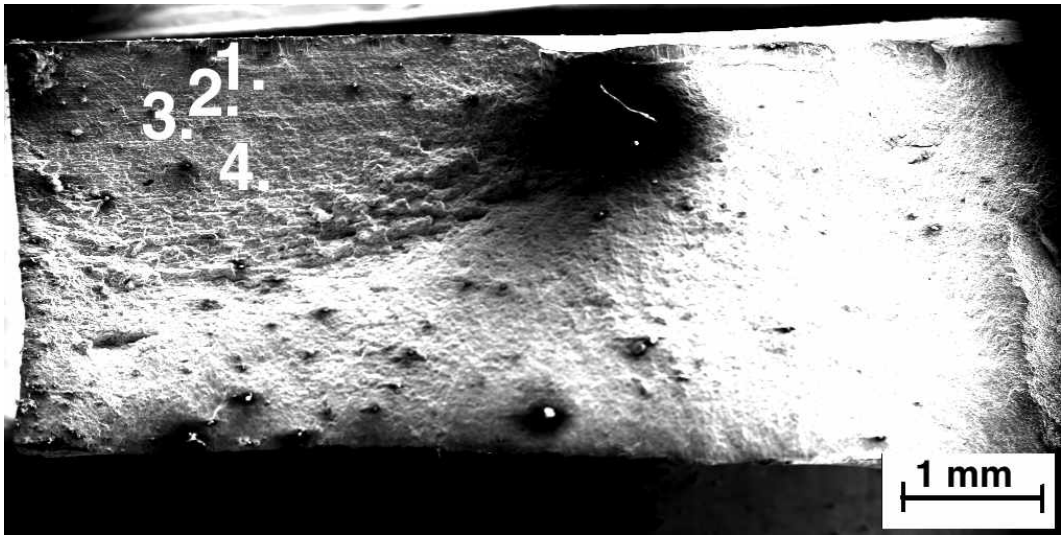

Figure 5.32: Overview of the fracture surface AA6082.52-T6 base material with fewest cycles to fracture. The numbers represent the different areas investigated further below.

The image to the left (1a), Figure 5.33, takes a closer look at the initiation point along the top surface. The image to the right (1b) show typical slip bands from the crack initiation stage.

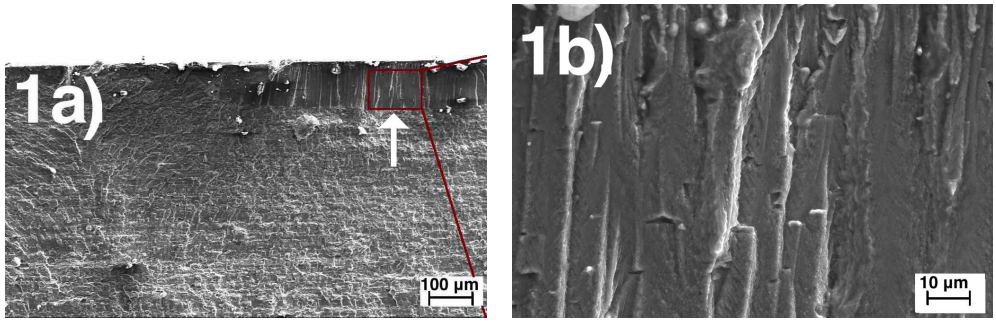

Figure 5.33: Initiation point of the fatigue crack of AA6082.52-T6 base material (1a). Slip bands are shown to the right (1b).

Further from the initiation point (2), Figure 5.34, some secondary cracks and slip bands can be seen in the micrograph to the left (2a) and typical fatigue striations to the right (2b). The average distance between each striations is found to be 0.15 μm.

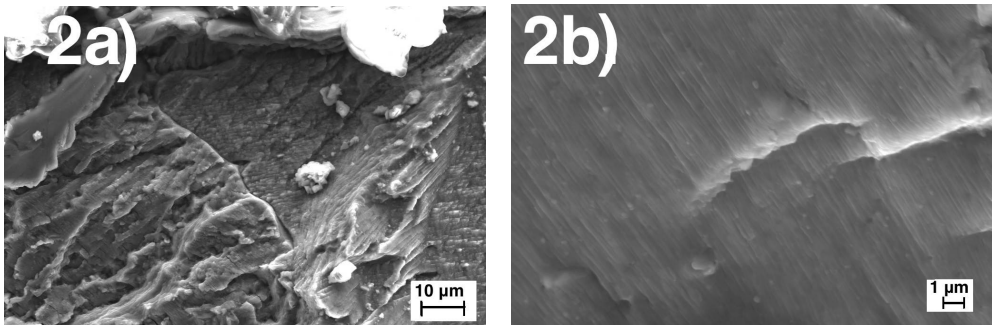

Figure 5.34: Secondary cracks shown to the left (2a) and striations to the right (2b) of AA6082.52-T6 base material.

Even further from the crack initiation point (3), Figure 5.35, more striations and internal cracks are found. The internal cracks are transgranular and the average distance between the striations is 0.16 μm.

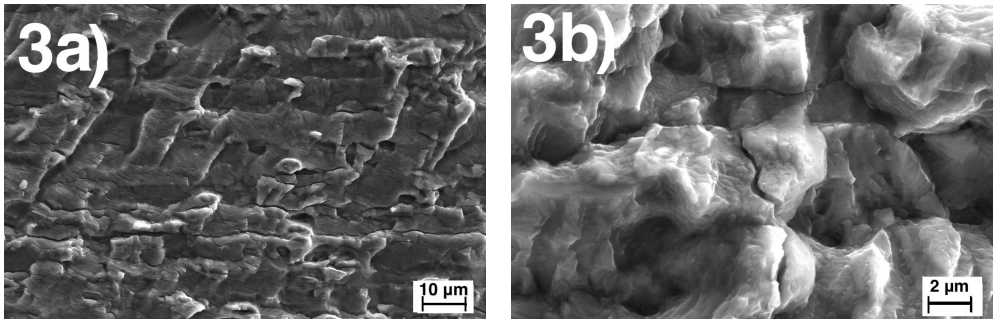

Figure 5.35: Striations and secondary transgranular cracks of AA6082.52-T6 base material.

Further from the initiation point, Figure 5.36, more transgranular cracks are found. The bright object to the left in the figure is probably a contamination on the surface.

Figure 5.36: Transgranular crack propagation (and some contaminations) on the surface of AA6082.52-T6 base material.

The specimen with the most cycles to fracture, see Figure 5.37, is investigated in the images below, Figures 5.38 - 5.42.

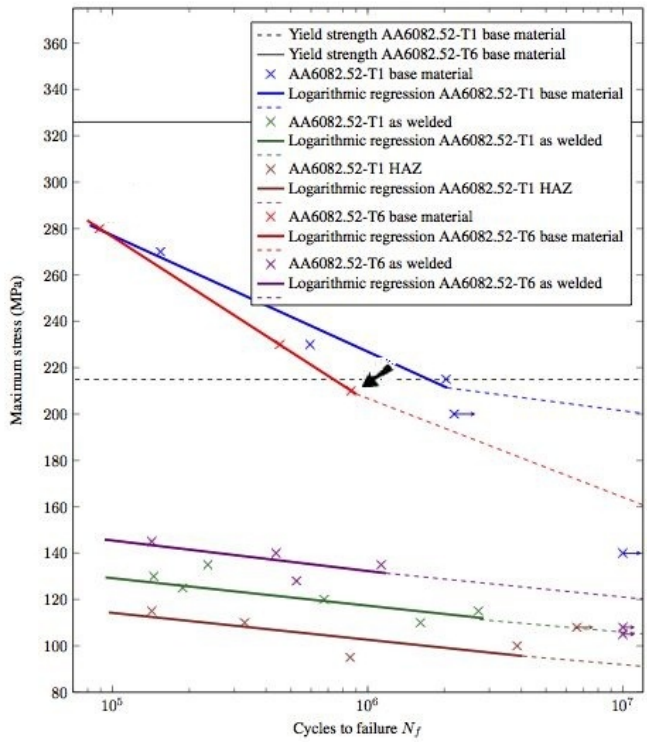

Figure 5.37: The arrow indicates the specimen with the most cycles to failure of AA6082.52-T6 base material investigated further below.

The AA6082.52-T6 base material specimen with the most cycles to failure, $8.6x10^5$ cycles at maximum applied stress at 210 MPa. The initiation point can be found at the top left corner, seen in Figure 5.38. Compared to the fractured surface above, the fatigue crack area of this specimen is larger than for the shorter lived specimen.

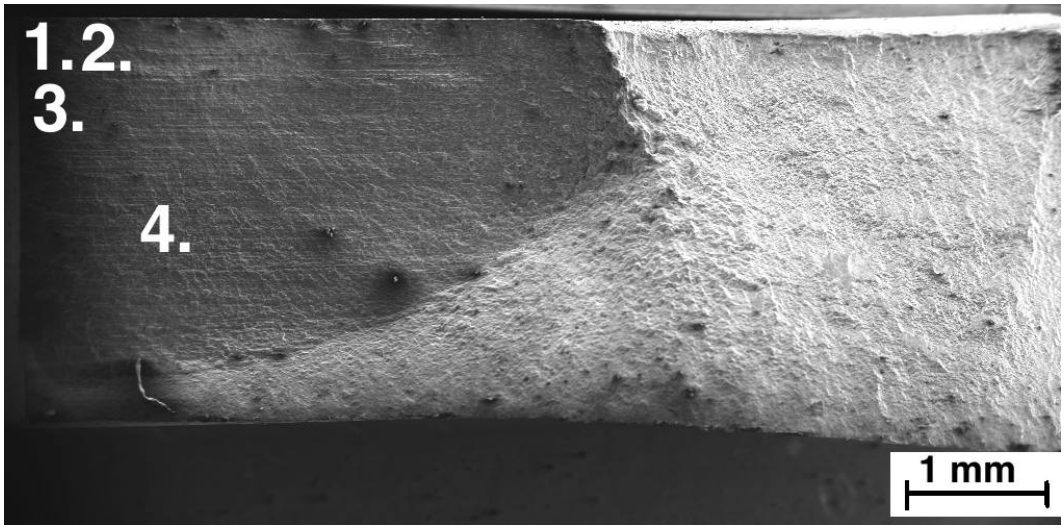

Figure 5.38: Overview of the fracture surface AA6082.52-T6 base material with most cycles to fracture. The numbers represent the different areas investigated further below.

A closer look at the initiation point (1a), Figure 5.39, show that the crack may have been initiated by particles along the surface. Slip bands after the crack has propagated outwards throughout the specimen are seen in the micrograph to the right (1b). The striations (1b) has an average distance of 0.55 μm.

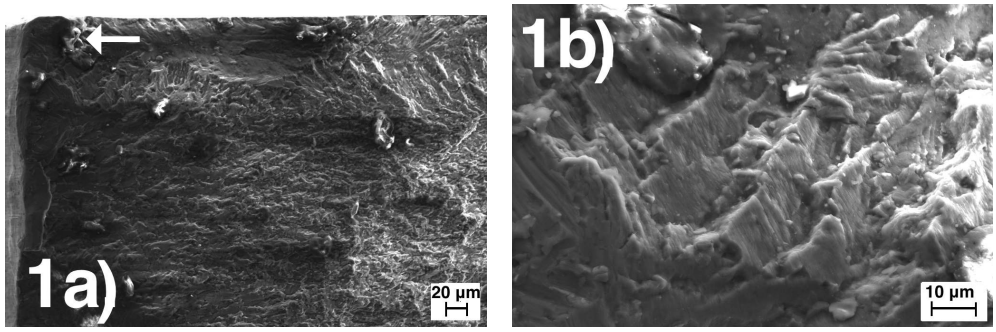

Figure 5.39: Initiation point of the fatigue crack of AA6082.52-T6 base material. Slip bands and striations shown to the right (1b).

The images in Figure 5.40 show typical intergranular crack propagation (2a) and large internal pores stretching more than 2 μm are visible in the micrograph to the right (2b).

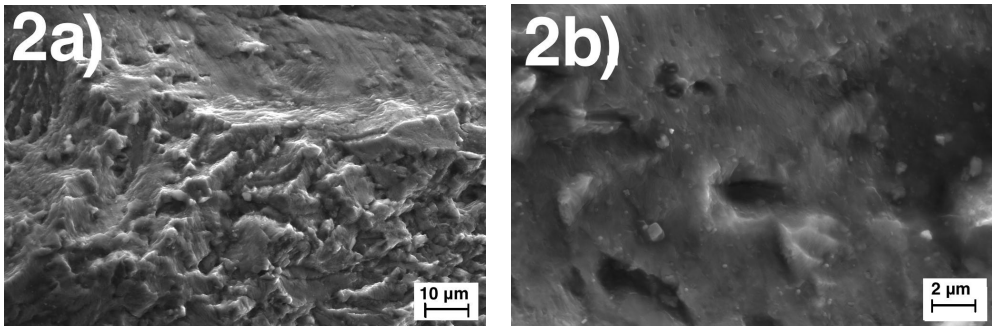

Figure 5.40: Secondary cracks and striations shown to the left (2a) and large internal pores to the right (2b) of AA6082.52-T6 base material.

Further from the crack initiation point, transgranular crack propagation and striations are found, Figure 5.41 . The distance between the striations (3b) is found to be 0.20 μm.

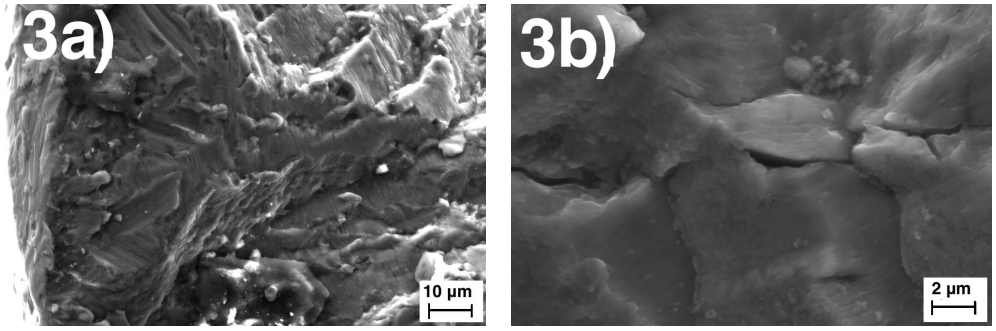

Figure 5.41: Transgranular cracks and striations of AA6082.52-T6 base material.

In Figure 5.42 typical tire tracks (4a) from the crack closure movements during crack propagation (stage II) are found quite far from the initiation point. A transgranular crack and striations are also found, with a distance of about 0.25 μm (4b).

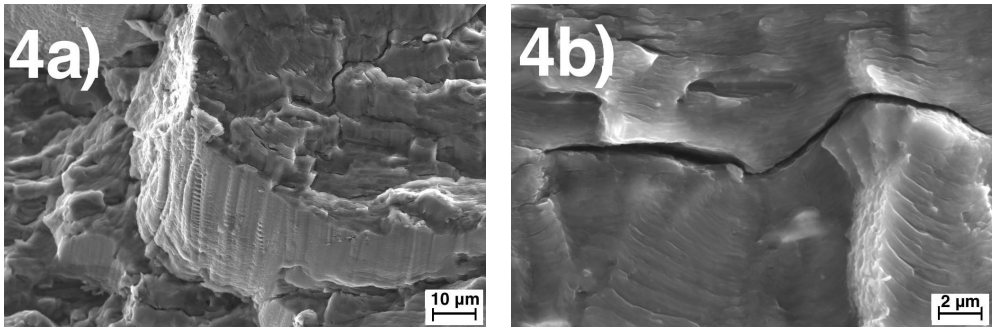

Figure 5.42: Tire tracks and internal cracks on the surface of AA6082.52-T6 base material.

5.7.2 Fractography of AA6082.52-T6 as welded

The specimen with the most cycles to fracture of the as welded AA6082.52-T6, see Figure 5.43, is investigated in the images below, Figures 5.44 - 5.49.

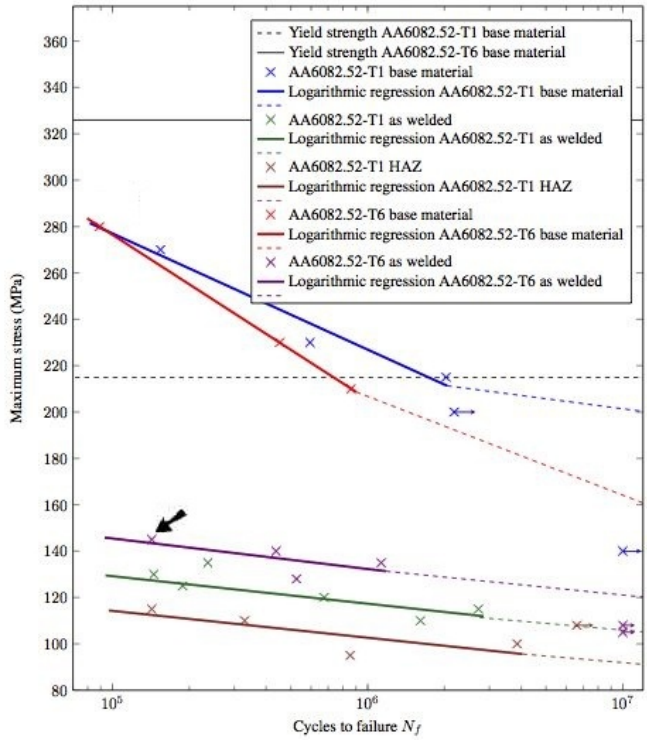

Figure 5.43: The arrow indicates the as welded AA6082.52-T6 specimen with the most cycles to failure investigated further below.

The overview of the as welded specimen of AA6082.52-T6, Figure 5.44, show the fracture surface of the specimen that fractured after $1.1x10^6$ cycles at 135 MPa. The surface show the initiation point at the bottom surface to the left. The surface also reveals large pores due to the welding.

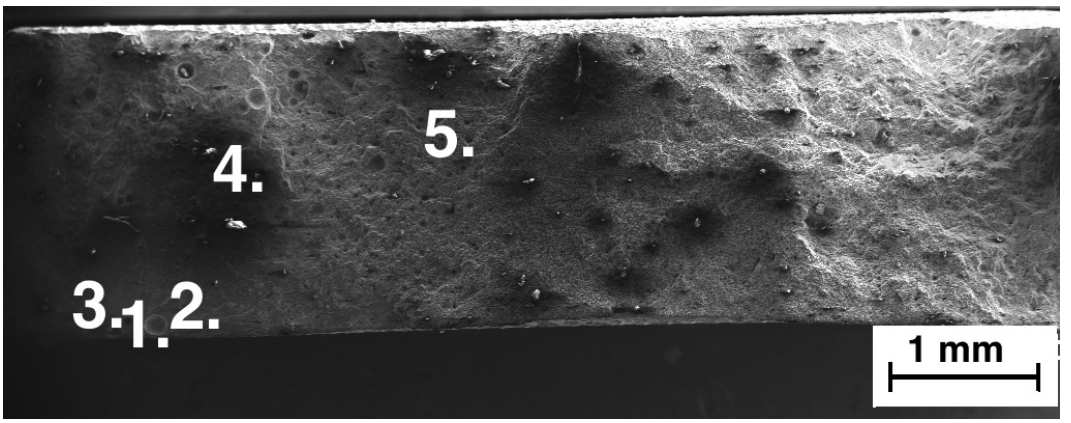

Figure 5.44: Overview of the fracture surface as welded AA6082.52-T6 with most cycles to fracture. The numbers represent the different areas investigated further below.

A closer look at the crack initiation point, Figure 5.45, show large pores as the cause of the fatigue failure. The largest pore in the left image (1a) is larger than 100 μm. The micrograph to the right (1b) show intergranular crack propagation out from the pore together with slip bands, seen to the left in the micrograph.

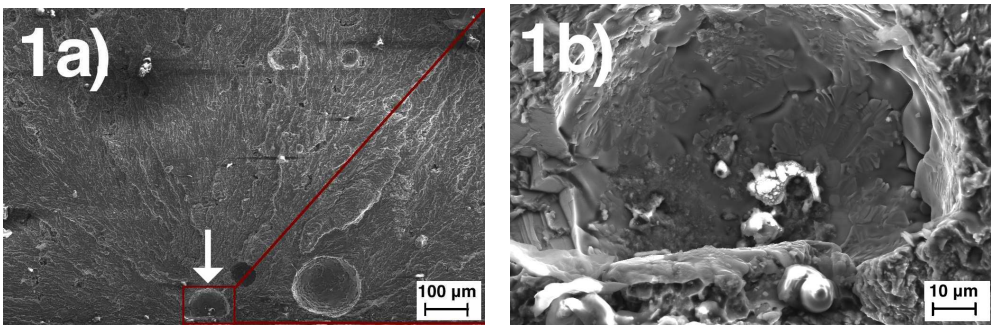

Figure 5.45: Initiation point of the fatigue crack of AA6082.52-T6 as welded at the bottom of the figure to the left (1a). A closer look at one of the pores are shown to the right (1b).

The larger pore is further investigated in Figure 5.46. To the right of the pore intergranular crack propagation and slip bands is seen.

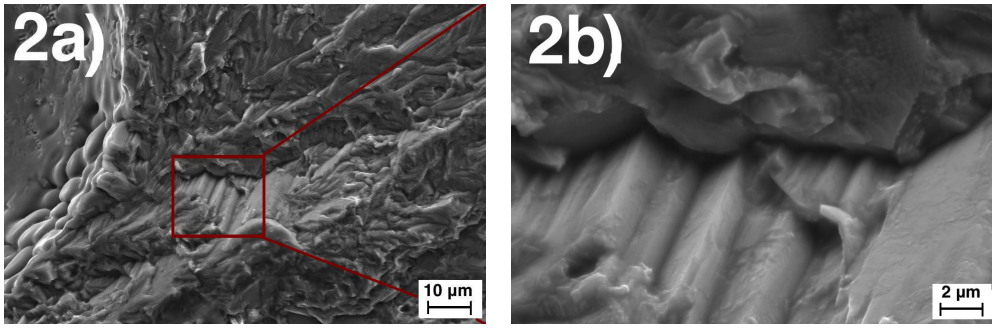

Figure 5.46: Secondary cracks shown to the left (2a) and slip bands to the right (2b) originating from one of the large pores around the initiation point.

Intergranular crack propagation is also found further from the initiation point, Figure 5.47. This is also close to one of the many pores on the surface, suggesting that there are many internal cracks propagating from these pores.

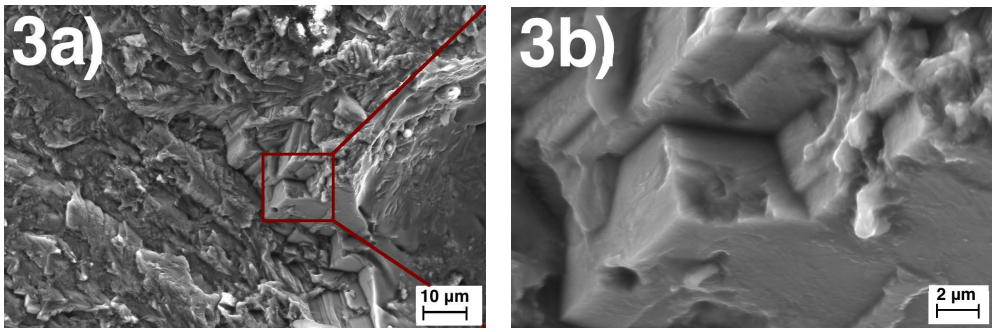

Figure 5.47: Intergranular crack propagation on the fractured surface of as welded AA6082.52-T6.

A large transgranular crack is seen in Figure 5.48 to the left (4a). In the image to the right (4b), striations with an average distance of 0.15 μm is found.

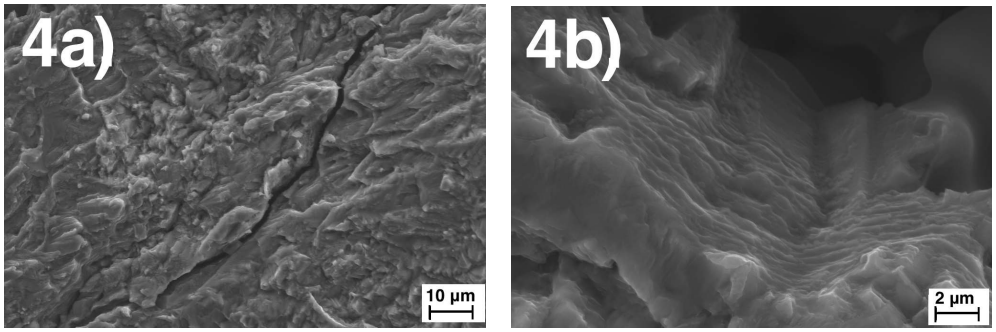

Figure 5.48: Transgranular cracks and striations of as welded AA6082.52-T6.

Far from the initiation point, Figure 5.49, intergranular and transgranular crack propagation are seen.

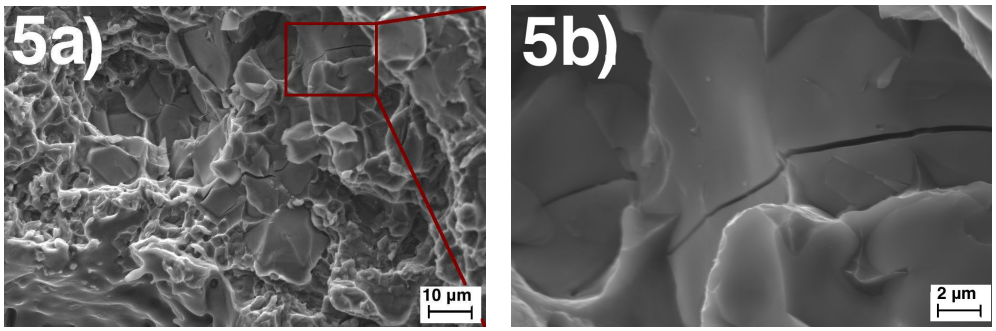

Figure 5.49: Transgranular and intergranular cracks of as welded AA6082.52-T6.

The specimen with the most cycles to fracture of the as welded AA6082.52-T6, see Figure 5.50, is investigated in the images below, Figures 5.51 - 5.55.

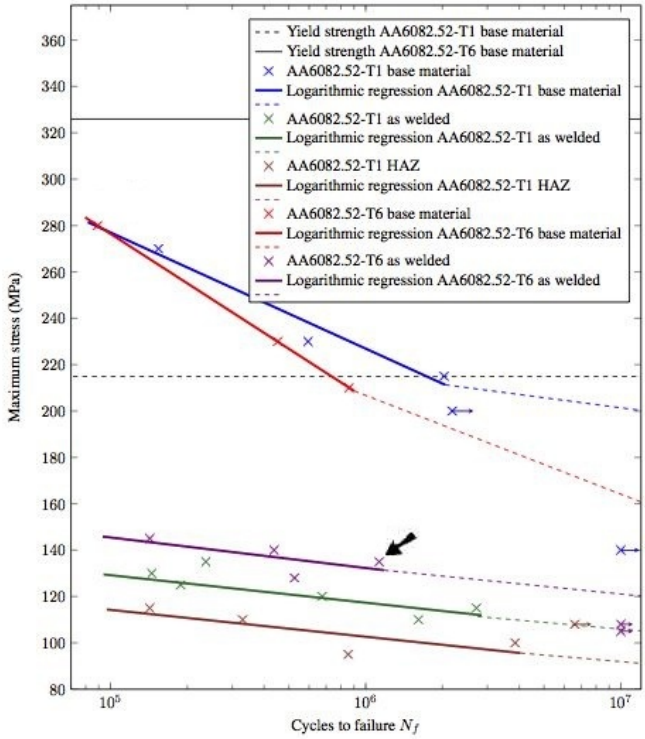

Figure 5.50: The arrow indicates the as welded specimen of AA6082.52-T6 specimen with the most cycles to failure investigated further below.

The specimen with the most cycles to failure, $4.4x10^5$ cycles at 140 MPa, also show large pores due to the welding, Figure 5.51. The fatigue fractured area has almost the same extent as the specimen above.

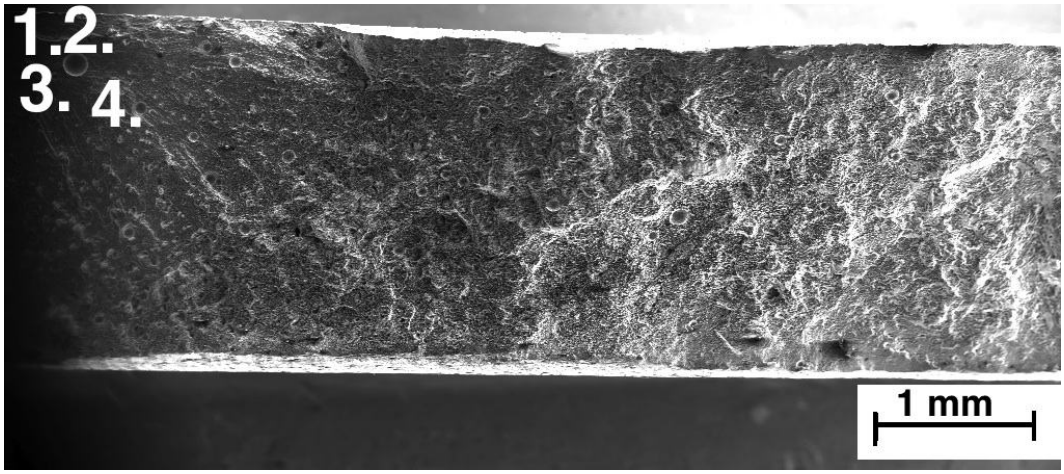

Figure 5.51: Overview of the fracture surface of as welded AA6082.52-T6 with most cycles to fracture. The numbers represents the different areas investigated further below.

The initiation point in the upper left corner show a large pore, stretching almost 200 μm in diameter. Another large pore can be seen in the middle of the micrograph, Figure 5.52.

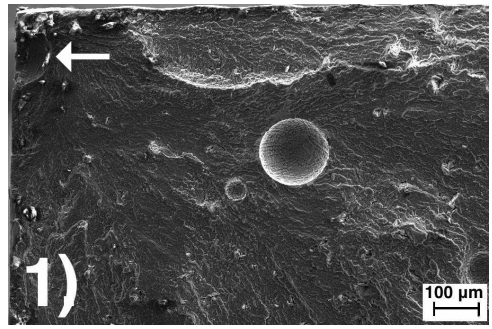

Figure 5.52: Initiation point of the fatigue crack up in the left corner and large internal pores of as welded AA6082.52-T6.

To the right of the crack initiation point in Figure 5.53, slip bands and river patterns can be seen progressing into the specimen.

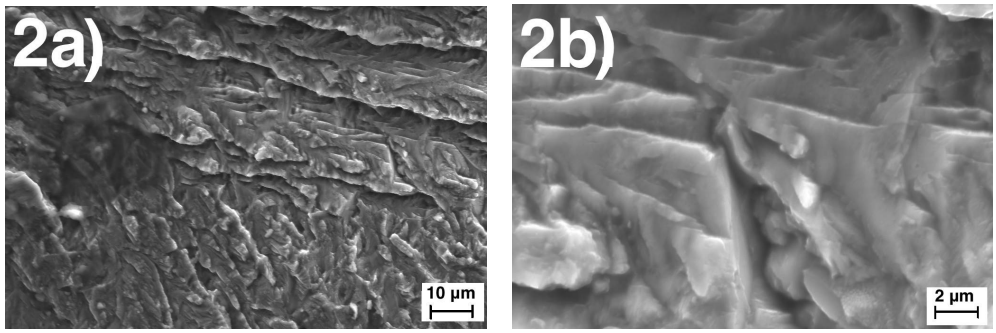

Figure 5.53: River patterns and slip bands on the fractured surface of AA6082.52-T6 as welded.

Other types of internal inhomogenities than the pores described above, can be seen in Figure 5.54. An internal pore can be seen to the left (3a) and striations with an average distance of 0.38 μm going out from this pore is shown to the right (3b).

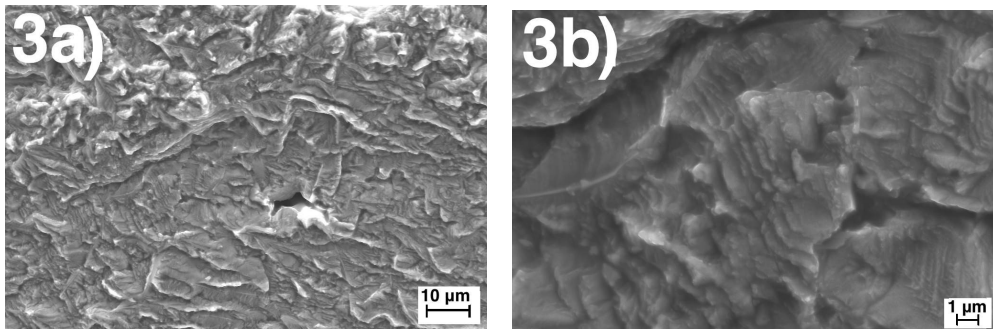

Figure 5.54: An internal pore and striations of as welded AA6082.52-T6.

A closer look at one of the pores on the fractured surface of AA6082.52-T6 due to the welding is shown in Figure 5.55. The size of the pore is approximately 40 μm in diameter (4a) and striations can be seen on top of the pore (4b) with an average distance of 0.44 μm.

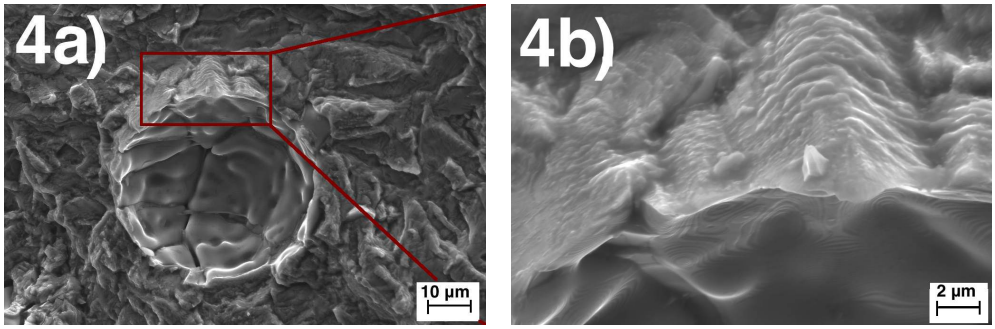

Figure 5.55: One of the larger pores on the surface and striations of as welded AA6082.52-T6.

5.7.3 Fractography of AA6082.50-T6 base material

The fractured surface of the base material of AA6082.50-T6 with the fewest cycles to failure is indicated by an arrow in Figure 5.56.

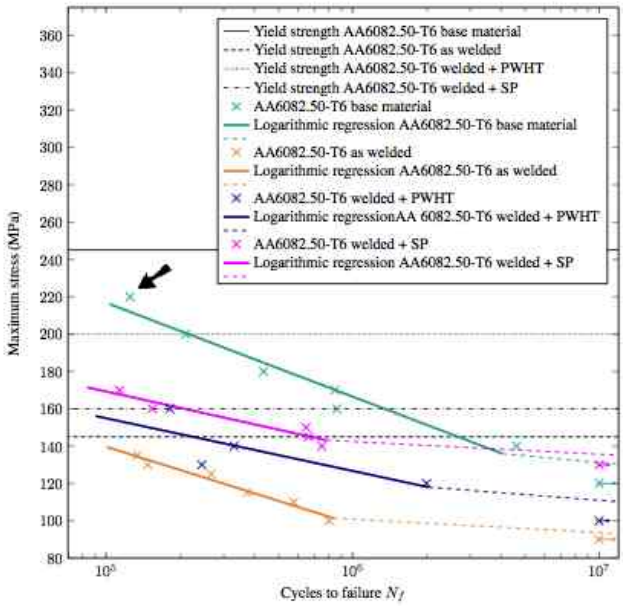

Figure 5.56: The arrow indicates the specimen with the fewest cycles to failure of the base material of AA6082.50-T6 investigated further below.

The fractured surface is investigated further below, Figures 5.58 - 5.62. The maximum stress was 220 MPa and the specimen fractured after $1.3x10^5$ cycles. Some contamination from the cutting preparation for the SEM can also be seen on the surface in Figure 5.57.

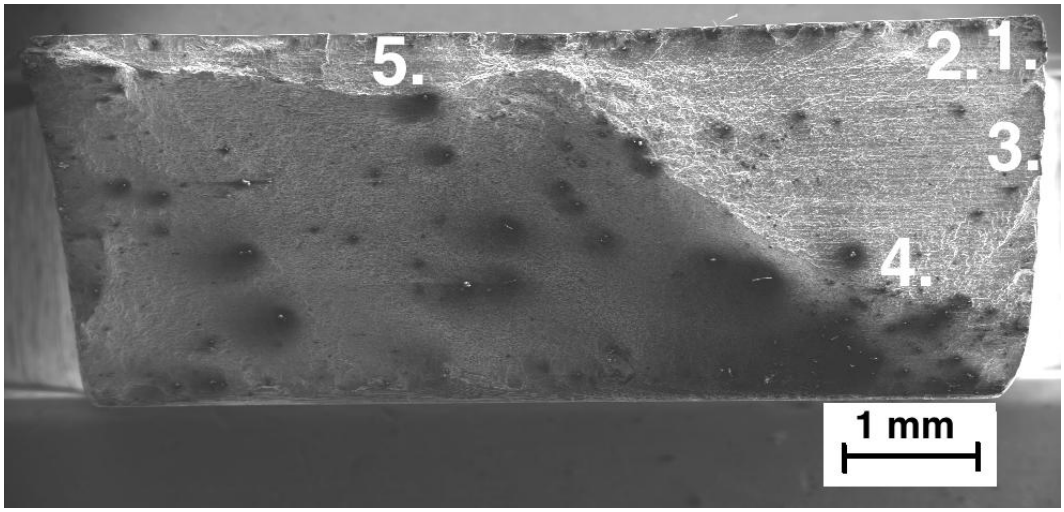

Figure 5.57: Overview of the fracture surface of base material AA6082.50-T6, the specimen with fewest cycles to fracture. The numbers represent the different areas investigated further below.

The initiation point of the fatigue crack can be seen along the top surface in Figure 5.58. Slip bands as the result of the crack progressing into the specimen are found by the initiation point.

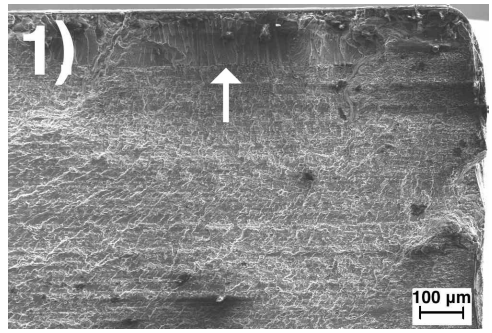

Figure 5.58: Initiation point along the top right surface of base material AA6082.50-T6.

Figure 5.59 show slip bands and river patterns to the left (2a) and secondary cracks (2b) just below the initiation point.

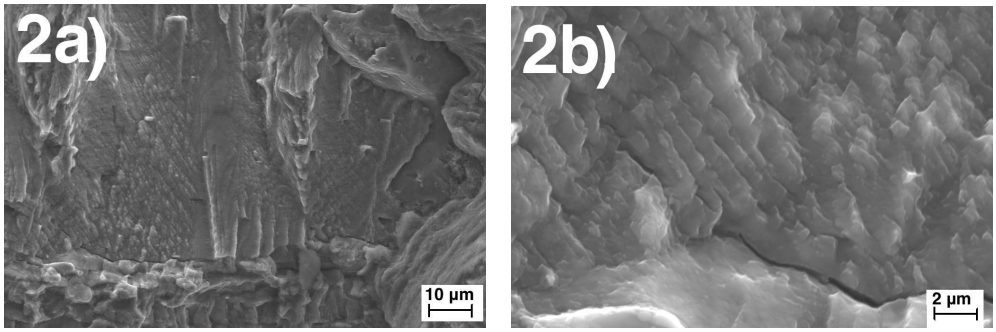

Figure 5.59: Fracture surface of base material AA6082.50-T6 with slip bands and secondary cracks.

Further from the initiation point, Figure 5.60, more secondary cracks and typical fatigue fracture surface features as striations are found. The striations have an average distance of 0.28 μm shown to the right (3b).

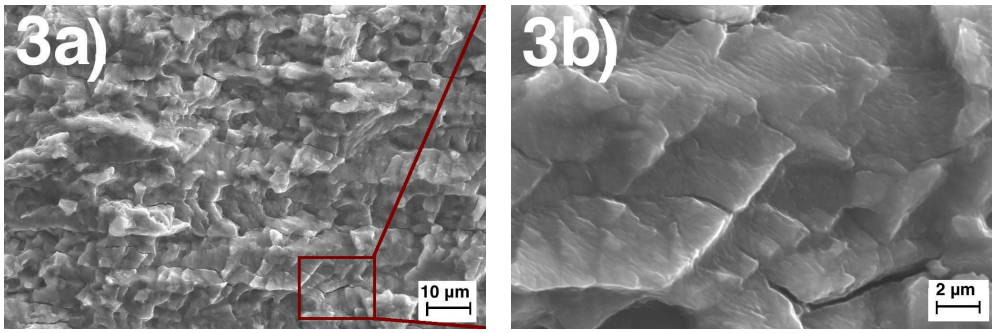

Figure 5.60: Secondary cracks and striations found below the initiation point.

At the transition area between fatigue failure and rapid failure, Figure 5.61, large internal cracks and striations are found.The striations shown to the right (4b) now have an average distance of 0.90 μm.

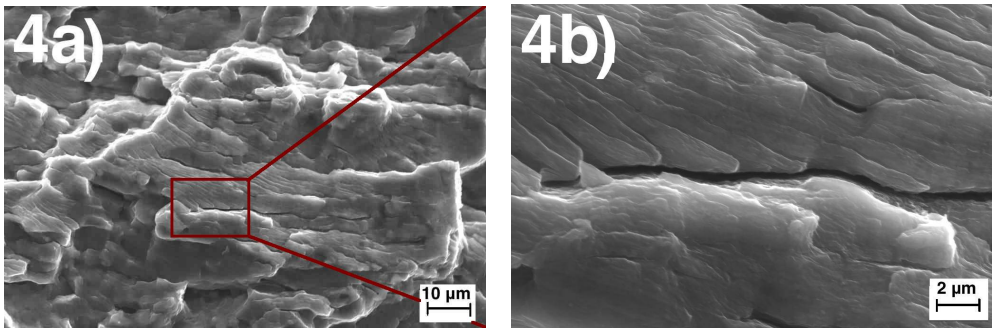

Figure 5.61: Fracture surface of the base material of AA6082.50-T6 with striations and transgranular cracks.

Far from the initiation point, Figure 5.62, a typical ductile fracture surface is found. The average distance between the striations to the right (5b) is 1.10 μm. Large pores are also shown in the micrograph to the right (5b).

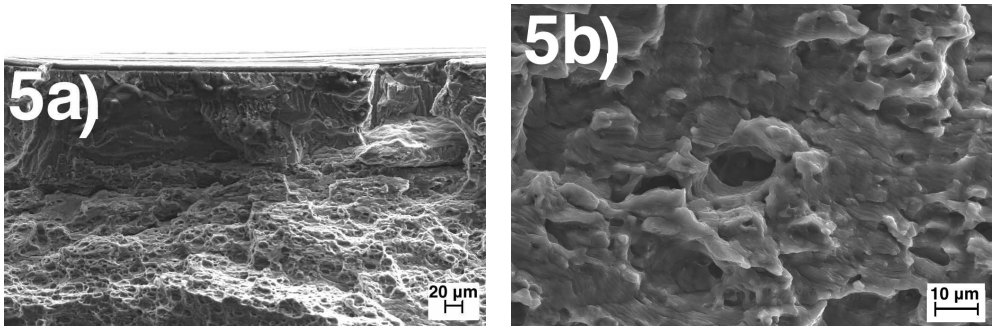

Figure 5.62: Ductile fracture surface of the base material AA6082.50-T6, far from the initiation point (5a) and striations and pores shown to the right (5b).

Figure 5.63 show the specimen with the most cycles to fracture for the base material of AA6082.50-T6. The maximum stress was 140 MPa and the specimen fractured after $4.6x10^6$ cycles.

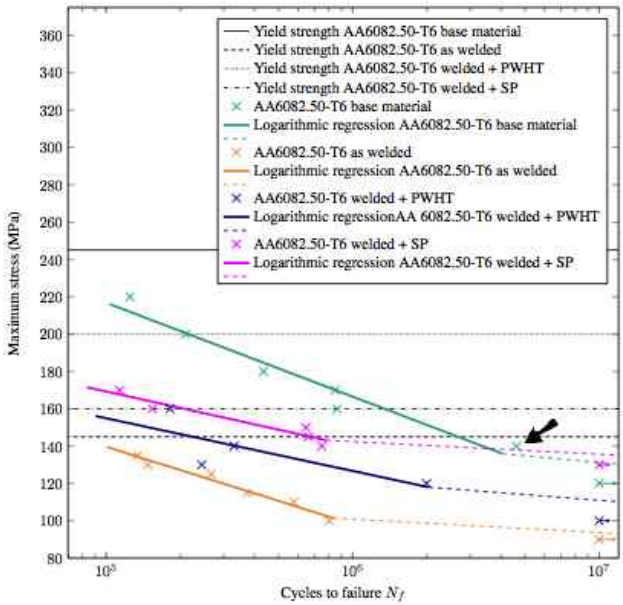

Figure 5.63: The arrow indicates the specimen with the most cycles to failure of the base material of AA6082.50-T6 investigated further below.

Figures 5.65 - 5.69 investigate the fractured surface of AA6082.50-T6 base material. This specimen, Figure 5.64, show a larger area where the specimen has failed due to fatigue compared to the specimen with the fewest cycles to failure.

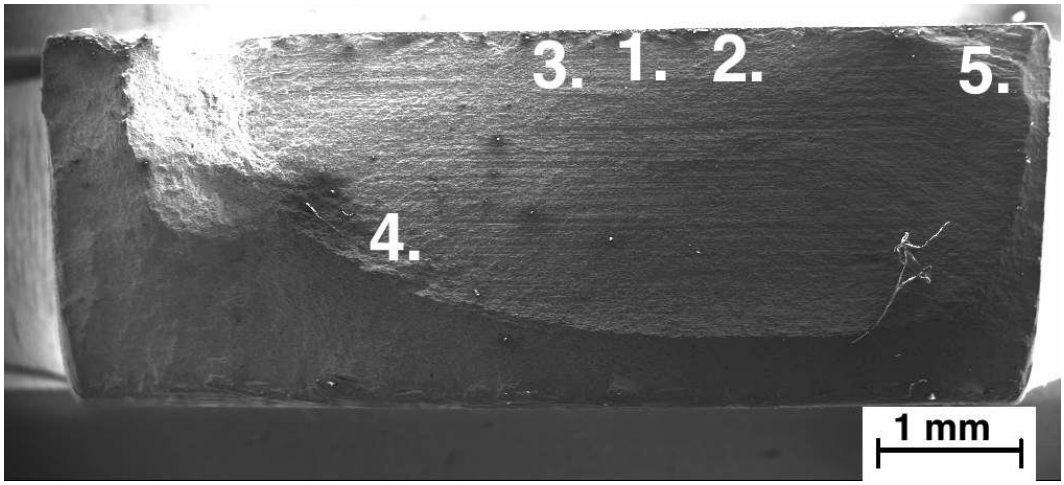

Figure 5.64: Overview of the fracture surface AA6082.50-T6 base material specimen with most cycles to fracture. The numbers represent the different areas investigated further below.

The initiation point is seen along the top surface, almost at the center. Figure 5.65 show a similar situation as the specimen above in Figure 5.58. From the initiation point, large slip bands are seen. The fractured surface then changes its feature as the fatigue crack has progressed inward into the specimen.

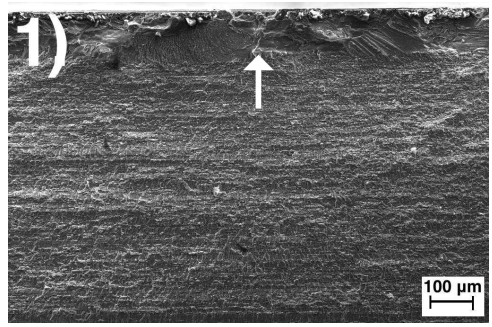

Figure 5.65: Initiation point along the top surface to the right of the fatigue crack of AA6082.50-T6 base material.

The slip bands made by the fatigue crack are shown in Figure 5.66. These slip bands are from the crack closure propagation of the fatigue crack.

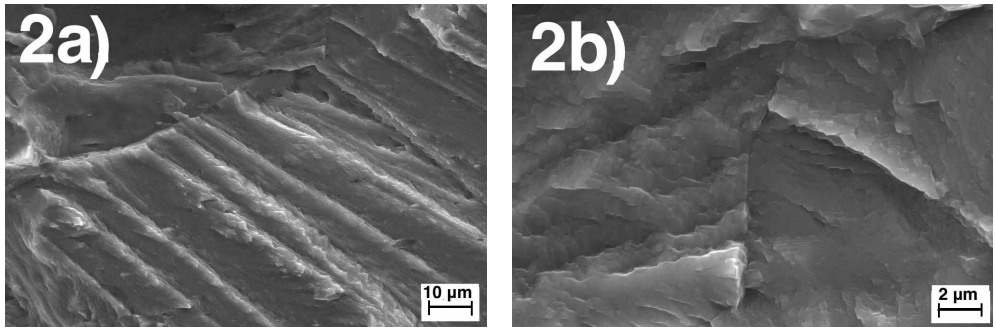

Figure 5.66: Fracture surface of AA6082.50-T6 base material. Slip bands shown to the left (2a.).

Intergranular crack propagation on the fractured surface is shown in Figure 5.67. In the micrograph to the right (3b) an internal secondary crack can be seen.

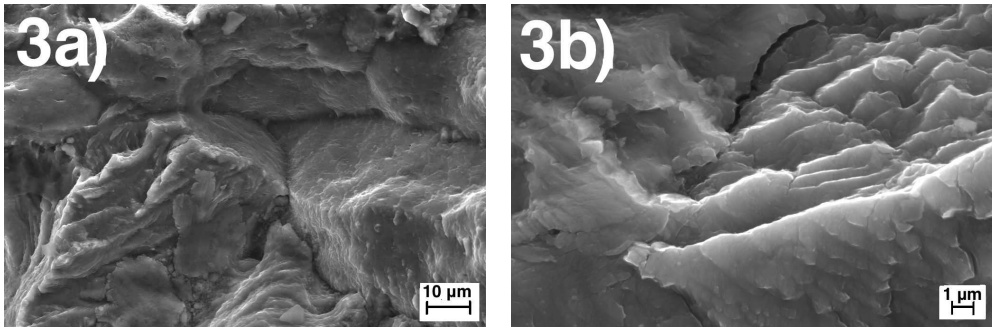

Figure 5.67: Intergranular cracks (3a) and slip bands (3b) on the fractured surface of AA6082.50-T6 base material.

In the area between the fatigue fracture surface and the ductile fracture surface, Figure 5.68, large secondary cracks and striations are found. The average distance between these striations to the right (4b) is 0.83 μm.

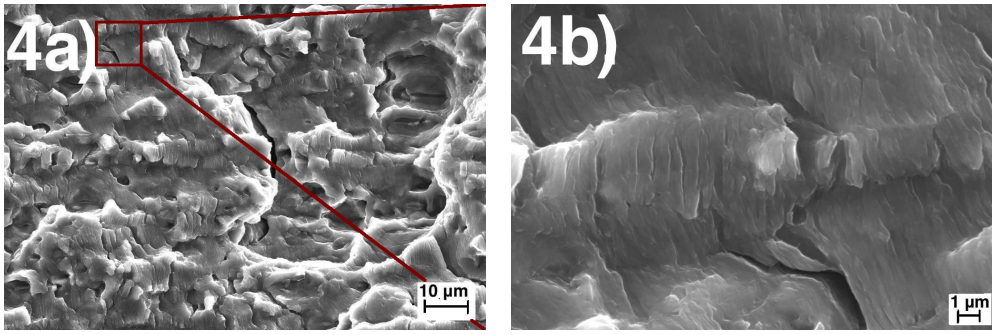

Figure 5.68: Secondary cracks and pores are shown in the micrograph to the left (4a) and striations to the right (4b).

In the top right corner of the specimen, shown in Figure 5.69, large secondary cracks are found on the surface.

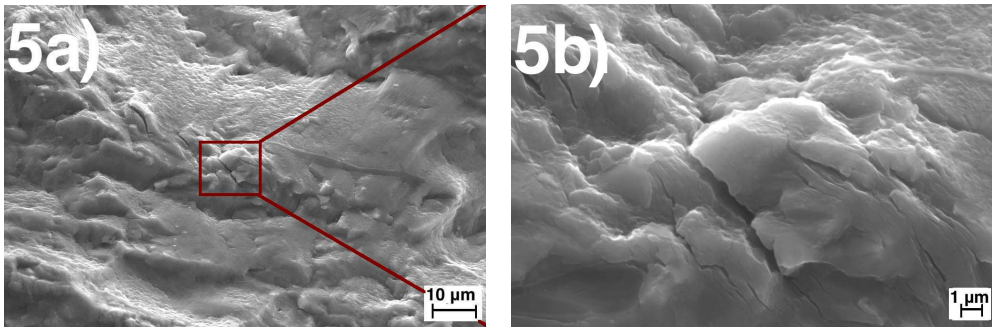

Figure 5.69: Far from the initiation point, large internal cracks can be found on the fractured surface of AA6082.50-T6 base material.

5.7.4 Fractography of AA6082.50-T6 as welded

Figures 5.71 - 5.75 show the fractured surface of the as welded AA6082.50-T6 specimen with the fewest cycles to failure, indicated with an arrow in Figure 5.70. The specimen fractured after $1.3x10^5$ cycles at a maximum stress of 135 MPa.

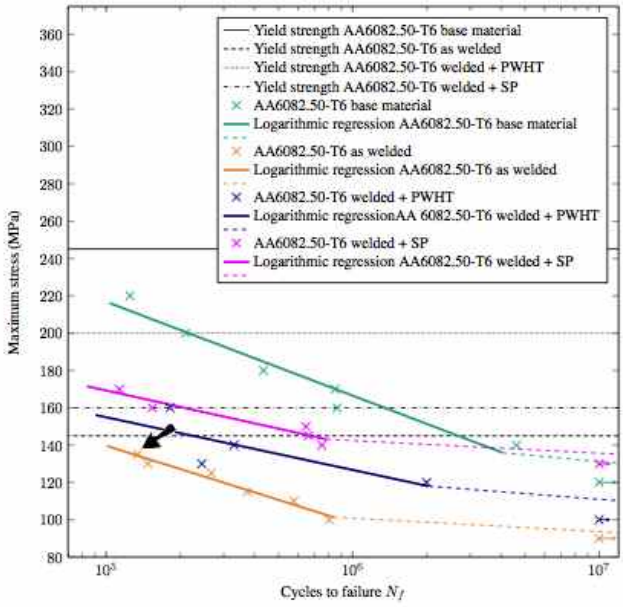

Figure 5.70: The arrow indicates the specimen with the fewest cycles to failure of the as welded AA6082.50-T6 investigated further below.

The initiation point is clearly seen as two large pores along the surface on top (1), Figure 5.71.

The figure also show that the fatigue crack has progressed further into the surface, and to the right the rapid fractured surface can be seen. The numbers represents the different areas investigated in more detail below.

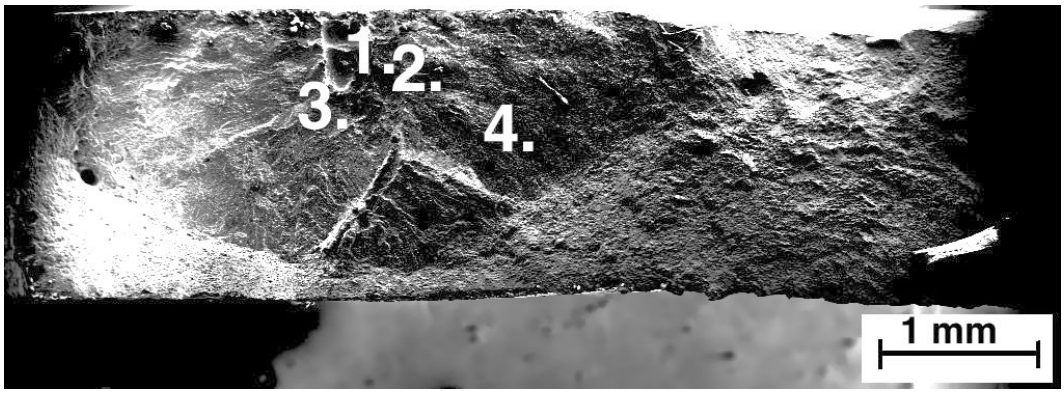

Figure 5.71: Overview of the fracture surface AA6082.50-T6 as welded specimen with fewest cycles to fracture. The numbers represent the different areas investigated further below.

A closer look at the pores where the fatigue crack started can be seen in Figure 5.72. The size of the pores are larger than 100 μm. More inhomogenities are seen surrounding the two pores, along with some oxidized particles to the top left.

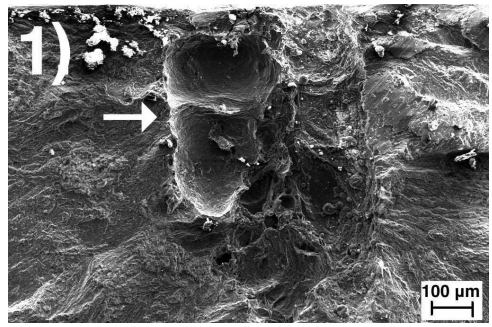

Figure 5.72: Large pores as the initiation point of the fatigue crack of AA6082.50-T6 as welded.

To the right of the initiation point, intergranular crack propagation can be seen in Figure 5.73 (2a). The micrograph to the right (2b) show striations with an average separation of 0.35 μm.

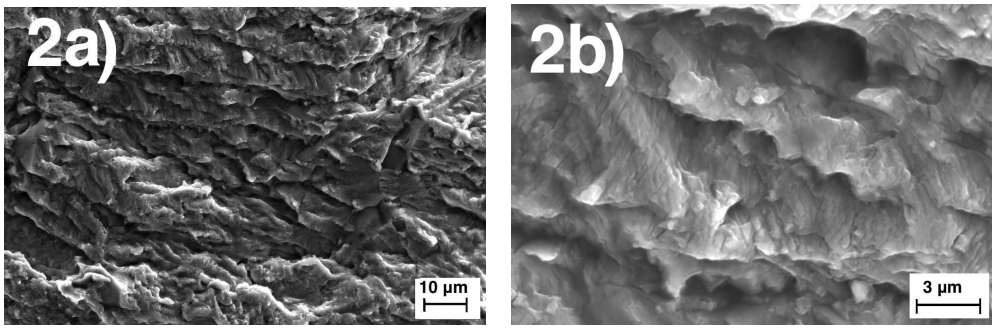

Figure 5.73: Fracture surface of AA6082.50-T6 as welded to the right of the initiation point. Striations shown to the right (2b.).

Further from the initiation point to the left, Figure 5.74, more transgranular cracks are found. The striations to the right (3b) have a distance of 0.20 μm on average.

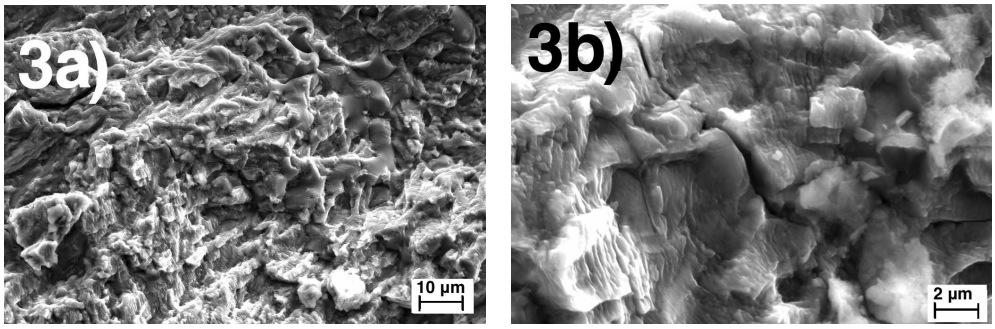

Figure 5.74: Transgranular secondary cracks and striations of AA6082.50-T6 as welded.

Far from the initiation point, Figure 5.75, slip bands are found along with striations. The striations have an average distance of 0.60 μm.

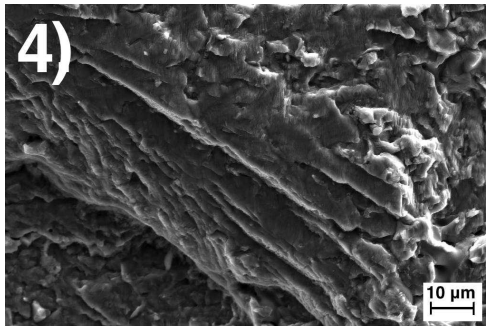

Figure 5.75: Slip bands and striations on the surface of AA6082.50-T6 as welded.

Figures 5.77 - 5.82 show the fractured surface of the as welded AA6082.50-T6 specimen with the most cycles to failure. The specimen fractured after $8.0x10^5$ cycles at a maximum stress of 100 MPa. The specimen is indicated with an arrow in Figure 5.76.

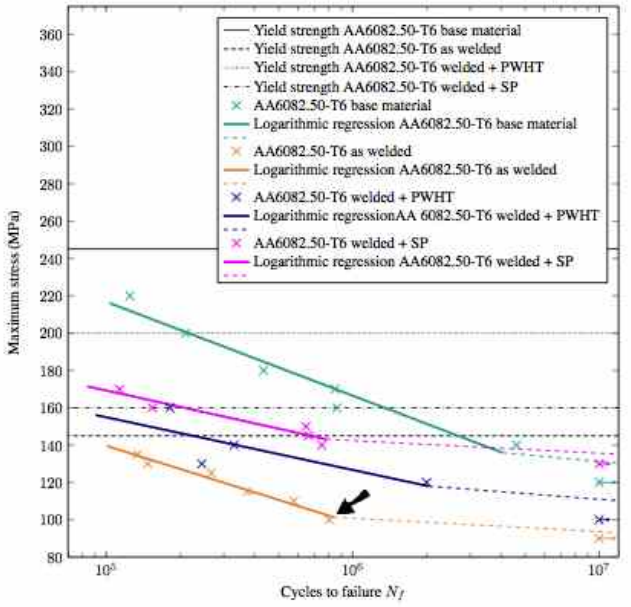

Figure 5.76: The arrow indicates the specimen with the most cycles to failure of the as welded AA6082.50-T6 investigated further below.

An overview of the fractured surface is given in Figure 5.77. The numbers represents the areas further investigated below. The fatigue fracture initiated at the top left corner (1). The fatigue failure area is much larger than the specimen above, the shorter lived specimen.

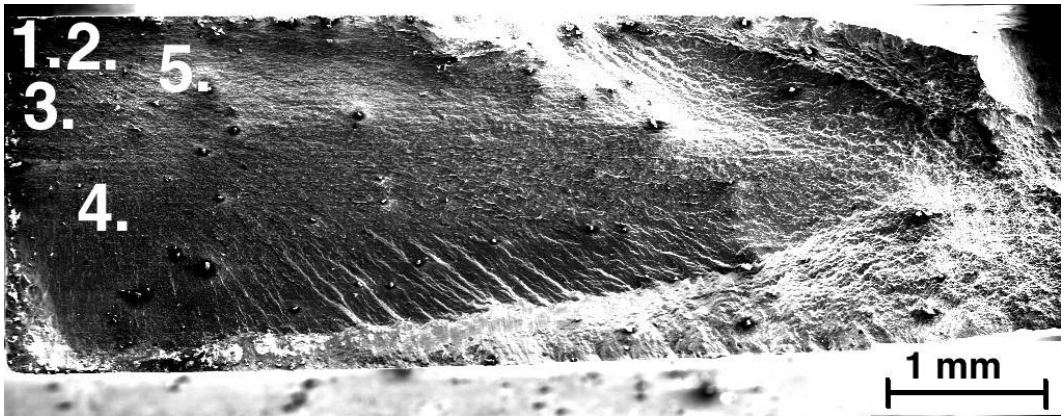

Figure 5.77: Overview of the fracture surface AA6082.50-T6 as welded specimen with most cycles to fracture. The numbers represent the different areas investigated further below.

The initiation point seemed to be an inhomogenity along the surface of the top left corner, Figure 5.78. Particles with oxide layers from the crack propagation are also seen.

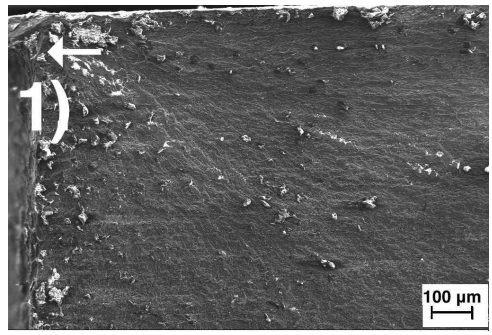

Figure 5.78: Initiation point in the top left corner of the fatigue crack of AA6082.50-T6 as welded.

More inhomogenities and pores can be seen in Figure 5.79. The micrograph to the left (2a.) show some of the particles with an oxide layer and typical river patterns. A pore is visible to the left in the micrograph to the right (2b), 3 μm in length.

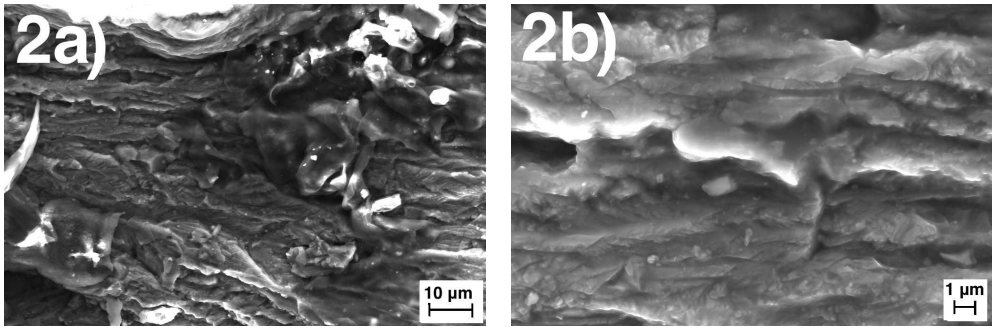

Figure 5.79: Fracture surface of AA6082.50-T6 as welded. Some oxide layer from the crack closure movement and river patterns to the left (2a) and one internal pore shown to the right (2b).

Slip bands from the crack propagation is shown in the micrograph to the left (3a) in Figure 5.80. The micrograph to the right (3b) show the result of an intergranular crack and some striations with an average distance of 0.20 μm. In the left micrograph (3b) the outline of a particle can be seen, about 5 μm in size.

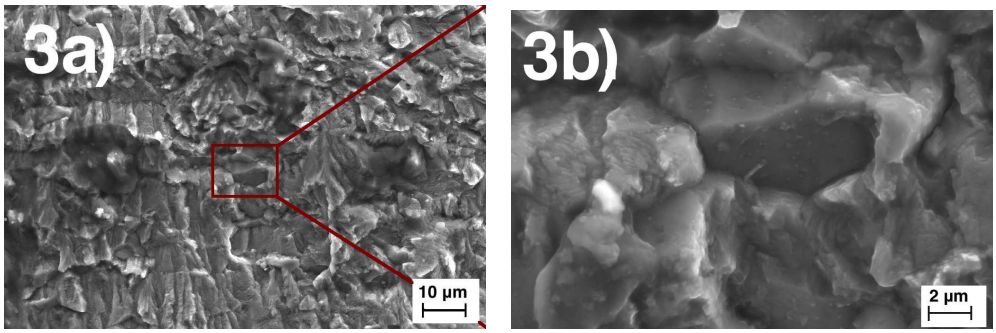

Figure 5.80: Slip bands (3a), intergranular cracks, striations and the outline of a particle (3b) of AA6082.50-T6 as welded.

Further from the initiation point, Figure 5.81, transgranular cracks can be found on the fractured surface. The micrograph to the right (4b) show a transgranular crack and striations with an average distance of 0.24 μm.

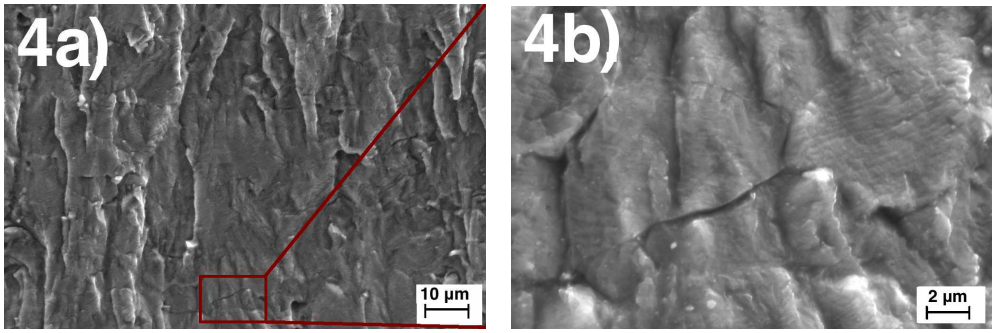

Figure 5.81: Transgranular cracks and striations of AA6082.50-T6 as welded.

Figure 5.82 show one of the particles found on the surface along with tire tracks, striations and slip bands. The size of the particle is approximately 20 μm.

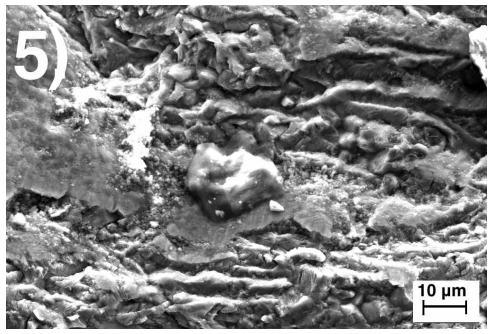

Figure 5.82: Particles and oxide layers on the surface of AA6082.50-T6 as welded.

5.7.5 Fractography of AA6082.50-T6 welded + PWHT

Figure 5.83 show the PWHT specimen with the fewest cycles to failure investigated below. The specimen fractured after $1.8x10^5$ cycles at a maximum applied stress of 160 MPa.

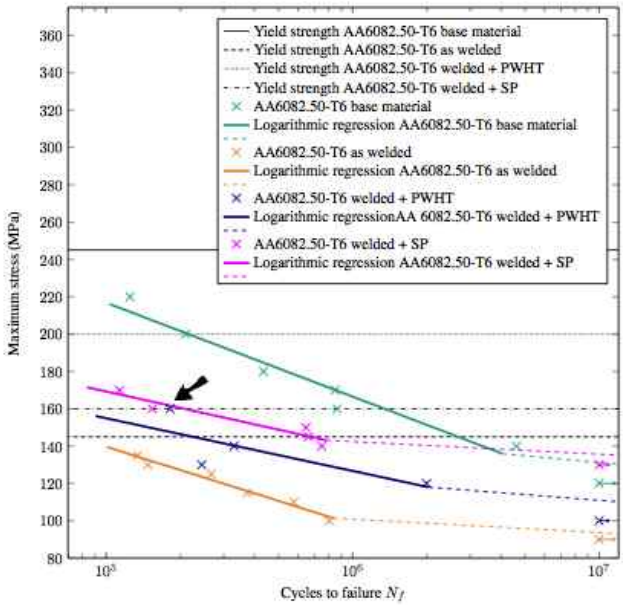

Figure 5.83: The arrow indicates the specimen with the fewest cycles to failure of the PWHT specimens of AA6082.50-T6 investigated further below.

The overview of the PWHT specimen of AA6082.50-T6, Figure 5.84, where the numbers represent the different areas investigated.

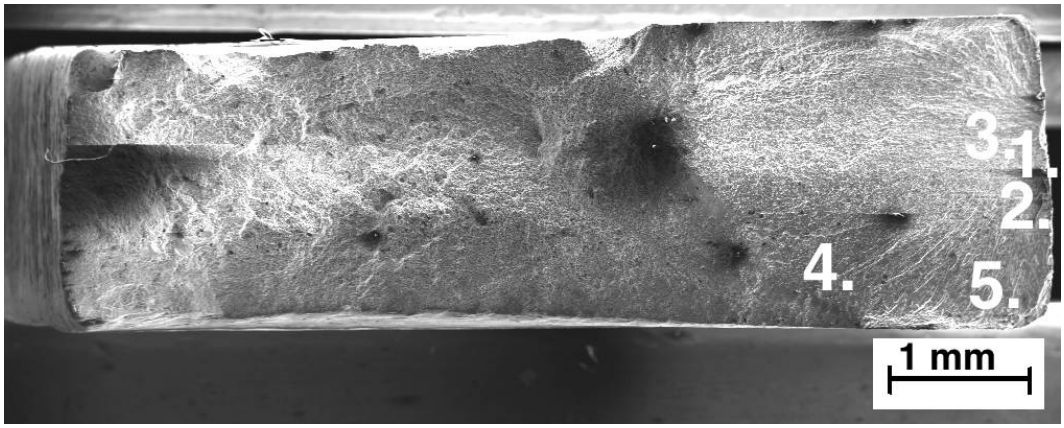

Figure 5.84: Overview of the fracture surface AA6082.50-T6 PWHT with fewest cycles to fracture. The numbers represent the different areas further investigated below.

Figure 5.85 show that the fatigue crack initiated from a discontinuity on the right edge of the specimen.

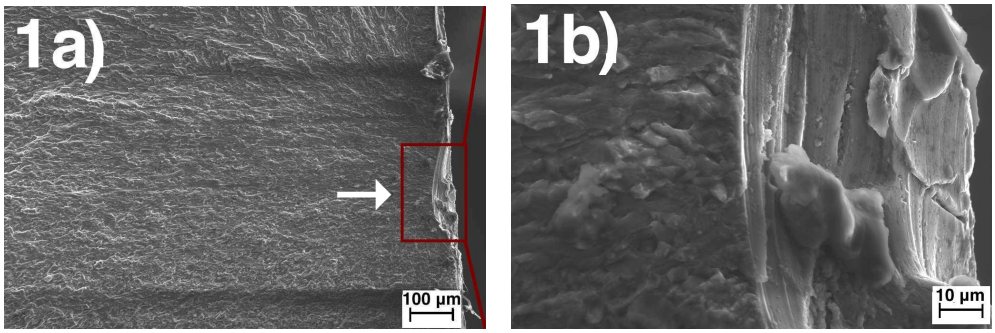

Figure 5.85: Initiation point of the fatigue crack of AA6082.50-T6 PWHT. The initiation point to the right in the the left micrograph (1a). A closer look at the initiation point is shown to the right (1b).

Below the initiation point, Figure 5.86, an intergranular fracture surface is observed. Typical river patterns can also be seen in the micrographs.

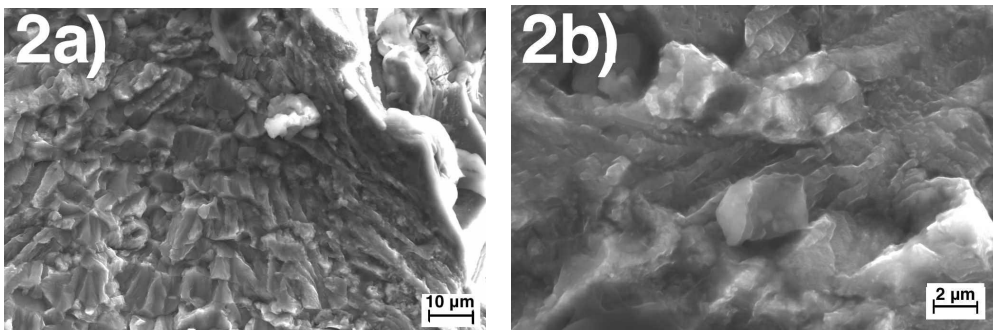

Figure 5.86: The fractured surface not far from the initiation point showing typical river patterns.

Above the initiation point, Figure 5.87, more intergranular fracture surface characteristics and river patterns are seen. A transgranular crack can also be found in the micrograph to the right (3b).

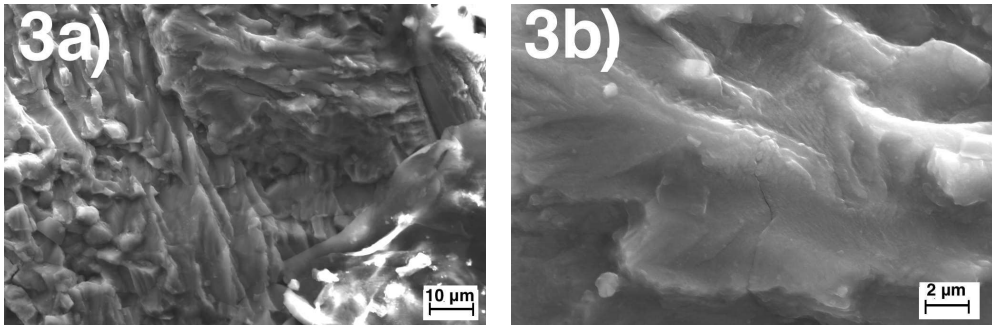

Figure 5.87: Intergranular cracks and river patterns of AA6082.50-T6 PWHT.

Typical for low cycle fractured specimens are tire tracks as shown in Figure 5.88. These are found in the transition area between the fatigue crack propagation and the rapid fracture. The striations the right (4b) have an average distance of 0.78 μm. The grain boundary direction changes when going from tire tracks to striations (4b).

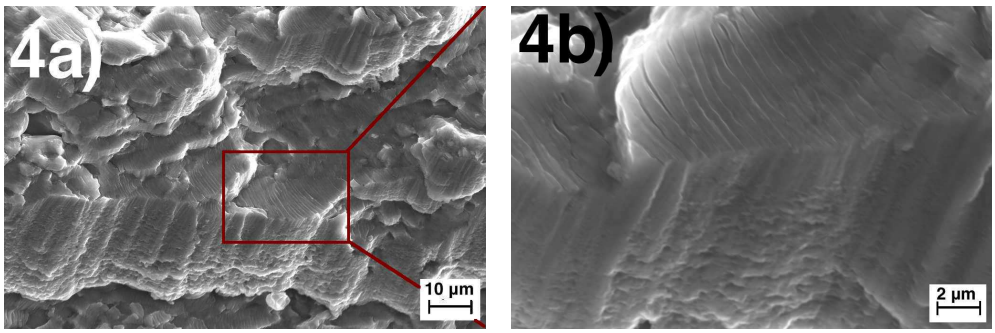

Figure 5.88: Tire tracks and striations of AA6082.50-T6 PWHT.

Figure 5.89 show transgranular crack propagation in the lower right corner. The striations in the right micrograph (5b) has an average distance of 0.28 μm.

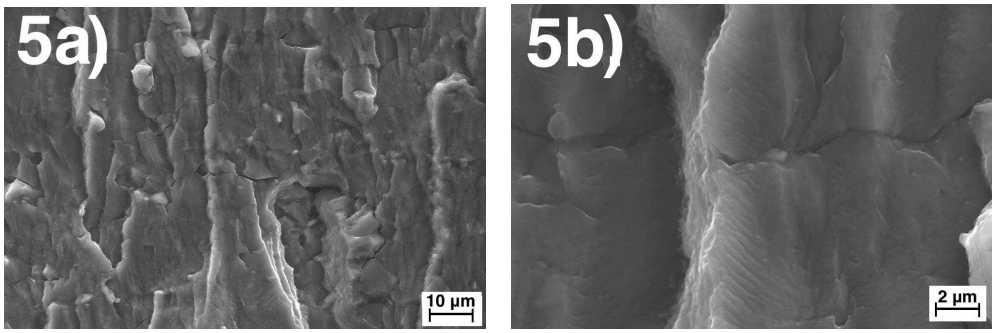

Figure 5.89: Transgranular cracks and striations of AA6082.50-T6 PWHT.

The PWHT specimen fractured after the most cycles to failure, is indicated with an arrow in Figure 5.90.

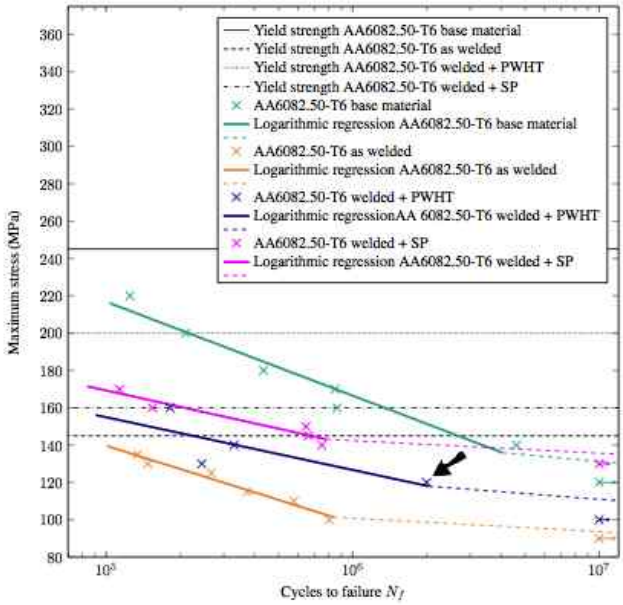

Figure 5.90: The arrow indicates the specimen with the most cycles to failure of the PWHT specimens of AA6082.50-T6 investigated further below.

The overview of the PWHT specimen of AA6082.50-T6, Figure 5.91, show the fracture surface of the specimen that fractured at a maximum applied stress of 120 MPa after $2.0x10^6$ cycles

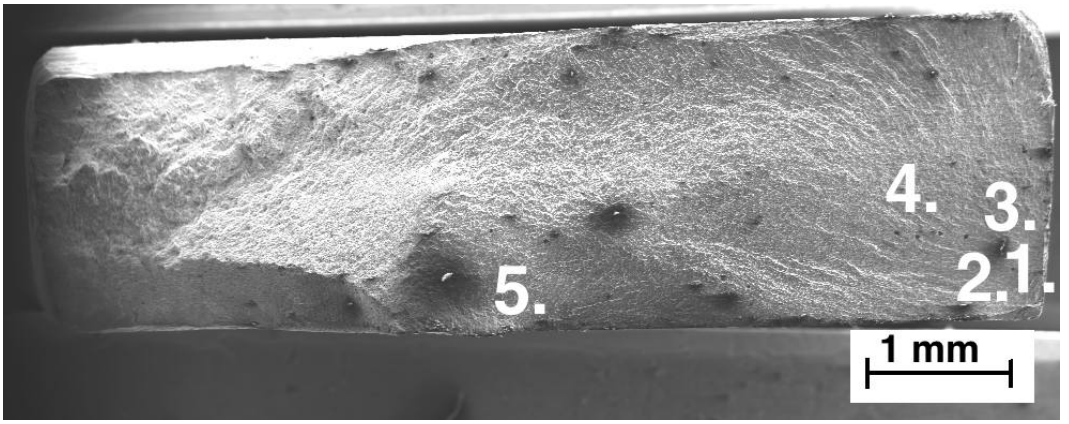

Figure 5.91: Overview of the fracture surface AA6082.50-T6 PWHT with most cycles to fracture. The numbers represent the different areas investigated further below.

Figure 5.92 show that the fatigue crack initiated from a notch on the right edge of the specimen, as for the specimen above. The notch is shown in the micrograph to the right (1b). The size of the notch exceeds 20 μm.

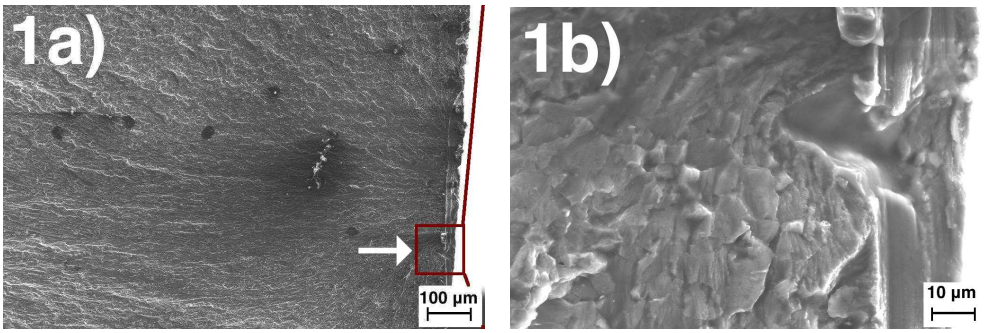

Figure 5.92: Initiation point of the fatigue crack of AA6082.50-T6 PWHT to the right in the the left micrograph (1a). A closer look at the notch is shown to the right (1b).

The fractured surface below the initiation point show an intergranular crack propagation, seen Figure 5.93.

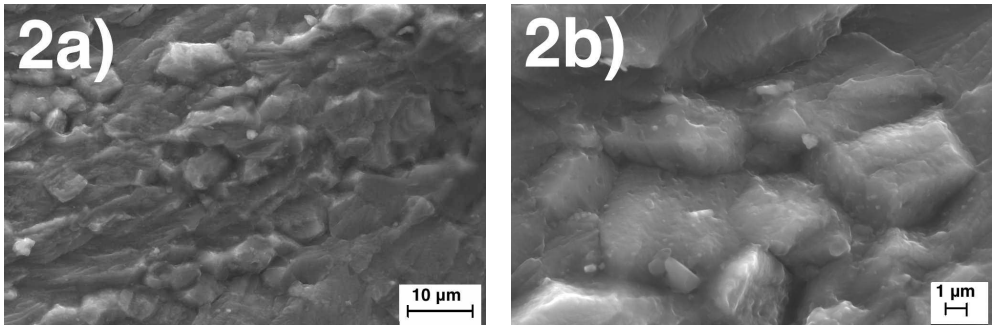

Figure 5.93: Intergranular fractured surface below the initiation point.

The area above the initiation point, Figure 5.94, has microvoids (3a) and slip bands (3b) from the crack propagation.

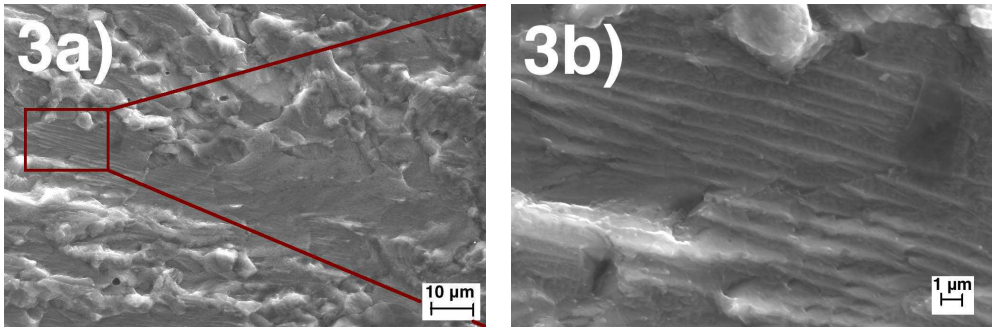

Figure 5.94: Slip bands and small pores on the fractured surface of AA6082.50-T6 PWHT.

Transgranular crack propagation (4a) is seen in Figure 5.95 along with more microvoids of about 2 μm in diameter (4b).

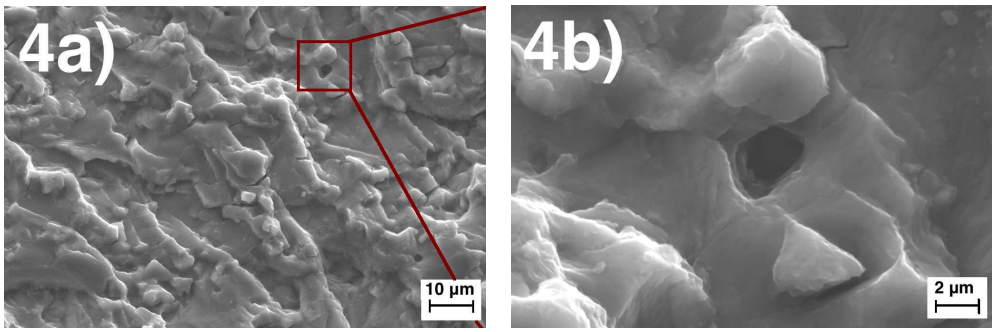

Figure 5.95: Transgranular fracture surface and microvoids of AA6082.50-T6 PWHT.

Figure 5.96 show a secondary notch along the surface, in the transition area between the fatigue crack propagation and the rapid fracture. The striations in the left micrograph (5a) have an average distance of 0.28 μm. The micrograph to the right (5b) show typical tire tracks.

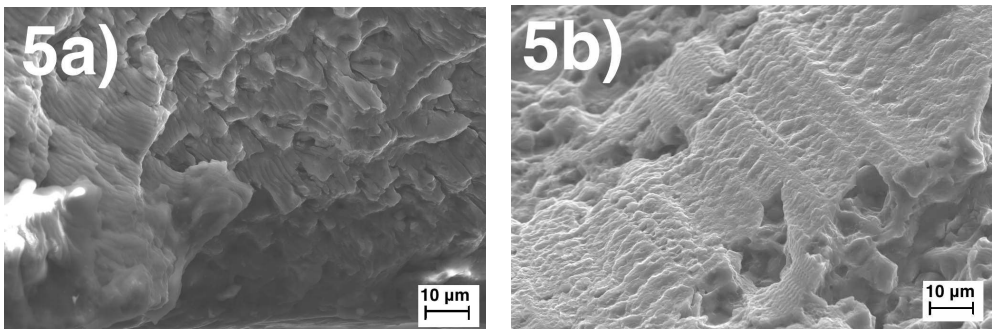

Figure 5.96: A secondary crack along with striations (5a) and tire tracks (5b) of AA6082.50-T6 PWHT.

5.7.6 Fractography of AA6082.50-T6 welded + SP

Figure 5.97 show the shot peened specimen that fractured after the fewest cycles to failure. The specimen fractured after $1.0x10^5$ cycles at 170 MPa maximum applied stress.

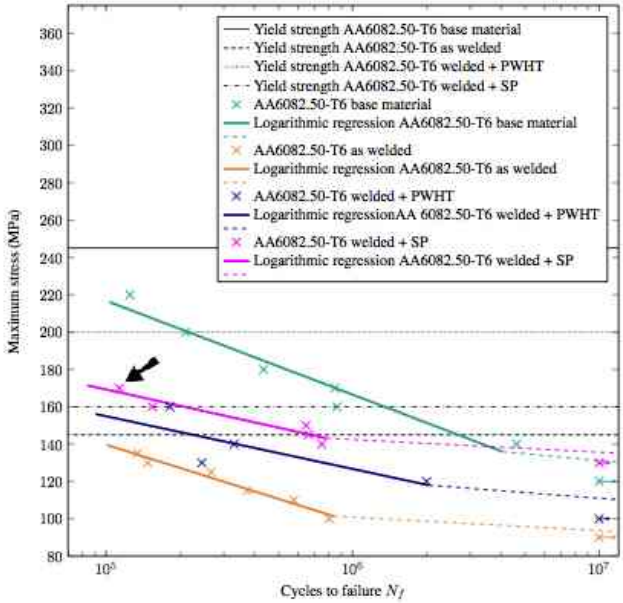

Figure 5.97: The arrow indicates the specimen with the fewest cycles to failure of the shot peened specimens of AA6082.50-T6 investigated further below.

Figure 5.98 show the overview of the shot peened specimen of AA6082.50-T6. The numbers represent the different areas investigated in more detail below. Some debris have contaminated the surface.

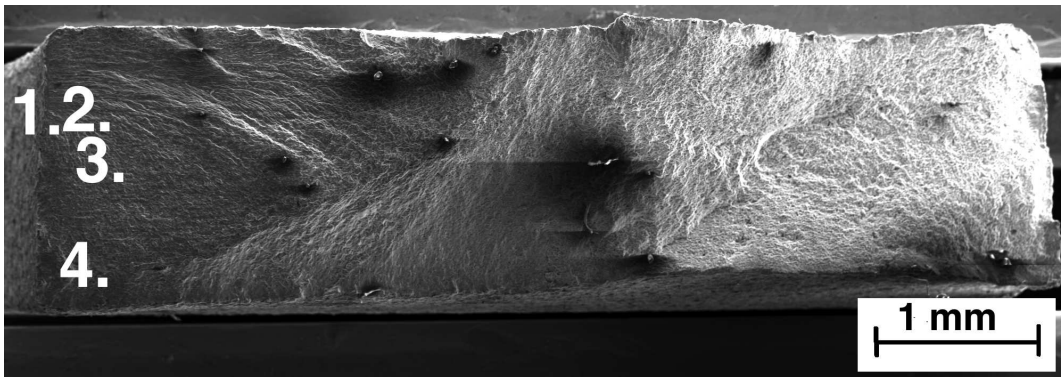

Figure 5.98: Overview of the fracture surface of the shot peened AA6082.50-T6 with fewest cycles to fracture. The numbers represent the different areas investigated further below.

Figure 5.99 show that the fatigue crack initiated at the left edge of the specimen. The micrograph show fan like crack propagation outward from the initiation point. Some inhomogenity can also be seen at the top right surface in the micrograph.

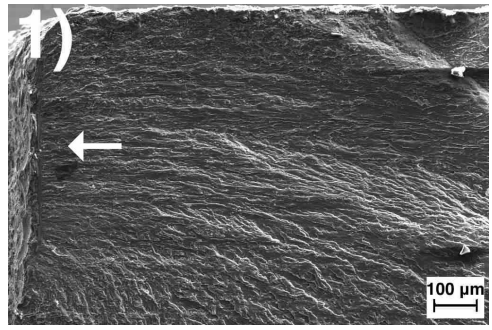

Figure 5.99: Initiation point of the fatigue crack of AA6082.50-T6 SP at the left edge of the specimen.

To the right of the initiation point, river patterns and small microvoids are found, shown in Figure 5.100 (2a). A close up of some of the microvoids (2b) show that their size exceeds 1.5 μm. The outline of some particles are also found, suggesting intergranular crack motion.

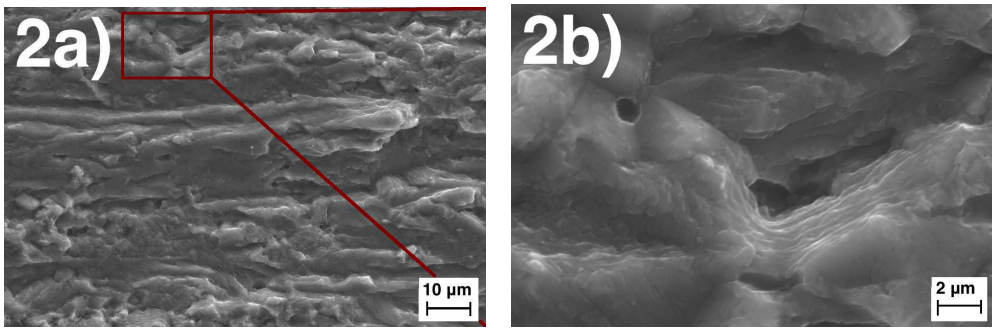

Figure 5.100: River patterns (2a) and microvoids (2b) to the right of the initiation point.

Below the initiation point, Figure 5.101, typical stage II crack propagation is found. Secondary cracks in transgranular propagation (3a) and striations (3b) are also found. The striations in the right micrograph (3b) is about 0.34 μm on average.

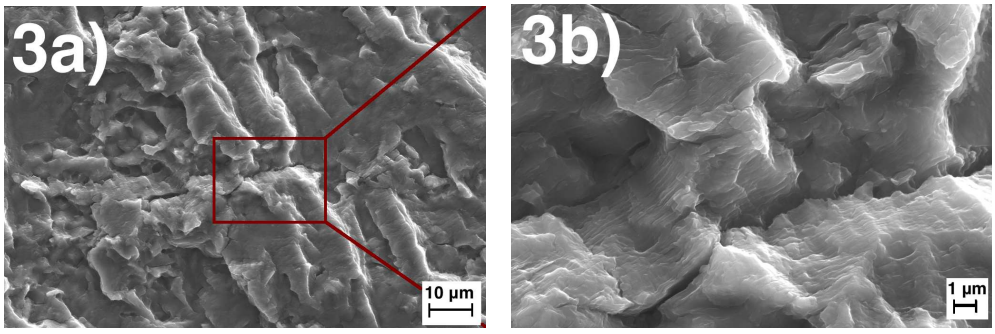

Figure 5.101: Transgranular cracks and striations on the fractured surface of AA6082.50-T6 shot peened.

At the lower left corner more pores are found, shown in Figure 5.102. The average diameter of these pores is found to be 4.5 μm.

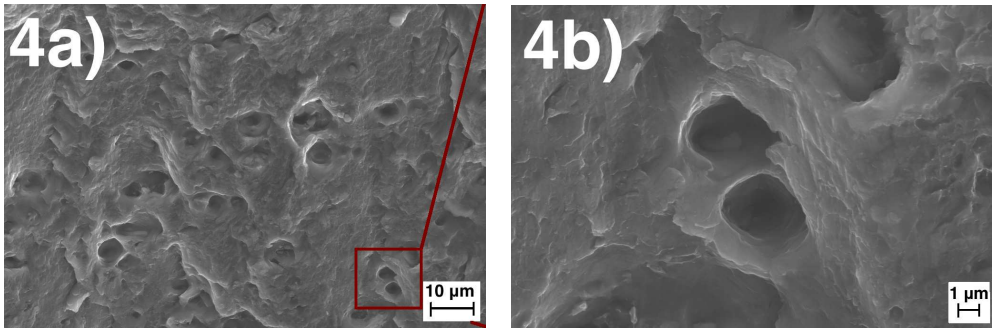

Figure 5.102: Large pores on the fractured surface of AA6082.50-T6 SP.

The shot peened welded specimen that fractured after the most cycles to failure is indicated with an arrow in Figure 5.103. This specimen fractured after $7.5x10^5$ cycles at maximum applied stress of 140 MPa.

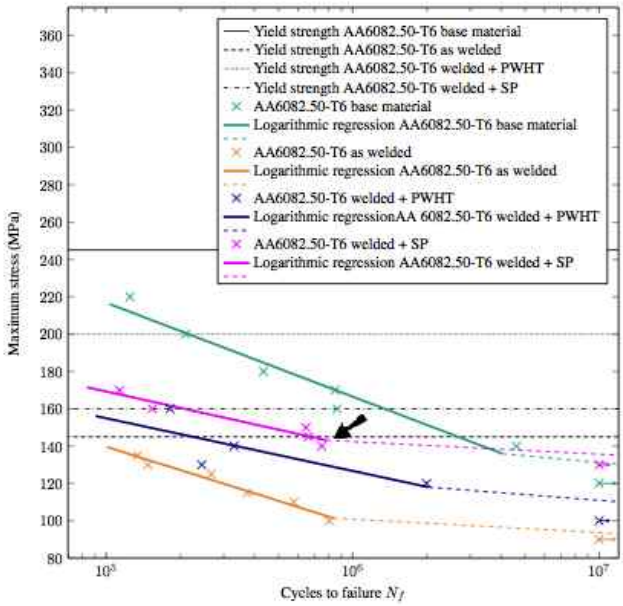

Figure 5.103: The arrow indicates the specimen with the most cycles to failure of the shot peened welded specimens of AA6082.50-T6 investigated further below.

An overview of the shot peened specimen of AA6082.50-T6 with the most cycles to fracture is given in Figure 5.104. The numbers represent the different areas investigated in more detail below.

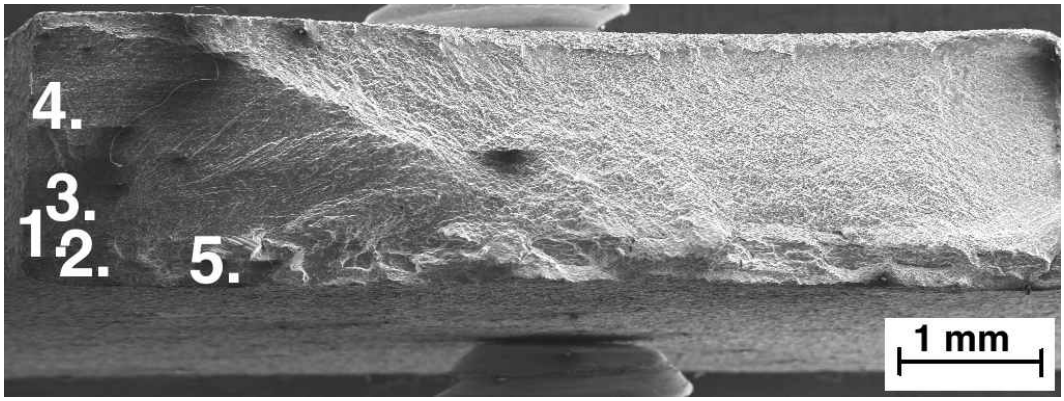

Figure 5.104: Overview of the fracture surface of the welded and shot peened AA6082.50-T6 with most cycles to fracture. The numbers represent the different areas investigated further below.

Figure 5.105 show that the fatigue crack initiated at the lower left corner of the specimen. The right micrograph (1b) show the initiation point in more detail. Some inhomogenity and particles are found at the initiation point. The size of the particles is about 15 μm.

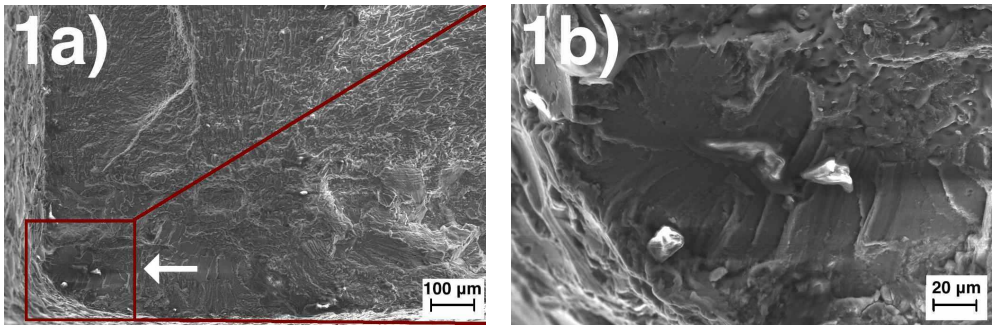

Figure 5.105: Initiation point of the fatigue crack of AA6082.50-T6 SP at the lower left corner. A closer look at the initiation point is shown to the right (1b), together with some particles.

To the left of the initiation point, slip bands from the crack closure movement are found (2a), shown in Figure 5.106. A large particle is found among the slip bands (2b), exceeding 10 μm in size.

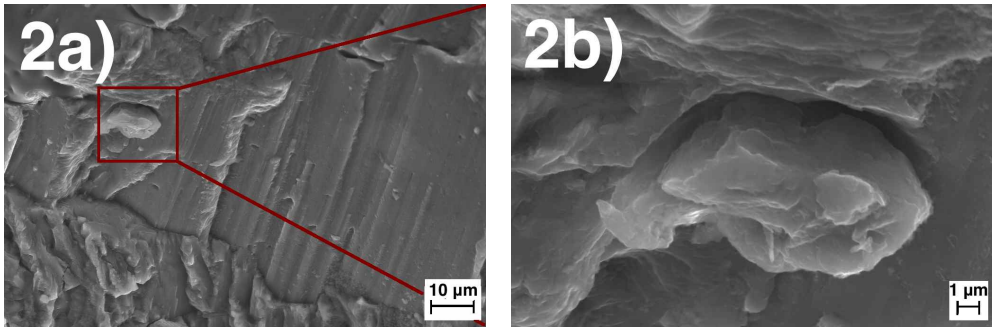

Figure 5.106: Slip bands (2a) and a large particle (2b) to the left of the initiation point.

The area above the initiation point, Figure 5.107, show small pores and some oxidation on the surface. The pore in the right micrograph (3b) is about 3 μm in diameter.

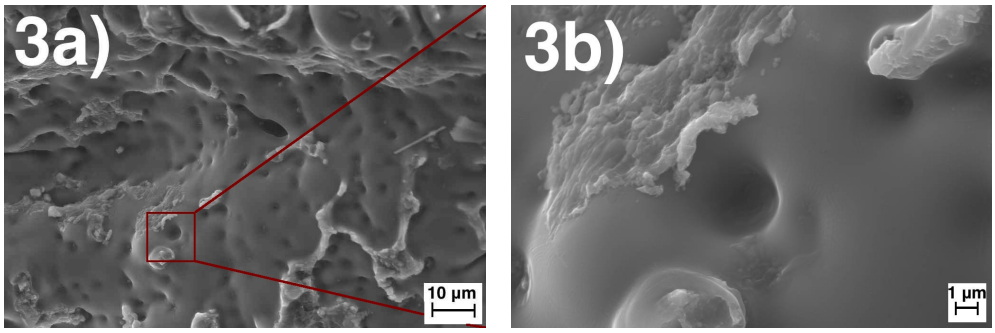

Figure 5.107: Pores and oxidation on the fractured surface of AA6082.50-T6 welded and shot peened.

Striations from the crack propagation (4a) and secondary cracks (4b) are seen in Figure 5.108, in an area above the initiation point. The striations have an average distance of about 0.10 μm.

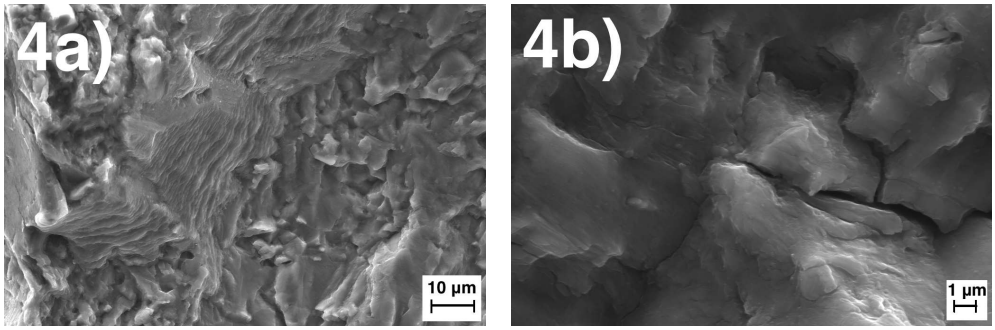

Figure 5.108: Striations and secondary cracks on the fractured surface of the welded and shot peened AA6082.50-T6.

Figure 5.109 show large slip bands and slip planes to the right of the initiation point. A transgranular crack across the slip bands is shown in the micrograph to the left (5a). The striations in the right micrograph (5b) have an average distance of 0.34 μm.

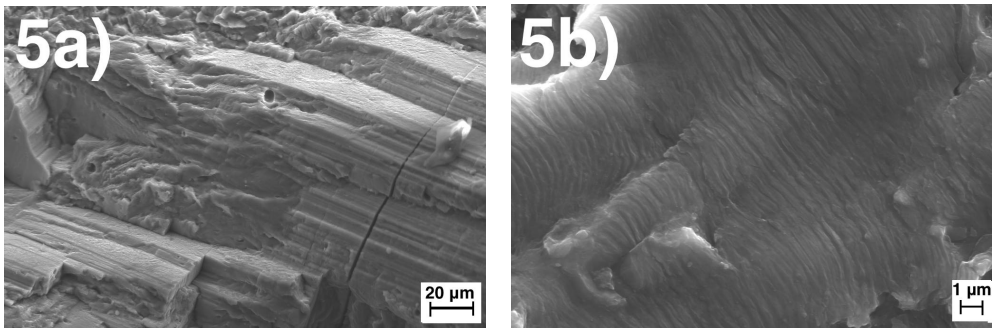

Figure 5.109: Large slip systems to the left (5a). Typical striations to the right (5b) of welded and shot peened AA6082.50-T6.

6 Discussion

This chapter will involve a discussion of all the main topics of this thesis. Microstructure, mechanical properties, fatigue behavior and further work will be discussed by them selves, followed by a conclusion that will relate the topics to each other and to answer the main objective of this thesis: "To correlate the fatigue behavior with the microstructure and mechanical behavior of MIG welded AA6082 alloys, and to investigate the effect of post weld treatments on fatigue life."

6.1 Microstructure and mechanical properties

AA6082.52-T6

The microstructures of the base material and as welded profiles of AA6082.52-T6 are shown in Section 5.1. The AA6082.52 profiles were welded fall 2012 for the specialization project. Figure 5.1 (a) show the typical fibrous microstructure with recrystallized grains along the surfaces of an extruded profile of AA6082.52-T6. The as welded specimen (b) however, has large grains and has lost its fibrous microstructure completely. This is most likely due to the heat input during the welding or lack of complete artificial aging (T6) before being welded. The recrystallized layer however has not been changed during welding. It should be noted that the micrographs were taken in the longitudinal transverse section at the surface of the base material and normal to the extrusion direction for the as welded specimen.

The large HAZ is also seen in Figure 5.2 (c), together with the microstructure of the weld (d). The microstructure of the weld differs in both size, shape and composition, being composed mainly by the filler metal ($AlMg_5$). The heat input during welding and fusion of the filler metal and base material have led to a high degree of nucleation and recrystallization of grains during and after solidification of the weld pool. Some hot cracking was observed at the weld toe due to the stresses occurring during solidification of the weld pool.

The poor welding of the AA6082.52-T6 profile is also reflected in the hardness profile shown in Section 5.2. The as welded AA6082.52-T6 is soft outside the weld bead (gray area) and throughout the profile, presented in Figure 5.7, due to large grains and few strengthening β" particles. The maximal reduction in strength in the HAZ was 60 % compared to the base material. This is expected having the microstructure discussed above. The microstructure of the HAZ also resulted in the tensile fracture occurring outside the weld, in the HAZ, as the grains are significantly larger there. This is in accordance to the Hall-Petch equation 2.1 in Section 2.2.3.

Hardness values from literature are given in Section 3.1. The maximum value for the base material found by Moreira et al. (Moreira et al., 2007) was over 90 HV reached 16 mm from the centre of the weld. The specimen had the softest area in the HAZ, 50 HV. Morgenstern et al. (Morgenstern et al., 2006) found higher values for the base material, 105 HV, and the minimum in the HAZ, 57 HV. These results are similar to the ones found in this thesis, where the base material was measured to be 109 HV and the minimum value found was 43 HV.

The yield strength and ultimate tensile strength of AA6082-T6 alloy found in literature were found to be 276.2 MPa and 322.9 MPa, respectively (Moreira et al., 2007). The yield strength found in this thesis for AA6082.52-T6 was 325 MPa and the ultimate tensile strength was found to be 365 MPa. The exact AA6082-T6 alloy is not given by Moreira et al, thus it gives an indication of what to expect. Yield strength and ultimate tensile strength for as welded AA6082-T6 found in the literature, was 176.8 MPa and 210.0 MPa, respectively (Moreira et al., 2007). In this thesis the yield strength found for the as welded profiles was 95 MPa and the ultimate tensile strength was 188 MPa. A reduction of the yield strength about 71 % and for the ultimate tensile strength by 50 % compared to the base material. Given the poor welding of the as welded AA6082.52-T6, these values differ from the literature as expected. A look at the fatigue fractography in Section 5.7 confirms that the welding of this alloy was not optimal. Large pores, most likely due to air being trapped in the weld bead during welding along with the extent of the HAZ, have reduced the strength of these specimens drastically.

AA6082.50-T6

The micrographs of AA6082.50-T6, Figure 5.3 (a), show a similar microstructure for the base material as the AA6082.52-T6 base material, having the typical fibrous microstructure with a recrystallized layer along the surfaces. The Mn content is the same in both alloys and works as a grain refiner causing the unique fibrous microstructure. The recrystallized surface is generally wider than for the AA6082.52-T6 alloy. This is due to the lack of Cr and less content of Cu and Mg in the AA6082.50-T6 alloy. These differences also reduces the strengths of this alloy, where the yield strength found for AA6082.50-T6 was 245 MPa and the ultimate tensile strength was 306 MPa. These values are also lower than the values found by White et al. (White et al., 2005) for the AA6082.50-T6 alloy, 309.6 MPa and 334.6 MPa for the yield strength and the ultimate tensile strength, respectively.

The base material of AA6082.50-T6 was also tested after being cycled 10^7 and about $3.0x10^6$ cycles without fracture. This was done to document the degree of cyclic softening or hardening of the material. The base material show almost no difference in strength, which indicates little or no alterations of the properties and microstructure of this alloy when being cycled. More data are

however needed to confirm this statement.

The as welded specimen (b) in the micrograph in Figure 5.3 show a completely different situation than for the as welded AA6082.52-T6. The micrograph taken normal to the extrusion direction still has its fibrous microstructure and an almost non-existing HAZ, hence indicating that either the artificial aging before welding was more homogenous throughout the extruded profile or that the heat input during welding was more restricted. The documentation of the artificial aging in Figure B.2 in Appendix B, shows no irregularities. The fact that this microstructure is almost unchanged even after welding, reflects all of the results in this thesis and shows that the welding is considerably better than for the AA6082.52-T6 specimens.

Some hot cracking was also here observed along the weld toe. Hot cracking will reduce the mechanical strength of the specimens and happens as the solidification stresses the microstructure. To reduce the chance of hot cracking, the choice of filler metal is important. For Al-Mg-Si alloys, being very crack sensitive, $AlMg_5$ and $AlSi_5$ have shown to give the best results as a filler metal in MIG welding (Sapa, 2012). Comparing how these two filler metals would differently affect the results, would be interesting to investigate further.

The different situation in the HAZ is also clearly visualized in the hardness profiles in Figure 5.8 and Figure 5.9. The HAZ has almost no extent out in the base material, only showing some grain growth along the fusion line at the surfaces, as is expected this close to the weld. A larger recrystallized surface is also observed along the surface due to the heat input during welding. The filler metal was the same as above, giving the same microstructure. The values measured for the as welded specimen, was 60 HV at the softest area and reached the base material value 18 mm from the centre of the weld resembles the literature values discussed above.

The as welded specimen of AA6082.50-T6 show a reduction in strength compared to the base material, having a yield strength of 145 MPa and an ultimate tensile strength of 236 MPa. Both somewhat the same strengths as given in literature; 176.8 MPa and 210.0 MPa, respectively (Moreira et al., 2007). However, the reductions are not as evident as for the AA6082.52-T6 alloy. The reductions are about 41 % in yield strength and 23 % in ultimate tensile strength compared to the base material. The hardness profiles also indicate a better conservation of strength after being welded. Some reduction would be expected as the 6xxx-series of aluminum is generally affected by heat input. All of the welded specimens fractured in the weld, supporting the Hall-Petch equation 2.1 in Section 2.2.3, as the grains in the weld were more coarse than the fibrous microstructure of the base material and to some extent in the HAZ. The fractographies of the fatigued specimens also confirm a better welding, with no large pores due to entrapment of air during welding as for the AA6082.52-T6. Some inhomogeneties were found, thus almost nothing compared to the as welded AA6082.52-T6.

For the as welded specimens, there were observed some cyclic hardening, especially for the specimen cycled for $3.0x10^6$ cycles. The ductility was reduced, and the strengths were increased with 9 % and 3 % for the yield strength and ultimate tensile strength, respectively. The deemed run-out specimen also experienced some cyclic hardening due to increased dislocation density when cycled in tension. The ductility was also reduced as the strength increased. The applied stress for the specimen cycled for $3.0x10^6$ cycles was 130 MPa and the RO specimen was 90 MPa, hence the higher applied stress the more cyclic hardening.

Post weld treatments

Two different post weld treatments were done on the as welded AA6082.50-T6 alloy. PWHT and shot peening were chosen to see how these affect the reduced strengths due to welding. Figure 5.5 show the microstructure of a PWHT AA6082.50-T6 specimen. The microstructure does not differ from the base material, except for some growth in the recrystallized layer in some areas, due to the heat treatment. The shot peened AA6082.50-T6 specimen in Figure 5.6 also show the same microstructure as the base material. The increased surface roughness due to the shot peening is easily seen along the surface.

The two hardness profiles, Figure 5.8 and Figure 5.9 show again how important the variables of welding can affect the hardness and strength of a welded profile. Figure 5.8 show the before (orange) and after PWHT (blue) situation and that the HAZ is restricted to only 15 mm from the centre of the weld. The PWHT specimen clearly show an increase of strength in both the weld bead (gray area) and in the HAZ. It does not however reach the base material value of 94 HV. This is due to overaging and thereby softening of the base material, as it already had been artificially aged to a T6 tempered condition before being PWHT.

Figure 5.9 show that the shot peening (pink) resulted in an increase of the hardness throughout the whole profile. The specimen has an increased hardness of the base material by 9 HV, up to 103 HV. The softest area is increased by at least 14 HV. By introducing compressive residual stresses, there was an overall increase in hardness of the as welded specimen.

The tensile tests of the PWHT specimens show a very reduced ductility, but an increase in both yield strength and tensile strength. In literature, an increase of 8-10 % was found for both yield and ultimate tensile strength by PWHT (Balasubramanian et al., 2008). In this thesis the increase was found to be 40 % and 6 % for the yield strength and the ultimate tensile strength, respectively. The PWHT causes a reprecipitaion of the strengthening β'' particles, however it also causes an overaging of the already artificially aged base material. The specimen deemed run-out and the un-cycled specimen do not differ much in strength, a part from some reduction in ductility for the RO specimen. The specimen cycled for $3.6x10^6$ cycles has experienced some cyclic softening, resulting in both reduced strength and ductility. The reductions were 18 % and 12 % for the yield strength and the ultimate strength, respectively compared to the un-cycled specimen. A larger reduction than the increased strength due to the cyclic hardening of the as welded specimen. The work hardening of this specimen has had a large impact on strength, however this hardening becomes unstable during post uniform straining, resulting in reduced ductility, probably due to hydrogen diffusion. This has then caused the specimens to be more affected by the geometry change during necking rather than the work hardening when put in tension. The increased temperature during PWHT triggered the diffusion of hydrogen to the grain and particle boundaries and the increased stress during tensile testing made the hydrogen move along with the dislocations in the $< 111 >$ slip systems. The diffusion may only be of micrometer scale, regardless the accumulation of hydrogen could lead to small brittle fractures on the atomic level, seen as serrated yielding throughout the tensile curve. The hydrogen diffusion is driven by the desire to reduce the lattice energy. The post uniform straining was larger for the PWHT than for the as welded and the shot peened specimens.

The induced compressive stresses due to the shot peening increased the yield strength by 10 %

and the ultimate tensile strength by 4 % compared to the as welded specimen. The ductility was more preserved than for the PWHT specimen. It seems however, that shot peening may not have had too much impact on strengthening of the mechanical properties, as the PWHT specimens. Compared to the RO specimen, not much have changed during 10^7 cycles at maximum applied stress at 130 MPa. Some reductions are observed, 6 % and 3 % for the yield strength and ultimate tensile strength, respectively. As the reductions in strength of the RO specimen are so small and no change is observed in the $2.8x10^6$ cycled specimen, this may only be coincidental. The relatively unchanged mechanical behavior of this specimen may be due to the shot peening leading to a saturated state of dislocation density.

These results reflect that both the thermal and the mechanical post weld treatment have had a positive effect on the mechanical properties of the as welded specimen of AA6082.50-T6. No significantly changes were observed in the microstructure due to these treatments.

6.2 Fatigue behavior

AA6082.52

The fatigue curves of AA6082.52-T6 in Figure 5.23 were a continuation of the specialization project from fall 2012. The T1 tempered specimens were only included to give a better overview of the AA6082.52 alloy. Both of the T1 welded specimens possesses a lower fatigue resistance than the as welded specimen in T6 tempered condition, implying less influence by the welding on strength for the latter temper condition despite the poor welding. The base material however show a steeper S-N curve than the base material in the naturally aged condition, indicating a larger difference in fatigue resistance by altering the applied stress. The as welded T6 tempered specimens show a reduction in fatigue life at 10^6 cycles of about 35 %, keeping in mind the large weld defects. There are some uncertainties about the artificial aging as it was not documented and an incomplete or uneven artificially aging may have affected the welding and the mechanical and fatigue properties of these specimens.

The fractures of the base material happened in the desired area (smallest cross section), hence no other factors than fatigue had affected the fractures. The as welded specimens mostly fractured in the HAZ, as expected from the microstructure and the resulting decreased strength.

To predict fatigue life by stress ratios, Equation 2.6, the Goodman diagrams are made based on the data from the S-N curves produced in this thesis. The R-ratios for tension-tension fatigue are given for ease of prediction. The area under the two lines, the Goodman line and the limiting mean stress, represents the safe operating area for fatigue. The area between the two lines indicate the yielding area, at given stress amplitude and mean stress. Above these lines are the non-safe operating area, where fatigue may happen.

The Goodman diagram for AA6082.52-T6 base material show a quite large area for safe operation, as the strength of the material is higher than for the other alloy and specimens. The safe area is mostly restricted by the fatigue limit and not the yield strength. This gives a large yielding area, and this kind of diagram is typical for ductile materials in tension mean stresses (Dowling, 2012).

The as welded specimens of AA6082.52-T6 show that the yield strength was the limiting factor when it comes to fatigue life. The area under this line is very small. This resulting Goodman diagram reflects the poor welding and its effects on both the materials strength and fatigue resistance. These results are not representative for as welded AA6082.52-T6.

Both the base material and the as welded specimens show the usual characteristics of a fatigue crack. The crack initiation stage (stage I) given by a initiation point, slip bands, secondary cracks, intergranular crack propagation and river patterns from cleavage fracture. The crack propagation stage (stage II) including striations, transgranular crack propagation and tire tracks. In addition the final fracture surfaces were of ductile matter. The fatigue crack propagation area is dependent on the length of the fatigue life, and increases with increased life, as expected. The striations of AA6082.52-T6 base material and as welded increases in average distance when fatigue life increases and the stress range decreases, implying some uncertainties about the correlation between striation width, crack propagation life and stress range as the opposite is expected.

In addition to the normal characteristics, the as welded specimens of the AA6082.52-T6, Section 5.7.2, showed a fracture surface that stands out drastically. The fractured surface revealed poor welding, having large pores all through the fractured surface. These results indicate trapped air during welding, decreasing both strength and fatigue resistance for these specimens as noted earlier.

AA6082.50-T6 and post weld treatments

All of the fractures happened in the desired area (smallest cross section), hence no other factors than fatigue have affected the fractures.

The S-N curves of AA6082.50-T6 in Figure 5.24 also show a reduction in fatigue strength after welding, as expected. In addition the fatigue resistances increased due to the post weld treatments. By PWHT the as welded specimens, the fatigue life increased by 26 % and by shot peening the fatigue life increases by 38 % compared to the as welded specimens. This is as expected from literature described in Section 3.3 where an increase of 20-25 % in fatigue strength was found by (Balasubramanian et al., 2008) for PWHT specimens. Unfortunately it was not able to measure the quantity of induced residual compressive stresses in the shot peened specimens. This could have led to a conclusion of how much induced residual compressive stresses there has to be to increase the fatigue life with 38 %, compared to as welded. A research by Bertini et al. (Bertini et al., 1998), showed an increase in fatigue strength by 25 % with maximum -125 MPa induced residual stresses of a MIG welded 6063 aluminum alloy.

It should be noted that each specimen was shot peened individually. The residual compressive stresses may therefore vary between each specimen, however all specimens performed better than the PWHT and as welded specimens, hence indicating that the introduction of residual compressive stresses was successful. Neither is the shot peening variables as Almen intensity and coverage percentage known, which makes the repetitiveness difficult. Due to time limitations a decision was made to conduct this experiment without knowing these variables relying on the characterization of the glass shots together with the measured hardness profile to provide suffice information about the effects of the shot peening on the specimens.

The higher fatigue life for the post weld treated specimens can be explained by the post weld treatments having greater effect on fatigue crack initiation and early propagation (stage I) rather than crack propagation (stage II) (Cheng et al., 2003), which usually is the dominant stage for welded specimens.

A Goodman diagram was made for all of the four specimens of the AA6082.50-T6 alloy. The base material showed somewhat the same diagram as for the base material of AA6082.52-T6. As the strength of this alloy is lower, the resulting area under the two lines is decreased. However the diagram still show a typical diagram for ductile material in tension.

The as welded specimens on AA6082.50-T6 indicates a reduced fatigue resistance in the S-N curves, also demonstrated in the Goodman diagram. The yield strength has a more pronounced effect on the safe operating area than for the base material, and this may be due to the increased ductility of the as welded specimen. In addition, the reduction in yield strength is larger than the reduction in ultimate tensile strength, hence giving these results.

The PWHT, having increased yield strength and ultimate tensile strength, resembles the base materials Goodman diagram. The resulting area under the two lines are smaller than for the base material, as expected due to the generally lower strengths of the material. However, the safe operation area is better than before the PWHT.

Shot peening the as welded AA6082.50-T6 results in a Goodman diagram where the yield strength is the most limiting factor. The yield strength was not increased as much as the PWHT specimen, indicating that shot peening does not have so much effect on the mechanical properties as on the fatigue resistance. The endurance limit however is higher than for the base material, proving the positive effect of shot peening on fatigue resistance, as reflected in the S-N curve.

All of the specimens showed the typical fatigue crack features; the crack initiation stage (stage I), the crack propagation stage (stage II) and the final fracture surface that was of ductile matter. In addition, the fatigue crack propagation area dependent on the length of the fatigue life, increased with increased life.

The average distance between the striations of the base material increased with increasing fatigue life and decreased with increasing stress range, similar to the AA6082.52-T6 specimens. On the contrary, the as welded and post weld treated specimens showed a decrease in average distance between the striations with increasing fatigue life. The striation distances also increased with increased stress range, as is expected from theory. At R = 0.1, the stress ranges does not differ too much and the observed change in striation distance may therefore only be arbitrary depending on where in the specimen they were found and the duration of the crack propagation life (stage II) of the different specimens.

The fractography of the as welded AA6082.50-T6 specimens, Section 5.7.4, show that these specimens also were affected by the welding, having some large inhomogenities and pores on the fractured surface leading to a shorter fatigue life. Oxide layers on the surface resulting from the crack closure movement during crack propagation throughout the specimens were also seen. The fractography of the as welded AA6082.50-T6 however, show that the welding of AA6082.50-T6 was much better than for the AA6082.52-T6, resulting in both better fatigue resistance and higher strengths of the material.

For the PWHT specimens, Section 5.7.5, it seems that the machining of the specimens have caused some notches on the edges, reducing the fatigue lives. A part from these inhomogenities, the fractured surfaces show the usual characteristics of a fatigue fracture.

The shot peened specimens in Section 5.7.6, showed to some extent the same fracture surface as the ones above, except having more pores and microvoids throughout the surface. Figure 5.102 and Figure 5.107 show many pores, and the latter figure also indicates oxide layers. These pores are most likely due to hydrogen diffusion in the specimens during the time between being welded and tested (8 weeks). As the hydrogen has slowly diffused to the nearest grain boundary or particle boundary, small pores have been formed on the surface. The diffusion has happened in room temperature, giving a slow diffusion rate, making this only a local phenomena and it did not have to drastically effect on the fatigue resistance. The smooth area around these pores along with some oxidation can be explained by small crack closure movements during crack propagation. This may have shortened the fatigue lives by making the crack propagation easier. Nevertheless, the shot peened specimens performed better than the other welded specimens.

General remarks

The removal of excess material of the weld may have introduced damaging residual stresses, hence making the specimens less resistant for fatigue than specimens with the weld intact. About 0.5 mm on each side of the specimens were machined down at the fine-mechanic workshop at NTNU, thus removing the recrystallized layers. As this was done for all of the welded specimens, it is assumed that the effect of the removal of excess material was the same for all of the specimens. The removal of excess material would also eliminate the potential moment to be introduced at the weld toes as mentioned in Section 2.7.8.

Welding of the profiles also introduced different variables for each specimen. The heat input is often larger at the start of the welding before stabilizing throughout the plate. These variables are hard to control and therefore about 5 cm on each end of all of the profiles was removed to exclude the largest deviations. However, this does not ensure that the welding was the same throughout the profile, thus creating some differences between each specimen.

Surface roughness of a specimen has a large impact on fatigue life. Having large and sharp notches on the surface can lead to a short fatigue life, and is undesirable. The surface profiles given in Section 5.3 visualizes the roughness of the specimens. The base materials were measured as extruded, while the as welded and post weld treated specimens were measured after the excess material had been removed. All of the surfaces differ from each other in some way, and there are no obvious correlation between these and the fatigue behavior of the specimens. As the surface finish was done individually, many variables would have affected the resulting surface roughness. These surface profiles should only be seen as a visualization, rather than a trend in surface roughness as the uncertainty around the surface finish and the repetitiveness of this is to large.

The increased surface roughness of the shot peened specimen is shown in the micrograph in Figure 5.6. The before and after surface roughness profile of the shot peened specimen are given in Figure 5.15 and Figure 5.16, respectively. These profiles validate the increased surface roughness. The increased surface roughness has, however, not decreased the fatigue strength of the shot

peened specimens as the effect of the induced residual stresses probably surpasses the effect of the increased surface roughness.

The MTS machine used has an applied stress limit at 25 kN. The fact that these fatigue tests were conducted between 0.5 - 3 kN makes the controlling of applied stress less accurate. However, it seems that the controller has stayed within an accepted interval during the testing and the results does not have too much scatter of data, indicating some repetitiveness of the results.

It must be taken into account that time has limited the number of tests being done, and therefore more data are required to validate these results. However, it is a good indication of what can be expected and as the curves show little scatter in data and as the results all point to the same conclusions, some consistency can be drawn form the results.

6.3 Further work

As mentioned earlier, to validate these results and to make a statistical analysis of the fatigue life of welded aluminum profiles, more data are needed. As fatigue is an empirical science, hence lots of data are needed to be able to make a clearer image of the fatigue behavior. In addition, welding introduces many uncertainties when it comes to unusual microstructure and increased porosity, as well as the geometry and the cooling of the molten introduces stress raisers and residual stresses. All of these variables together with the large differences depending on how the profiles are welded, makes the repetitiveness more difficult and requires even more data to be able to predict the fatigue lives. The documentation of all of the variables in all of the tests and methods used are also essential for a better understanding and prediction of fatigue behavior.

A comparison of the two filler metals $AlMg_5$ and $AlSi_5$ to optimize welding of AA6082 or other Al-Mg-Si alloys could be interesting.

The quantification of the induced residual stresses, as well as documenting the intensity and coverage of the shot peening, would increase the repetitiveness and validation of the effect of shot peening, and thereby document how the residual stresses affect fatigue behavior and mechanical properties. To be able to do this, quite complex methods and equipment are needed and this was unfortunately not within the scope of this thesis.

Another interesting aspect to further investigate is the PWHT. As the PWHT of a T6 tempered specimen experienced overaging of the base material, an optimization of time and temperature to increase the strength of the HAZ while preserving the strength of the base material could give even better results than in this thesis. A closer look at the distribution of the reprecipitaion of the strengthening β'' particles would also be interesting, especially in the HAZ.

A more detailed analysis of the fatigue fracture mechanisms is also needed. The extent of both crack initiation stage (stage I) and crack propagation stage (II) of the welded profiles would be interesting to document. Terminating specimens in stage I and stage II followed by an analysis of the fractured surface could give a more insight into the mechanisms of fatigue fracture of the base material compared to the as welded specimens, with or without post weld treatments. Looking at the microstructure of the fractured surface in an optical microscope may also reveal more about the mechanisms and the microstructure.

The effect of hydrogen diffusion in some of the results should also be investigated further. The confirmation of the reduction of strength and fatigue resistance due to hydrogen diffusion is needed. One way to prove this is to look at the fractured surface of the tensile tested specimen and find evidence of small brittle fractures caused by this.

7 Conclusion

In this thesis the fatigue behavior was to be correlated with the microstructure, mechanical behavior and post weld treatments of metal inert gas welded AA6082 alloys.

The microstructure of AA6082.52-T6 was investigated of both the base material and across the weld. The microstructure of the weld revealed poor welding, reducing the yield strength with 71 %, the ultimate tensile strength 50 % and the fatigue resistance with 35 %. This was reflected for all of the results of this alloy. The fracture surface of the fatigued specimens of as welded AA6082.52-T6 showed large pores due to entrapment of air during welding, as well as the hardness profile demonstrated the extent of the HAZ throughout the welded profile.

The investigation of AA6082.50-T6 showed how important the performance of the welding is. The microstructure was completely different from AA6082.52-T6, revealing almost no HAZ. The hardness profiles also showed a more typical variation of strength over the welded profiles. A reduction of the yield strength of the as welded by 40 % was observed and the ultimate tensile strength by 20 % compared to the base material.

By introducing the post weld treatments for the AA6082.50-T6 alloy, the mechanical strength and the fatigue resistance increased. The microstructure seemed generally unchanged when post weld treated. The strengths of the PWHT specimens were larger than for the shot peened, with an increase of 40 % and 6 % for the yield and ultimate tensile strength, respectively. However a large reduction in ductility was observed, most likely due to hydrogen diffusion during PWHT. The shot peened specimen had an increase in yield strength with 10 % and 4 % in ultimate tensile strength. Most specimens did not experience any cyclic hardening, as expected for aluminum. The PWHT specimen was most likely affected by hydrogen diffusion, giving serrated yielding and different results than the other specimens. Some hydrogen diffusion was also found in the fatigue fractography of the shot peened specimens, however the specimens still performed better during fatigue than the other welded specimens.

The as welded AA6082.50-T6 specimen had a reduction in fatigue life by about 40 % compared to the base material. Both post weld treatments had a positive effect on fatigue resistance. PWHT

increased the fatigue life with 26 % and the shot peening with 38 % compared to the as welded.

Further work should include better documentation of all of the parameters of welding, fatigue testing and post weld treatments. A more extensive investigation of the fracture surfaces would give more insight to the extent of hydrogen diffusion during PWHT and the fatigue fracture mechanisms.

Bibliography

Ambriz, R., Chicot, D., Benseddiq, N., Mesmacque, G., De la Torre, S., 2011. Local mechanical properties of the 6061-t6 aluminium weld using micro-traction and instrumented indentation. European Journal of Mechanics-A/Solids 30 (3), 307–315.

Balasubramanian, V., Ravisankar, V., Madhusudhan Reddy, G., 2008. Influences of pulsed current welding and post weld aging treatment on fatigue crack growth behaviour of AA7075 aluminium alloy joints. International Journal of Fatigue 30 (3), 405–416.

Bertini, L., Fontanari, V., Straffelini, G., 1998. Influence of post weld treatments on the fatigue behaviour of Al-alloy welded joints. International journal of fatigue 20 (10), 749–755.

Callister, W., 2007. Materials science and engineering: An introduction. Vol. 7. Wiley New York.

Campbell, F., 2008. Elements of metallurgy and engineering alloys. ASM International (OH).

Cheng, X., Fisher, J. W., Prask, H. J., Gnäupel-Herold, T., Yen, B. T., Roy, S., 2003. Residual stress modification by post-weld treatment and its beneficial effect on fatigue strength of welded structures. International Journal of fatigue 25 (9), 1259–1269.

ClemcoNorgeAs, February 2009. Impact glasskuler.
URL `http://www.clemco.no/clemco/Produktkatalog/Varegruppe_08/Varegruppe_08_Blaasemiddel_og_metalliseringstraad.pdf`

Dieter, G. E., 1984. Mechanical Metallurgy, 2nd Edition. McGraw-Hill International Book Company.

Dowling, N., 2012. Mechanical behavior of materials: Engineering methods for deformation, fracture, and fatigue, 4th Edition. prentice Hall Englewood Cliffs, NJ.

Furu, T., 2012. Material properties. Internal report Hydro Aluminium Sunndal.

Haagensen, P., 2008. Fatigue design of welded structures. Lecture notes TMM4195 Fatigue Design fall 2012.

Hydro, 2012. Aluminium a part of our future.
URL http://www.hydro.com/en/About-aluminium

Klesnil, M., Lukás, P., 1992. Fatigue of metallic materials. Vol. 71. Elsevier Science.

Kopeliovich, D., 2012. Shot peening.
URL http://www.substech.com/dokuwiki/doku.php?id=shot_peening

Kovacs, S., Beck, T., Singheiser, L., 2013. Influence of mean stresses on fatigue life and damage of a turbine blade steel in the VHCF-regime. International Journal of Fatigue 49, 90–99.

Lancaster, J., 2002. The physics of welding. Physics in Technology 15 (2), 73.

Locke, J., Kumar, B., Salah, L., 2005. Effect of shot peening on the fatigue endurance and fatigue crack growth rate of 7050 & 7075 aluminum alloys. In: Proceedings of the 11th International Conference on Fracture ICF-11, Turin, Italy. Elsevier.

Mehmood, A., Hammouda, M., 2007. Effect of shot peening on the fatigue life of 2024 aluminum alloy. Department of Mechanical Engineering, University of Engineering & Technology Taxila-Pakistan.

Moreira, P., De Figueiredo, M., De Castro, P., 2007. Fatigue behaviour of FSW and MIG weldments for two aluminium alloys. Theoretical and applied fracture mechanics 48 (2), 169–177.

Morgenstern, C., Sonsino, C., Hobbacher, A., Sorbo, F., 2006. Fatigue design of aluminium welded joints by the local stress concept with the fictitious notch radius of r = 1mm. International journal of fatigue 28 (8), 881–890.

Myhr, O., Grong, Ø., Fjær, H., Marioara, C., 2004. Modelling of the microstructure and strength evolution in Al–Mg–Si alloys during multistage thermal processing. Acta Materialia 52 (17), 4997–5008.

Myhr, O. R., January 2013. Welding of aluminium. theory, simulations and practical examples. Presentation held at Aluminium Symposium, Doha, Qatar.

Richter-Trummer, V., Tavares, S. M., Moreira, P. M., Figueiredo, M. A. d., Castro, P. M. d., 2008. Residual stress measurement using the contour and the sectioning methods in a MIG weld: Effects on the stress intensity factor. Ciência & Tecnologia dos Materiais 20 (1-2), 114–119.

Sapa, 2012. Welding aluminum.
URL http://www.sapagroup.com/pages/522511/Answer%20Book/11_Welding.pdf

Skorpen, K. G., 2011. Characterization of extruded aluminium. Master's thesis, Norwegian University of Science and Technology.

Solberg, J., 2011. Teknologiske metaller og legeringer. Kompendium, kap 1.

White, C., Andersen, O., Åsholt, P., Bauger, Ø., Furu, T., 11 2005. Fatigue of extruded Al-Mg-Si alloys, internal report Hydro Aluminium Sunndal.

A

Welding parameters

Metal inert gas welding of the profiles were done at SINTEF, Materials and Chemistry, Trondheim, Norway. All of the welding parameters are given in Table A.1.

Table A.1: Metal inert gas welding parameters.

Filler metal $AlMg_5$ 5183				
Alloy	Specimen	Temper condition	Speed [mm/s]	Gap [mm]
6082.52	3-16	T4	10	1
6082.52	3-8/16	T6	10	1
6082.50	7609	T6	10	0

Addition to the welding parameters given above, the shield gas used was Ar 4.6, the welding current varied between 165-170 A, and the voltage used for filler metal 5183 was 22 V, all values are the average input during welding. Figure A.1 illustrates how the profiles were welded together.

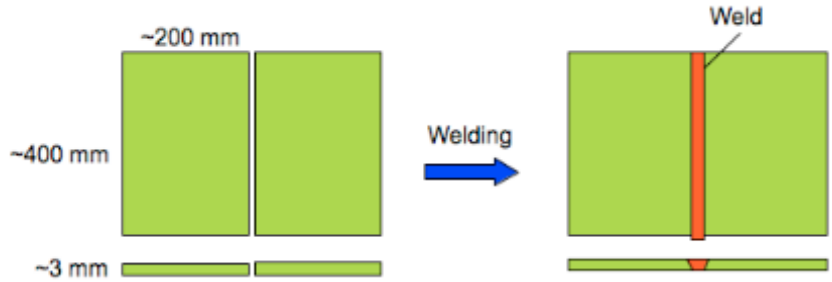

Figure A.1: Description of the welded aluminum profiles.

B

ASTM Standard and specimen design

The specimen used in this thesis followed the guidelines given by the American Society for Testing and Materials (ASTM) standard E466. The ASTM E466 specifically gives the standard for designing a specimen for fatigue testing. The fatigue specimen used in this thesis had a rectangular cross-section and a continuos radius between the ends, as shown in Figure B.1.

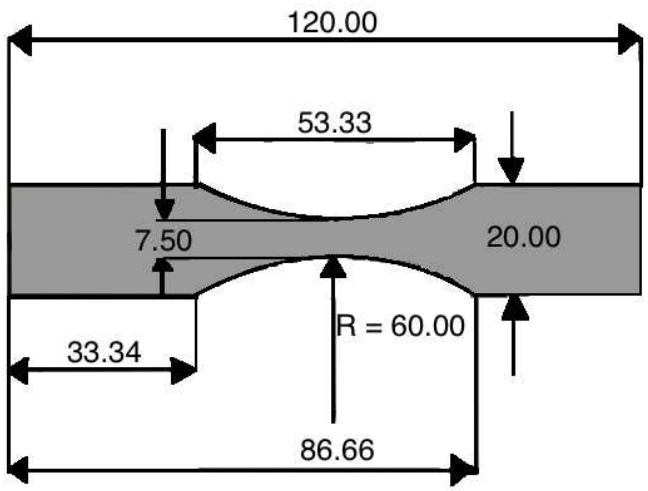

Figure B.1: Tensile and fatigue testing specimen designed by ASTM E466.

Figure B.2 shows the artificial aging of AA6082.50. The PWHT of the as welded specimens followed the same heat treatment.

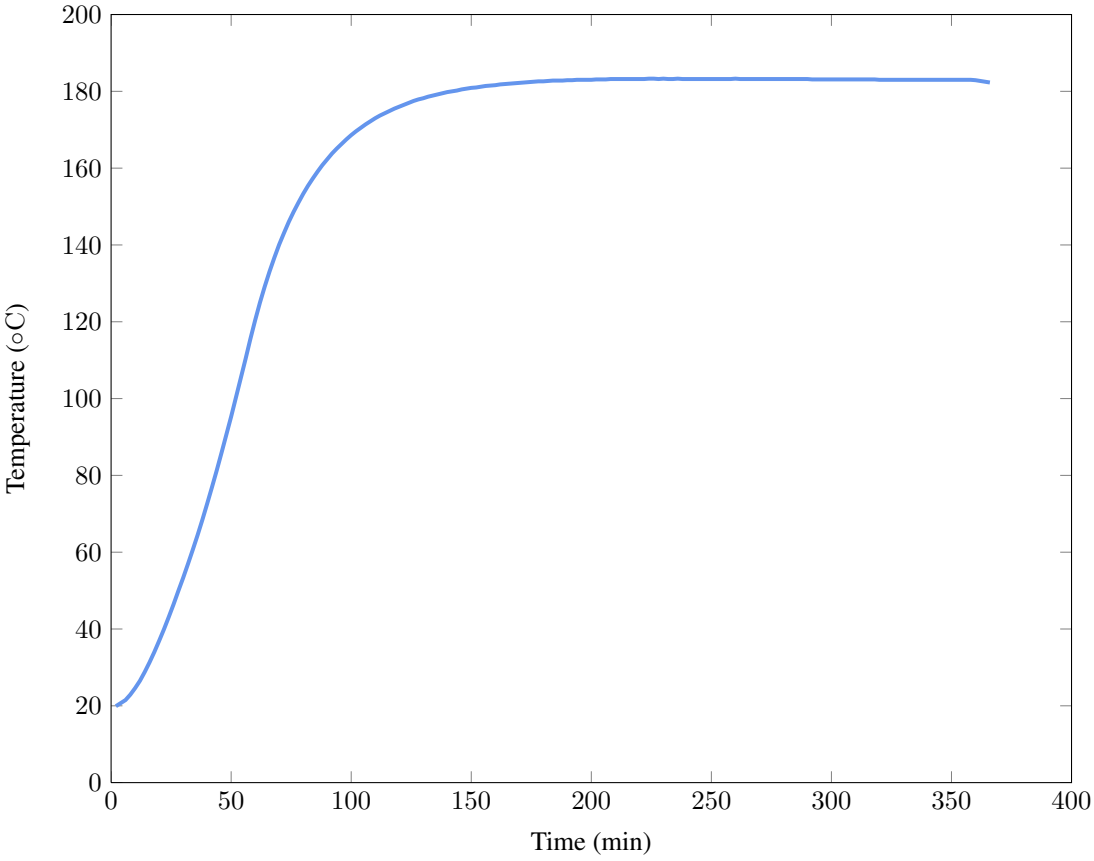

Figure B.2: Artificial aging of AA6082.50.

All of the specimens were machined at the fine-mechanic workshop at NTNU. Figure B.3 show the increased roughness on the shot peened surface of welded AA6082.50-T6.

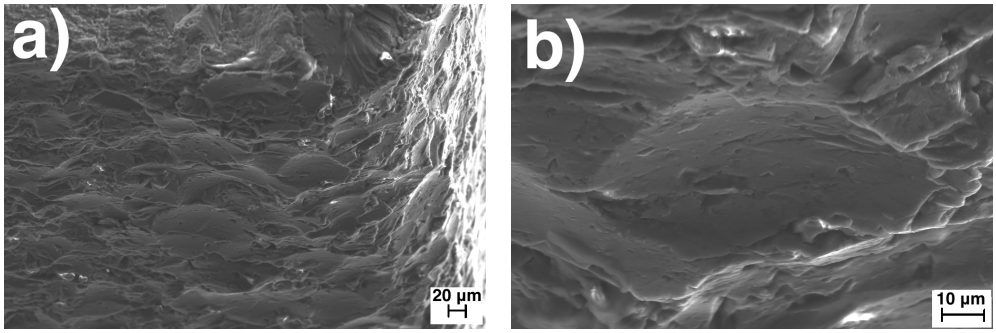

Figure B.3: The effect of the shot peening on the surface of AA6082.50-T6. a) and b) show different magnifications.

Figure B.4 show how the specimens were taken from one of the welded profiles. This was the profile that was post weld heat treated.

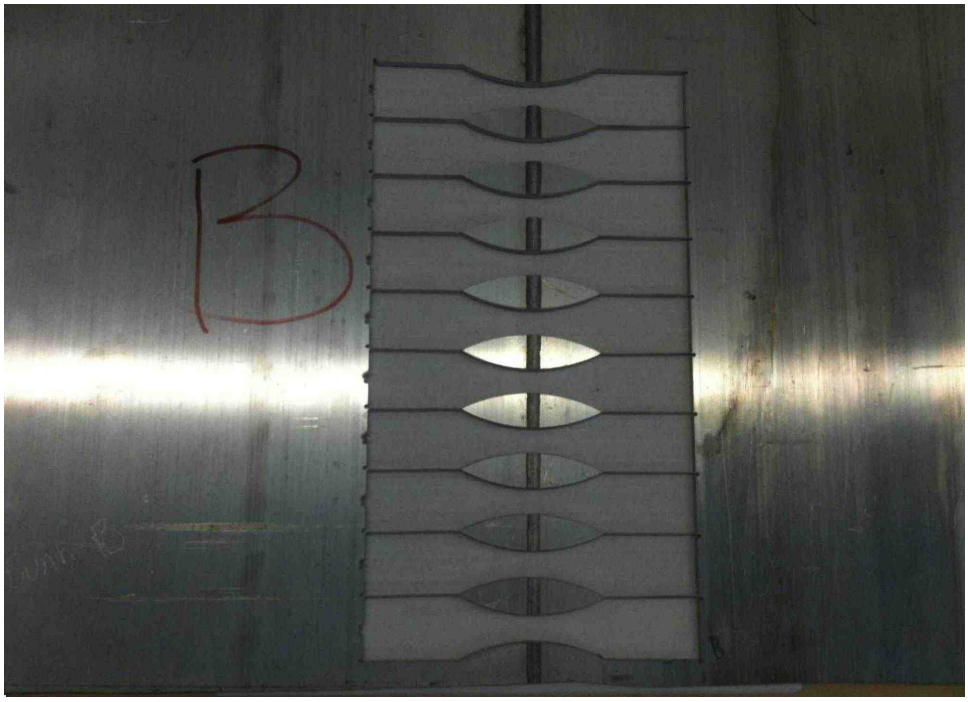

Figure B.4: How the specimens were taken out from one of the welded profiles. These specimens were post weld heat treated.

Designation: E466 – 07

Standard Practice for Conducting Force Controlled Constant Amplitude Axial Fatigue Tests of Metallic Materials[1]

This standard is issued under the fixed designation E466; the number immediately following the designation indicates the year of original adoption or, in the case of revision, the year of last revision. A number in parentheses indicates the year of last reapproval. A superscript epsilon (ε) indicates an editorial change since the last revision or reapproval.

1. Scope

1.1 This practice covers the procedure for the performance of axial force controlled fatigue tests to obtain the fatigue strength of metallic materials in the fatigue regime where the strains are predominately elastic, both upon initial loading and throughout the test. This practice is limited to the fatigue testing of axial unnotched and notched specimens subjected to a constant amplitude, periodic forcing function in air at room temperature. This practice is not intended for application in axial fatigue tests of components or parts.

NOTE 1—The following documents, although not directly referenced in the text, are considered important enough to be listed in this practice:
E739 Practice for Statistical Analysis of Linear or Linearized Stress-Life (S-N) and Strain-Life (ε-N) Fatigue Data
STP 566 Handbook of Fatigue Testing[2]
STP 588 Manual on Statistical Planning and Analysis for Fatigue Experiments[3]
STP 731 Tables for Estimating Median Fatigue Limits[4]

2. Referenced Documents

2.1 *ASTM Standards:*[5]
E3 Guide for Preparation of Metallographic Specimens
E467 Practice for Verification of Constant Amplitude Dynamic Forces in an Axial Fatigue Testing System
E468 Practice for Presentation of Constant Amplitude Fatigue Test Results for Metallic Materials
E606 Practice for Strain-Controlled Fatigue Testing
E739 Practice for Statistical Analysis of Linear or Linearized Stress-Life (*S-N*) and Strain-Life (*ε-N*) Fatigue Data
E1012 Practice for Verification of Testing Frame and Specimen Alignment Under Tensile and Compressive Axial Force Application
E1823 Terminology Relating to Fatigue and Fracture Testing

3. Terminology

3.1 *Definitions:*
3.1.1 The terms used in this practice shall be as defined in Terminology E1823.

4. Significance and Use

4.1 The axial force fatigue test is used to determine the effect of variations in material, geometry, surface condition, stress, and so forth, on the fatigue resistance of metallic materials subjected to direct stress for relatively large numbers of cycles. The results may also be used as a guide for the selection of metallic materials for service under conditions of repeated direct stress.

4.2 In order to verify that such basic fatigue data generated using this practice is comparable, reproducible, and correlated among laboratories, it may be advantageous to conduct a round-robin-type test program from a statistician's point of view. To do so would require the control or balance of what are often deemed nuisance variables; for example, hardness, cleanliness, grain size, composition, directionality, surface residual stress, surface finish, and so forth. Thus, when embarking on a program of this nature it is essential to define and maintain consistency a priori, as many variables as reasonably possible, with as much economy as prudent. All material variables, testing information, and procedures used should be reported so that correlation and reproducibility of results may be attempted in a fashion that is considered reasonably good current test practice.

4.3 The results of the axial force fatigue test are suitable for application to design only when the specimen test conditions realistically simulate service conditions or some methodology of accounting for service conditions is available and clearly defined.

5. Specimen Design

5.1 The type of specimen used will depend on the objective of the test program, the type of equipment, the equipment

[1] This practice is under the jurisdiction of ASTM Committee E08 on Fatigue and Fracture and is the direct responsibility of Subcommittee E08.05 on Cyclic Deformation and Fatigue Crack Formation.

Current edition approved Nov. 1, 2007. Published November 2007. Originally approved in 1972. Last previous edition approved in 2002 as E466 – 96(2002)ε1. DOI: 10.1520/E0466-07.

[2] *Handbook of Fatigue Testing, ASTM STP 566*, ASTM, 1974.

[3] Little, R. E., *Manual on Statistical Planning and Analysis, ASTM STP 588*, ASTM, 1975.

[4] Little, R. E., *Tables for Estimating Median Fatigue Limits, ASTM STP 731*, ASTM, 1981.

[5] For referenced ASTM standards, visit the ASTM website, www.astm.org, or contact ASTM Customer Service at service@astm.org. For *Annual Book of ASTM Standards* volume information, refer to the standard's Document Summary page on the ASTM website.

capacity, and the form in which the material is available. However, the design should meet certain general criteria outlined below:

5.1.1 The design of the specimen should be such that failure occurs in the test section (reduced area as shown in Fig. 1 and Fig. 2). The acceptable ratio of the areas (test section to grip section) to ensure a test section failure is dependent on the specimen gripping method. Threaded end specimens may prove difficult to align and failure often initiates at these stress concentrations when testing in the life regime of interest in this practice. A caveat is given regarding the gage section with sharp edges (that is, square or rectangular cross section) since these are inherent weaknesses because the slip of the grains at sharp edges is not confined by neighboring grains on two sides. Because of this, a circular cross section may be preferred if material form lends itself to this configuration. The size of the gripped end relative to the gage section, and the blend radius from gage section into the grip section, may cause premature failure particularly if fretting occurs in the grip section or if the radius is too small. Readers are referred to Ref **(1)** should this occur.

5.1.2 For the purpose of calculating the force to be applied to obtain the required stress, the dimensions from which the area is calculated should be measured to the nearest 0.001 in. (0.03 mm) for dimensions equal to or greater than 0.200 in. (5.08 mm) and to the nearest 0.0005 in. (0.013 mm) for dimensions less than 0.200 in. (5.08 mm). Surfaces intended to be parallel and straight should be in a manner consistent with 8.2.

NOTE 2—Measurements of dimensions presume smooth surface finishes for the specimens. In the case of surfaces that are not smooth, due to the fact that some surface treatment or condition is being studied, the dimensions should be measured as above and the average, maximum, and minimum values reported.

5.2 *Specimen Dimensions:*

5.2.1 *Circular Cross Sections*—Specimens with circular cross sections may be either of two types:

5.2.1.1 *Specimens with tangentially blended fillets between the test section and the ends (*Fig. 1*)*—The diameter of the test section should preferably be between 0.200 in. (5.08 mm) and 1.000 in. (25.4 mm). To ensure test section failure, the grip cross-sectional area should be at least 1.5 times but, preferably for most materials and specimens, at least four times the test section area. The blending fillet radius should be at least eight times the test section diameter to minimize the theoretical stress concentration factor, K_t of the specimen. The test section length should be approximately two to three times the test section diameter. For tests run in compression, the length of the test section should be approximately two times the test section diameter to minimize buckling.

5.2.1.2 *Specimens with a continuous radius between ends (*Fig. 3*)*—The radius of curvature should be no less than eight times the minimum diameter of the test section to minimize K_t . The reduced section length should be greater than three times the minimum test section diameter. Otherwise, the same dimensional relationships should apply, as in the case of the specimens described in 5.2.1.1.

5.2.2 *Rectangular Cross Sections*—Specimens with rectangular cross sections may be made from sheet or plate material and may have a reduced test cross section along one dimension, generally the width, or they may be made from material requiring dimensional reductions in both width and thickness. In view of this, no maximum ratio of area (grip to test section) should apply. The value of 1.5 given in 5.2.1.1 may be considered as a guideline. Otherwise, the sections may be either of two types:

5.2.2.1 *Specimens with tangentially blended fillets between the uniform test section and the ends (*Fig. 4*)*—The radius of the blending fillets should be at least eight times the specimen test section width to minimize K_t of the specimen. The ratio of specimen test section width to thickness should be between two and six, and the reduced area should preferably be between 0.030 in.^{2} (19.4 mm^2) and 1.000 in.^{2} (645 mm^2), except in extreme cases where the necessity of sampling a product with an unchanged surface makes the above restrictions impractical. The test section length should be approximately two to three times the test section width of the specimen. For specimens that are less than 0.100 in. (2.54 mm) thick, special precautions are necessary particularly in reversed loading, such as $R = -1$. For example, specimen alignment is of utmost importance and the procedure outlined in Practice E606 would be advantageous. Also, Refs **(2-5)**, although they pertain to strain-controlled testing, may prove of interest since they deal with sheet specimens approximately 0.05 in. (1.25 mm) thick.

5.2.2.2 *Specimens with continuous radius between ends (*Fig. 2*)*—The same restrictions should apply in the case of this type of specimen as for the specimen described in 5.2.1.2. The area restrictions should be the same as for the specimen described in 5.2.2.1.

5.2.3 *Notched Specimens*—In view of the specialized nature of the test programs involving notched specimens, no restrictions are placed on the design of the notched specimen, other than that it must be consistent with the objectives of the program. Also, specific notched geometry, notch tip radius, information on the associated K_t for the notch, and the method and source of its determination should be reported.

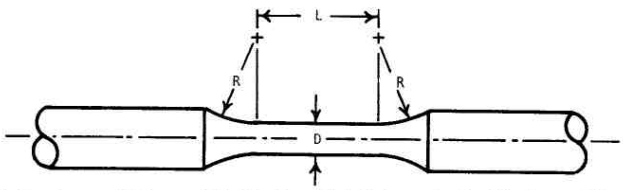

FIG. 1 Specimens with Tangentially Blending Fillets Between the Test Section and the Ends

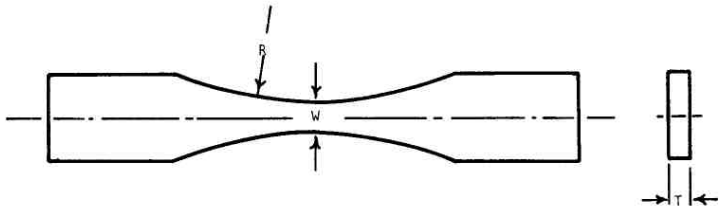

FIG. 2 Specimens with Continuous Radius Between Ends

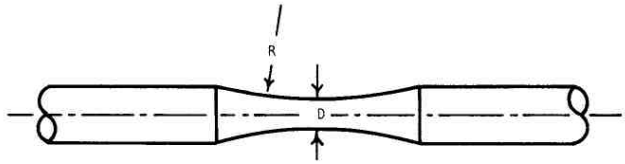

FIG. 3 Specimens with a Continuous Radius Between Ends

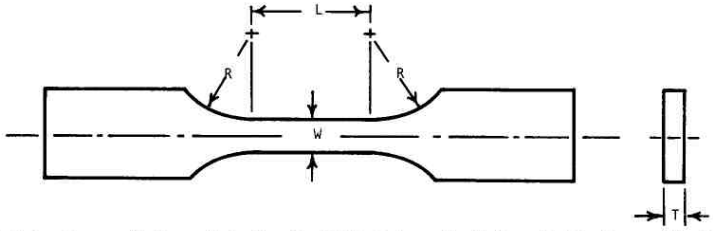

FIG. 4 Specimens with Tangentially Blending Fillets Between the Uniform Test Section and the Ends

6. Specimen Preparation

6.1 The condition of the test specimen and the method of specimen preparation are of the utmost importance. Improper methods of preparation can greatly bias the test results. In view of this fact, the method of preparation should be agreed upon prior to the beginning of the test program by both the originator and the user of the fatigue data to be generated. Since specimen preparation can strongly influence the resulting fatigue data, the application or end use of that data, or both, should be considered when selecting the method of preparation. Appendix X1 presents an example of a machining procedure that has been employed on some metals in an attempt to minimize the variability of machining and heat treatment upon fatigue life.

6.2 Once a technique has been established and approved for a specific material and test specimen configuration, change should not be made because of potential bias that may be introduced by the changed technique. Regardless of the machining, grinding, or polishing method used, the final metal removal should be in a direction approximately parallel to the long axis of the specimen. This entire procedure should be clearly explained in the reporting since it is known to influence fatigue behavior in the long life regime.

6.3 The effects to be most avoided are fillet undercutting and residual stresses introduced by specimen machining practices. One exception may be where these parameters are under study. Fillet undercutting can be readily determined by inspection. Assurance that surface residual stresses are minimized can be achieved by careful control of the machining procedures. It is advisable to determine these surface residual stresses with X-ray diffraction peak shift or similar techniques, and that the value of the surface residual stress be reported along with the direction of determination (that is, longitudinal, transverse, radial, and so forth).

6.4 *Storage*—Specimens that are subject to corrosion in room temperature air should be accordingly protected, preferably in an inert medium. The storage medium should generally be removed before testing using appropriate solvents, if necessary, without adverse effects upon the life of the specimens.

6.5 *Inspection*—Visual inspections with unaided eyes or with low power magnification up to 20× should be conducted on all specimens. Obvious abnormalities, such as cracks, machining marks, gouges, undercuts, and so forth, are not acceptable. Specimens should be cleaned prior to testing with solvent(s) non-injurious and non-detrimental to the mechanical

properties of the material in order to remove any surface oil films, fingerprints, and so forth. Dimensional analysis and inspection should be conducted in a manner that will not visibly mark, scratch, gouge, score, or alter the surface of the specimen.

7. Equipment Characteristics

7.1 Generally, the tests will be performed on one of the following types of fatigue testing machines:

7.1.1 Mechanical (eccentric crank, power screws, rotating masses),

7.1.2 Electromechanical or magnetically driven, or

7.1.3 Hydraulic or electrohydraulic.

7.2 The action of the machine should be analyzed to ensure that the desired form and magnitude of loading is maintained for the duration of the test.

7.3 The test machines should have a force-monitoring system, such as a transducer mounted in series with the specimen, or mounted on the specimen itself, unless the use of such a system is impractical due to space or other limitations. The test forces should be monitored continuously in the early stage of the test and periodically, thereafter, to ensure that the desired force cycle is maintained. The varying stress amplitude, as determined by a suitable dynamic verification (see Practice E467), should be maintained at all times within 2 % of the desired test value.

7.4 *Test Frequency*—The range of frequencies for which fatigue results may be influenced by rate effects varies from material to material. In the typical regime of 10^{-2} to 10^{+2} Hz over which most results are generated, fatigue strength is generally unaffected for most metallic engineering materials. It is beyond the scope of Practice E466 to extrapolate beyond this range or to extend this assumption to other materials systems that may be viscoelastic or viscoplastic at ambient test temperatures and within the frequency regime mentioned. As a cautionary note, should localized yielding occur, significant specimen heating may result and affect fatigue strength.

8. Procedure

8.1 *Mounting the Specimen*—By far the most important consideration for specimen grips is that they can be brought into good alignment consistently from specimen to specimen (see 8.2). For most conventional grips, good alignment must come about from very careful attention to design detail. Every effort should be made to prevent the occurrence of misalignment, either due to twist (rotation of the grips), or to a displacement in their axes of symmetry.

8.2 *Alignment Verification*—To minimize bending stresses (strains), specimen fixtures should be aligned such that the major axis of the specimen closely coincides with the load axis throughout each cycle. It is important that the accuracy of alignment be kept consistent from specimen to specimen. For cylindrical specimens, alignment should be checked by means of a trial test specimen with longitudinal strain gages placed at four equidistant locations around the minimum diameter. The trial test specimen should be turned about its axis, installed, and checked for each of four orientations within the fixtures. For rectangular cross section specimens, alignment should be checked by placing longitudinal strain gages on either side of the trial specimen at the minimum width location. The trial specimen should be rotated about its longitudinal axis, installed and checked in both orientations within the fixtures. The bending stresses (strains) so determined on either the cylindrical or rectangular cross section specimen should be limited to less than 5 % of the greater of the range, maximum or minimum stresses (strains), imposed during any test program. For specimens having a uniform gage length, it is advisable to place a similar set of gages at two or three axial positions within the gage section. One set of strain gages should be placed at the center of the gage length to detect misalignment that causes relative rotation of the specimen ends about axes perpendicular to the specimen axis. The lower the bending stresses (strains), the more repeatable the test results will be from specimen to specimen. This is especially important for materials with low ductility (that is, bending stresses (strains) should not exceed 5 % of the minimum stress (strain) amplitude).

NOTE 3—This section refers to Type A Tests, in Practice E1012.

9. Test Termination

9.1 Continue the tests until the specimen failure criterion is attained or until a predetermined number of cycles has been applied to the specimen. Failure may be defined as complete separation, as a visible crack at a specified magnification, as a crack of certain dimensions, or by some other criterion. In reporting the results, state the criterion selected for defining failure and be consistent within a given data set.

10. Report

10.1 Report the following information:

10.1.1 The fatigue test specimens, procedures, and results should be reported in accordance with Practice E468.

10.1.2 The use of this practice is limited to metallic specimens tested in a suitable environment, generally atmospheric air at room temperature. Since however, the environment can greatly influence the test results, the environmental conditions, that is, temperature, relative humidity, as well as the medium, should always be periodically recorded during the test and reported.

10.1.3 Generally, the fatigue tests may be carried out using a periodic forcing function, usually sinusoidal. However, regardless of the nature of the forcing function, it should be reported (sine, ramp, saw tooth, etc.).

10.1.4 When noticeable yielding occurs in the fatigue tests of unnotched specimens (for example, non-zero mean stress fatigue test) the permanent deformation of the unbroken but tested specimens (for example, percent change in cross-section area of test section) should be reported.

10.1.5 A brief description of the fracture characteristics; results of post-test metallography or scanning election microscopy, or both; identification of fatigue mechanism; and the relative degree of transgranular and intergranular cracking would be highly beneficial.

APPENDIX

(Nonmandatory Information)

X1. EXAMPLE OF MACHINING PROCEDURE

X1.1 While the following procedure was developed for machining high-strength materials with minimal attendant surface damage and alteration, it can be successfully applied to materials of lower strength. As a conservative general measure, this procedure is recommended unless: (*1*) the experimental objective is to evaluate another given surface condition or, (*2*) it is known that the material under evaluation is relatively insensitive to surface condition.

X1.2 *Procedure:*

X1.2.1 In the final stages of machining, remove material in small amounts until 0.125 mm (0.005 in.) of excess material remains.

X1.2.2 Remove the next 0.1 mm (0.004 in.) of gage diameter by cylindrical grinding at a rate of no more than 0.005 mm (0.0002 in.)/pass.

X1.2.3 Remove the final 0.025 mm (0.001 in.) by polishing (Note X1.1) longitudinally to impart a maximum surface roughness of 0.2-µm (8-µin.) R_a, in the longitudinal direction.

NOTE X1.1—Extreme caution should be exercised in polishing to ensure that material is being properly removed rather than merely smeared to produce a smooth surface. This is a particular danger in soft materials wherein material can be smeared over tool marks, thereby creating a potentially undesirable influence on crack initiation during testing.

X1.2.4 After polishing (see Note X1.1) all remaining grinding and polishing marks should be longitudinal. No circumferential machining should be evident when viewed at approximately 20× magnification under a light microscope.

X1.2.5 Degrease the finished specimen.

X1.2.6 If heat treatment is necessary, conduct it before final machining.

X1.2.7 If surface observations are to be made, the test specimen may be electropolished in accordance with Methods E3.

X1.2.8 Imprint specimen numbers on both ends of the test section in regions of low stress, away from grip contact surfaces.

REFERENCES

(1) Worthem, D. W., "Flat Tensile Specimen Design for Advanced Composites," NASA Contractor Report No. 185261, NASA— Lewis Research Center, Cleveland, OH, November 1990.

(2) Miller, G. A., "Interlaboratory Study of Strain—Cycle Fatigue of 1.2 mm—Thick Sheet Specimens," Journal of Testing and Evaluation, JTEVA, Vol 13, No. 5, September 1985, pp 344–351.

(3) Miller, G. A. and Reemsnyder, H. S.," Strain—Cycle Fatigue of Sheet and Plate Steels I: Test Method Development and Data Presentation," *High Strength Steel for Automotive Use, P124*, SAE Paper No. 830175, Society of Automotive Engineers, Warrendale, PA, February 1983, pp 23–31.

(4) Miller, G. A. and Reemsnyder, H. S., "Strain—Cycle Fatigue of Sheet and Plate Steels II: Some Practical Considerations in Applying Strain—Cycle Fatigue Concepts," *High Strength Steel for Automotive Use, P124*, SAE Paper 830173, Society of Automotive Engineers, Warrendale, PA, February 1983, pp 33–41.

(5) Miller, G. A. and Reemsnyder, H. S., "Strain—Cycle Fatigue of Sheet and Plat Steels III: Tests of Notched Specimens," *High Strength Steel for Automotive Use, P124*, SAE Paper 830176, Society of Automotive Engineers, Warrendale, PA, February 1983, pp 43–53.

C

Fatigue testing

All fatigue tests were done at the MTS laboratory at the Norwegian University of Science and Technology. A MTS testing machine was used with the stress ratio, R = 0.1, at a frequenzy of 25 Hz and at room temperature. Table C.1 shows all of the testing parameters and the results from the fatigue testings. Tests that were manually stopped after 10^7 cycles without fracture are deemed run-outs (RO). Some tests were manually stopped before reaching 10^7 cycles due to time limitation or to be used for documenting cyclic hardening or softening after approximately $3.0x10^6$ cycles without fracture. These are marked "aborted" in Table C.1.

Table C.1: Fatigue testing data.

Sample #	Mean stress [MPa]	Stress amplitude [MPa]	Maximum stress [MPa]	Area $[mm^2]$	Cycles to failure N_f
AA6082.52-T1 base material					
1	110.00	90.00	200	21.54	RO
2	148.50	121.50	270	21.55	154198
3	137.50	112.50	250	21.04	385397
4	126.50	103.50	230	20.83	594674
5	118.25	96.75	215	21.02	2028766
6	77.00	63.00	140	21.44	RO
AA6082.52-T1 as welded					
1	74.25	60.75	135	25.17	236412
2	63.25	51.75	115	23.69	2717680
3	68.75	56.25	125	27.20	188380
4	66.00	54.00	120	24.82	675208
5	71.50	58.50	130	25.07	145114
6	60.50	49.50	110	23.46	1611427
AA6082.52-T1 HAZ					
8	63.25	51.75	115	22.40	142575

Continued on next page

Sample #	Mean stress [MPa]	Stress amplitude [MPa]	Maximum stress [MPa]	Area $[mm^2]$	Cycles to failure N_f
9	60.50	49.50	110	22.29	32955
10	52.25	42.75	95	22.14	853731
11	55.00	45.00	100	22.17	3845978
12	57.75	47.25	105	22.39	-
13	59.40	48.60	108	21.91	RO
AA6082.52-T6 base material					
2	192.50	157.50	350	21.99	31237
3	178.75	146.25	325	21.90	48383
4	154.00	126.00	280	22.35	89056
5	126.50	103.50	230	21.99	452585
6	115.50	94.50	210	21.85	861308
AA6082.52-T6 as welded					
2	82.50	67.50	150	16.05	-
3	59.40	48.60	108	18.14	RO
4	70.40	57.60	128	17.37	526366
5	74.25	60.75	135	16.59	1129491
6	79.75	65.25	145	17.40	-
7	57.75	47.25	105	17.89	RO
8	77.00	63.00	140	17.61	437667
AA6082.50-T6 base material					
2	121.00	99.00	220	21.67	124950
3	110.00	90.00	200	21.62	210457
4	99.00	81.00	180	21.62	435226
5	93.50	76.50	170	21.36	848547
6	88.00	72.00	160	21.78	864020
7	77.00	63.00	140	21.58	4624097
8	66.00	54.00	120	21.47	RO
9	104.50	85.50	190	21.32	275404
10	66.00	54.00	120	21.37	Aborted
AA6082.50-T6 as welded					
2	74.25	60.75	135	14.65	134154
3	68.75	56.25	125	15.74	266626
4	60.50	49.50	110	14.94	577650
5	55.00	45.00	100	15.20	802893
6	63.25	51.75	115	14.98	374443
7	49.50	40.50	90	14.75	RO
8	57.75	47.25	105	14.75	344630
9	71.50	58.50	130	13.49	Aborted
10	71.50	58.50	130	14.80	147722
AA6082.50-T6 welded + PWHT					
2	88.00	72.00	160	17.10	181505
3	77.00	63.00	140	16.01	57577

Continued on next page

Sample #	Mean stress [MPa]	Stress amplitude [MPa]	Maximum stress [MPa]	Area $[mm^2]$	Cycles to failure N_f
4	66.00	54.00	120	16.43	1997094
5	77.00	63.00	140	16.19	331035
6	71.50	58.50	130	14.64	244511
7	68.75	56.25	125	16.28	Aborted
8	60.50	49.50	110	16.66	-
9	55.00	45.00	100	16.26	RO
AA6082.50-T6 welded + shot peening					
2	82.50	67.50	150	14.96	647061
3	77.00	67.50	140	15.41	750493
4	71.50	58.50	130	14.21	RO
5	93.50	76.50	170	13.99	113199
6	88.00	72.00	160	15.45	156970
7	85.25	69.75	155	14.31	323096
8	79.75	69.25	145	15.98	662378
9	71.50	58.50	130	14.64	Aborted

Equations (C.1) - (C.3) gives the logarithmic regression curves for the three S-N curves of the base material, the as welded and the HAZ specimens of the AA6082.52-T1, respectively.

$$f(x) = -21.76ln(x) + 527.5 \tag{C.1}$$

$$f(x) = -6.68ln(x) + 210.3 \tag{C.2}$$

$$f(x) = -5.03ln(x) + 172.2 \tag{C.3}$$

Equations (C.4) - (C.5) gives the logarithmic regression curves for the two S-N curves of the base material and as welded specimens of the AA6082.52-T6, respectively.

$$f(x) = -41.00ln(x) + 764.59 \tag{C.4}$$

$$f(x) = -2.21ln(x) + 163.91 \tag{C.5}$$

Equations (C.6) - (C.9) gives the logarithmic regression curves for the S-N curve of the base material, the as welded, the PWHT and the shot peened specimens of the AA6082.50-T6, respectively.

$$f(x) = -21.49ln(x) + 462.96 \tag{C.6}$$

$$f(x) = -18.43ln(x) + 350.56 \tag{C.7}$$

$$f(x) = -7.07ln(x) + 226.69 \tag{C.8}$$

$$f(x) = -12.71ln(x) + 315.64 \tag{C.9}$$